1-1-2008

Three-dimensional numerical simulation of crystal growth using TSM under g-jitter conditions

Elalami Asmae
Ryerson University

THREE-DIMENSIONAL NUMERICAL SIMULATIONOF CRYSTAL GOWTH USING TSM UNDER G-JITTER CONDITIONS

by

ASMAE, ELALAMI

Bachelor of Engineering, Aerospace Engineering

Ryerson University, 2003

A thesis

Presented to Ryerson University

in partial fulfillment of the
requirement for the degree of
Master of Applied Science
in the Program of
Mechanical Engineering

Toronto, Ontario, Canada, 2008

AUTHOR'S DECLARATION

I hereby declare that I am the sole of this thesis.

I authorize Ryerson University to lend this thesis to other institutions or individuals for the purpose of scholarly research.

I further authorize Ryerson University to reproduce this thesis by photocopying or by other means, in total or in part, at request of other institutions or individuals for the purpose of scholarly research.

ABSTRACT

THREE-DIMENSIONAL NUMERICAL SIMULATIONOF CRYSTAL GOWTH USING TSM UNDER G-JITTER CONDITIONS

Master of Applied Science 2008, Asmae, Elalami

Mechanical Engineering

Ryerson University, Toronto

The goal of this thesis is to study the effect of residual gravity on crystal growth of Silicon Germanium $Ge_{0.98}Si_{0.02}$ using the Traveling Heater Method (THM). This method has proven to be one of the most efficient techniques to grow high-quality crystals because it can be grown at relatively low temperatures compared to existing crystal growth techniques. Yet, because of natural convection due to earth's gravity, imperfection in terms of silicon distribution along the growth interface occurs. By growing crystals in a space environment, residual gravity represented by a static microgravity component and a sinusoidal component would decrease the intensity of the convective flow, which in return would lead to a more uniform silicon distribution. However, g-jitter fluctuation has proven to have a noticeable effect on the silicon distribution. Therefore, as an initial step to understand the behavior of crystal growth in space, each component of the g-jitter force will be studied thoroughly. The momentum, mass and energy equations, representing the 3D TSM model, were solved using finite element means. The preliminary results indicate that the complexity and the intensity of the silicon distribution along the growth interface are proportional to the convective flow, that partially controls the migration of silicon. Therefore, the quality of the crystal growth is assessed based on the behavior of the flow along the solvent regime. Based on the imposed static gravity in the range of 10^{-6} g_o to 10^{-3} g_o, the flow was determined to be in a diffusion mode with a velocity ranging from 10^{-6} cm/sec to 10^{-3} cm/sec. As a matter of fact, the flow intensity was noted to be positively proportional to the dominant

component of both the static and the amplitude of the imposed g-jitter and negatively proportional to the frequency of the sinusoidal g-jitter. Consequently, realistic space growth conditions have proven to be an effective way of producing a homogeneous crystal since a flawless crystal silicon distribution is obtained at the growth interface.

ACKNOWLEDGEMENTS

I would like to thank Professor M. Z. Saghir, Ryerson University, for his invaluable guidance, encouragement and great support throughout my graduate study. His patience and guidance are most appreciated of all. Without his collaboration, the completion of this thesis would not have been possible.

I also would like to sincerely thank my colleague, Tawfiq Jaber, for his constant assistance, support and guidance throughout this research.

I would like to dedicate this thesis to my family members, my parents, brothers and sisters, who believed in me and supported me throughout my education. Special thanks to my mother, Fatima Bennani. Without her support, love and patience I would not have gone the distance.

Table of Content

List of Figures

List of Tables

NOMENCLATURE

A	Gravitational Amplitude (cm/s^2)
A^*	Non-dimensionalized gravitational amplitude
C	Non-dimensionalized concentration (atomic %)
c	Solute concentration (atomic %)
c_o	Reference solute concentration (atomic %)
Δc	Change in concentration (atomic %)
c_p	Specific heat capacity at constant pressure (cal/g.K)
D	Reference diameter (cm)
e_z	Axial unit vector
F	Sinusoidal Frequency
E	Electric field (volt/cm)
Gr	Grashof number
g	Gravity (cm/s^2)
g_o	Earth gravity (cm/s^2)
g*	Non-dimensionalized gravity
Ha	Hartmann number
L_f	Latent heat (cal/g)
p	Pressure (g/cm^2.s^2)
Pr	Prandtl number
r	Radial direction(cm)
Re	Reynolds number
R	Non-dimensionalized radial direction
Sc	Schmidt number
T	Temperature (^{o}C)

T_o Reference temperature (°C)

ΔT Change in temperature (°C)

U Non-dimensionalized radial velocity

u Radial velocity (cm/s)

u_o Reference velocity = $\sqrt{g\beta_t \Delta TD}$

U Speed: $\sqrt{u^2+v^2+w^2}$ (cm/s)

V Velocity vector (cm/s)

v Circumferential velocity (cm/s)

w Axial velocity (cm/s)

W Non-dimensionalized axial velocity

z Axial direction (cm)

Z Non-dimensionalized axial direction

Greek Symbols

α_T Thermal diffusivity of the species (cm^2/s)

α_C Solutal (mass) diffusivity of the species (cm^2/s)

β_C Solutal expansion coefficient (1/at %Si))

β_T Thermal expansion coefficient (1/oC)

θ Non-dimensionalized temperature

κ Thermal conductivity (cal/s.cm.K)

μ Dynamic viscosity (g/cm.s)

μ_o Permeability (N/A^2)

ν Kinematic viscosity (cm^2/s)

ρ Density (g/cm3)

φ Circumferential direction

ω Angular velocity (rad/s)

Subscripts

o	Reference
s	Solid phase

Chapter 1

Introduction and Literature Review

1.1 Introduction

Semiconductors are special materials that conduct differently under different conditions, having conductivities intermediate to those of conductors like copper and insulators like wood or plastic. Semiconductors have had a monumental impact on our society. They are found in microprocessor chips, as well as transistors. Anything that is computerized or uses radio waves depends on semiconductors. Silicon and germanium are among the common semiconductors. The reason semiconductors are important is that, with some engineering, they can sometimes both conduct and insulate depending on their connections. Thus, they serve as the basis for switching and amplification, the fundamental actions of computer elements. A typical modern processor has several million transistors, one of the elements manufactured from semi-conducting material, which we will study here. Nearly all the semiconductors used in modern electronics are extrinsic. This means that semiconductors are created by altering the electronic properties of their material composition.

1.2 Crystal Structure

1.2.1 Silicon & Germanium properties

The most commonly used semiconductor material is silicon [1]. This is an element which has 14 electrons with four valence electrons. Its pure solid form melts at 1420 °C. This material is used for thousands of years to make ordinary glass, cements and ceramics among other applications. Silicon turns up in lots of rocks and forms the sand on beaches.

The earliest commercial semiconductor devices mostly used germanium [2]. This element has 32 electrons per atom and melts at 985 °C. It has now largely fallen into disuse because it is rare and more expensive than silicon and has no real advantages for most purposes.

SiGe semiconductor is a leading global supplier of analog and mixed-signal integrated circuits for next-generation cable, high-speed optical and wireless access systems [3]. It can be found in cable phone equipments, optical network interfaces, Bluetooth-enabled portable devices, GPS and telematics systems, and cell-phones.

1.2.2 Semiconductor Background

One of the main reasons that semiconductors are useful in electronics is that their electronic properties can be greatly altered in a controllable way by adding small amounts of impurities. These impurities are called dopants. Heavily doping a semiconductor can increase its conductivity by a factor greater than a billion. In modern integrated circuits, for instance, heavily doped polycrystalline silicon is often used as a replacement for metals [4].

Doping refers to the addition of impurities to a semiconductor. The addition of impurities adds charge, carrying elements to the semiconductor. The two classes of doping are n-type and p-type, which refer to the introduction of positive and negative charge carriers, respectively. For instance, if one introduces a germanium atom into a silicon lattice, the germanium atom would prefer to shed one of the electrons in its outer shell in order to fit in with the silicon lattice. This electron is then available to slide through the material, carrying current. This is an example of n-type doping [5].

Analyzing semiconductors in terms of solid-state physics, semiconductors (and insulators) are defined as solids in which at absolute zero (0 K), the uppermost band of occupied electron energy states, known as the valence band, is completely full. Under absolute zero conditions, the Fermi energy, or Fermi level, can be thought of as the energy up to which available electron states are occupied.

The Fermi level, seen in Figure 1- *1*, lies within the bandgap free of the covalent bond. As they cross the energy band gap into the conduction band, they become free to move around and hence conduct charge. The covalent bonds, from which these excited electrons have come, now have missing electrons. This process is known as the creation of an electron-hole pair. The holes in the valence band behave very much like positively-charged counterparts of electrons, and they are usually treated as if they are real charged particles. As a result, neighboring electrons can move to fill their locations, leading to a matrix of electron relocation. At room temperatures, there is some smearing of the energy distribution of the electrons such that a small, but not a significant, number of electrons have enough energy to break.

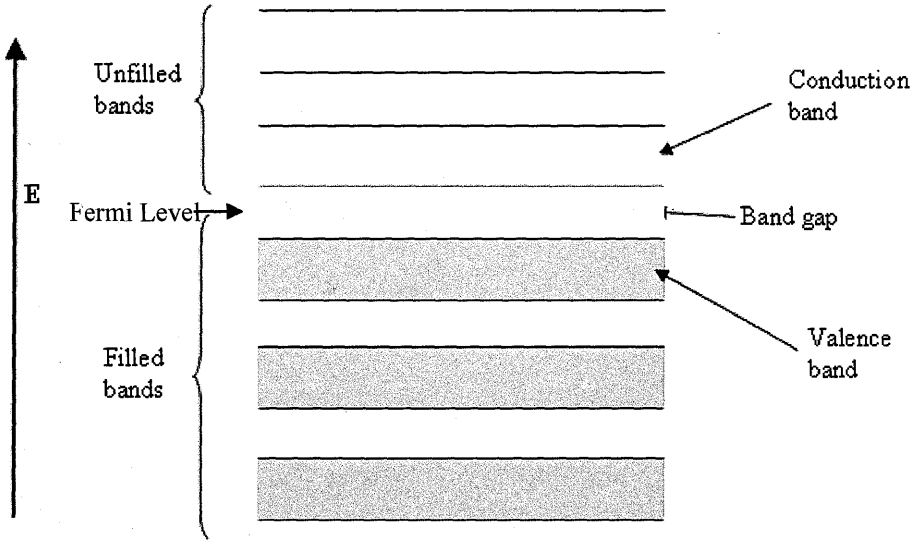

Figure 1- 1: Fermi Level bandgap

The major distinction between conductors and semiconductors is that, in semiconductors, the electron-hole pair facilitates movement of charge in terms of current. Contrast this to a conductor where the Fermi level lies within the conduction band, such that the band is only half filled with electrons. In this case, only a small amount of energy is needed for the electrons to find other unoccupied states to move into, and hence for current to flow. The ease with which electrons in a semiconductor can be excited from the valence band to the conduction band depends on the band gap between the bands, and it is the size of this energy bandgap that serves as an arbitrary dividing line between semiconductors and insulators. Materials with bandgap energy of less than about 3 electronvolts (eV) are generally considered semiconductors, while those with greater bandgap energy are considered insulators.

The concentration of carriers in an intrinsic semiconductor is strongly dependent on the temperature. At low temperatures, the valence band is completely full, making the material an insulator. Increasing the temperature leads to an increase in the number of carriers and a corresponding increase in conductivity. This principle is used in thermostats.

An intrinsic semiconductor, such as the silicon Germanium semiconductor, can be considered pure enough that the impurities in it do not appreciably affect its electrical behavior. In this case, all carriers are created by thermally or optically excited electrons from the full valence band into the empty conduction band. Thus, equal numbers of electrons and holes are present in an intrinsic semiconductor. Note: the concentration of carriers (Silicon) in an intrinsic semiconductor is strongly dependent on the temperature. At low temperatures, the valence band is completely full, making the material an insulator. Increasing the temperature leads to an increase in the number of carriers and a corresponding increase in conductivity. In a well defined structure of semiconductors, electrons and holes flow in opposite directions in an electric field, though they contribute to current in the same direction since they are oppositely charged. Practically, hole

current and electron current are not necessarily equal in an intrinsic semiconductor because the quality of the semiconductors to conduct a current in a controllable direction with high efficiency depends mainly on how well the compositional and structural properties of the crystal are defined.

Semiconductors with predictable, reliable electronic properties are necessary for mass production. The level of chemical purity needed is extremely high because the presence of impurities even in very small proportions can have large effects on the properties of the material. A high degree of crystalline perfection is also required, since faults in crystal structure (such as dislocations, twins, and stacking faults) interfere with the semiconducting properties of the material. Crystalline faults are a major cause of defective semiconductor devices. The larger the crystal, the more difficult it is to achieve the necessary perfection. Current mass production processes use crystal ingots between four and twelve inches (300 mm) in diameter which are grown as cylinders and sliced into wafers.

Because of the required level of chemical purity and the perfection of the crystal structure which are needed to make semiconductor devices, special methods have been developed to produce the initial semiconductor material. Currently, a number of different methods of crystal growth from the melts have been used. In order to obtain optimum growth conditions, all of these techniques require similar conditions throughout the melt. Some of these conditions include having a symmetric heat distribution, a symmetric flow, a smoothed concentration of dopant along the growth interface, and an interface containing the least amount of curvature as possible. All these conditions would confirm the dopant distribution along the crystal structure of the semiconductor is achieved in order to obtain an efficient semiconductor in terms of current flow and response to thermal variation along the semiconductor.

Silicon and germanium in solid-state electronics, either pure silicon or germanium, may be used as intrinsic semiconductors which form the starting point for fabrication. Both silicon and germanium have four valence electrons. Germanium atomic size is larger than silicon. Therefore, at a given temperature, germanium have the tendency to give off more electrons leading to higher conductivity than that of silicon. Silicon is by far the more widely used semiconductor for electronics, partly because it can be used at much higher temperatures than that of germanium.

1.2.3 Crystallization Concept

The general concept of crystalization process is mainly driven by natural convection imposed on the melt zone due to thermal variation and the presence of gravitationl effects. Also, the thermo-solutal effect has to be considered since crystalization growth relies on the mitigation of dopant from the source to the growth interface. The primary objective of crystal growth is to produce a homogeneous material in terms of solutal distribution and therefore eliminating solidification defects. The main obstacle in achieving this goal is the disturbance imposed by unsteady convection such as that encountered in the earth gravity environment.

1.3 Suppression of Unsteady Convection

1.3.1 Usage of Magnetic Field

There are several methods to suppress this undesirable unsteady convection. The most commonly one is the usage of a magnetic field as a mean to weaken the buoyancy-driven fluctuations, which modify the interface shape and its composition during the manufacturing processes of semiconductor crystals, regardless of the crystal growth method used. Moreover, external magnetic fields also play an important role in affecting crystal growth by controlling the fluid flow in metallurgical processes [6], which help improve the homogenous distribution of the dopant along the growth interface. The imposed magnetic field produces a turbulent shear flow,

which improves the distribution of dopant in the melt regime. This phenomenon induces grain refinement effect during the solidification process along the growth interface [7]. In the same manner, a magnetic field can be used to reduce unwanted turbulent flows and fluctuations associated with melt convection during solidification to help eliminate solidification defects.

1.3.2 Usage of Micro-gravity

Another mean of suppressing the undesirable convection is simply to reduce the buoyancy convection by reducing gravity. This method is the least studied and the most costly because it requires a space environment for crystal growth. One may think of the international space station, ISS, or an unmanned satellite as a potential platform for such a crystal growth environment. However, gravity perturbation or g-jitter occurs on board the space platform such as the space shuttle and the ISS due to crew motions, mechanical vibrations, space maneuvers, altitude, and Earth's gravity gradients on the space shuttle. The so-called g-jitter effect has to be studied and its influence on the growth process has to be taken into consideration.

When crystals are grown in an environment where gravity is absent, the crystal quality is improved, because convection is minimized or even eliminated. Without convection, dopant from the source has to be transported by much slower diffusion. A large depletion zone will form, the growth rate will decrease drastically and larger impurities will be less incorporated. Many protein crystallization experiments have been performed on board the ISS and the space shuttle [8, 9, 10]. The results have proven that the reduction of gravity has a beneficial influence on the quality of crystal growth.

In a typical microgravity environment, the residual acceleration experienced by the spacecraft is composed of a steady component and time-dependent component acting in 3D. The magnitude of the time-dependent component is much greater than that of the steady state component. However,

the effect of the two components has to be analyzed extensively in order to be able to understand the flow and concentration behavior under the irregular fluctuation of microgravity encountered in space.

1.4 Literature Review

Currently, there exist several different methods of crystal growth from melts such as the Czochralaki growth technique (CZ), the Bridgman technique, the float zone technique (FZ) and the traveling solvent method (TSM) which is also known as the traveling heater method (THM). In every method, the main objective is to obtain high quality crystal with minimal flaws. Since the basic concept of crystal growth in all these methods is based on the migration of dopant in the melt to the growth interface where it is calcified to grow the crystal, the influence of the growth conditions is considered to be the most important factor that determines the quality of the crystal growth.

The ideal growth conditions can be considered to be a perfectly symmetrical heat distribution and flow, a uniformly distributed dopant concentration, a flat growth interface and zero gravity with non-exiting additional external forces such as vibration. This environment would guarantee that the dopant distribution along the growth interface is purely uniform with no flaws as discussed previously. Such an environment is not practical as there will always be uncontrollable factors such as the unsymmetrical convective flow due to the terrestrial gravitational forces. To obtain more control on the crystal growth procedure, lower gravitational forces have to be imposed in order to achieve the ideal crystal growth environment. Prior to doing so, each method had to be studied extensively in order to identify ways to control its growth environments.

The Czochralski process is the most utilized technique for mass production of semiconductor crystals while achieving high purity crystal. This method was invented by the Polish scientist J.

Czochralski in 1916 [11]. The process is relatively simple. A seed crystal of an element (most usually silicon) is placed just at the surface of the molten silicon solution. To make the crystal as uniform and free from imperfections as possible, the crystal is slowly turned while slowly being drawn up. This allows for high quality crystals to be grown in very large sizes [12]. However, to further increase purity of the crystal structure an additional step, known as zone refining, is required. In zone refining, part of a solid crystal is melted. The impurities tend to concentrate in the melted region, while the desired material recrystalizes leaving the solid material more pure and with fewer crystalline faults.

However, studies conducted by D. Schwabe [13] indicated that under microgravity, thermocapillary flow penetrates fully into the fluid volume of the molten solution whereas it separates into a layer-like flow on top of the liquid at normal gravity. Also it was found that under microgravity oscillation, the mechanism oscillations, such as temperature and flow, are mainly of thermocapillary nature. Therefore, while microgravity lead to unstable tension at the free surface, it was also proven that microgravity with the influence of oscillation does not have a significant effect on the growth behavior. By reducing gravitational effect, convective flow is minimize to a level that allow diffusion flow to dominate on the mechanisms of the crystal growth.

Another mean of controlling the convective flow in the CZ method is the usage of magnetic field. Liu et al. [14] carried out a series of computations which were performed for Czochralski silicon crystal growth in a transverse magnetic field with different crystal growth rates by using a recently developed three-dimensional global model. The effects of the transverse magnetic field and crystal growth rate on the melt–crystal interface were numerically investigated. It was found that the interface shape is three-dimensional when the crystal is not rotating; when the crystal is rotating, even at a low rotation rate, the interface shape becomes nearly two dimensional. The

temperature gradient in the axial direction at the melt–crystal interface increases with increase in crystal growth rate except near the crystal edge, where it changes oppositely.

The Bridgman technique is a directional solidification process. It involves heating polycrystalline material in a container above its melting point and slowly cooling it from one end where a seed crystal is located. Single crystal material is progressively formed along the length of the container. The process can be carried out in a horizontal or vertical geometry. This technique was first patented in the late 1920`s [15], where it was designed for the purpose of growing metallic crystals. In a horizontal Bridgman setup, the furnace is moved along the length of the quartz tube such that the solidification of the melt starting from the seed crystal is achieved as the seed moved from the hotter to the colder section of the furnace. The shape of the crystal is constrained by the walls of the tube. The crystals are typically D-shaped. In general, significantly lower thermal stresses can be obtained in horizontal Bridgeman technique than with the CZ technique. The vertical Bridgman technique is similar to the horizontal Bridgman technique, but here the quartz or PBN crucible contains the seed in a well at the bottom and polycrystaline material above it. For growth to occur, the initial charge and a portion of the seed are melted and the crucible is lowered slowly into the bottom section of the furnace. Instead of moving the crucible the furnace is moved relative to the crucible [16]

Li et al.[17] have studied the effect of the combined g-jitter and magneto hydrodynamic forces effect on the solutal striation in a simplified Bridgman-Stockbarger crystal growth system under microgravity. The results indicated that magnetic field can effectively damp the velocity caused by g-jitter and help to reduce the time variation of solute redistribution. Even though the g-jitter driven flow have the same oscillation period as the driving force, the applied magnetic field help shorten the transient period over which the flow field evolved into a quasi-steady state time harmonic oscillation. It was also seen that a stronger applied magnetic field is more effective in

suppressing the convective flow which in return lead to reduction of the concentration oscillation intensity. The draw back of this paper is it considers 2D analysis using a steady component and time-dependent component for the residual acceleration. Also solidification phenomenon is not considered. All these assumptions are non realistic.

Saghir et al. [18] analyzed the crystallization of GaSb using the horizontal Bridgman method under terrestrial and g-jitter conditions. The research lead to the conclusion that, once g-jitter effect is embedded into the momentum equation as a body force, symmetrical behavior of the flow variables was noticed which indicate good quality crystal growth. However, when simulating a more realistic approach by applying the g-jitter effect directly to the growth interface, larger oscillation in the radial and axial directions were noted. As a result thermal variation was noted everywhere, but minimal at the growth interface. Also, the tellurium concentration at the growth interface was more noticeable and its fluctuation increased as the frequency decreased. It is also interesting to note that micro-gravity of the order 10^{-6} g_o decoupled the energy and the mass transport equations causing the concentration variation (i.e., mass transport equation) to be a pure function of diffusion and not at all a function of thermal distribution (i.e., Energy Equation).

Li et al. have studied the effect of microgravity on crystal growth in a series of papers. In their initial study [19] they examined in details the effect of g-jitter induced flow between a simple apparatus of two parallel plates held at different temperature. The objective was to obtain a general analysis of the flow profile under synthetic single-phase frequency. The results showed that the g-jitter frequency and temperature gradients both contribute to the effect of convective flow. It is found that the amplitude of the velocity decreases at a rate inversely proportional to the g-jitter frequency. The induced flow oscillated at the same frequency as the affecting g-jitter, yet with a phase angle, which could be expressed as a function of the geometry. In two additional

papers [20, 21], they applied the above general analysis to study the combined g-jitter and magneto hydrodynamic forces effects on the solutal striation in a simplified Bridgman-Stockbarger crystal growth system under microgravity. This study also confirmed that convection in microgravity is related to the magnitude and frequency of g-jitter and to the alignment of the gravity field with respect to the growth direction or the direction of the temperature gradient. Residual gravity equivalent to that encountered on a space station is sufficient to cause unacceptable fluid motion in the liquid, which in return affected deleteriously the solute distribution in the melt and hence the quality of crystals grown. Similar to their initial study, it was found that g-jitter driven flow have the same oscillation period as the driving force and the velocity attained a maximum when the gravity vector is perpendicular to the temperature gradient.

Li et al [22] studied the same experiment mentioned above. Except they took into consideration the effect of solidification interface morphology associated with the melt growth of single crystals in microgravity. Similarly they found that frequency, amplitude and spatial orientation of the residual gravity vector all play an important role in determining the convective flow behavior of the system. Under steady microgravity condition, they found that the worst case scenario occurs when the gravity is oriented perpendicular to the growth direction.

Garandet et al [23] took an experimental approach to simulate Sn-Bi crystal growth using the Bridgman method during the USMP-3 space flight mission under the MEPHISTO program. The idea was to use alternative compensating methods that would shorten the duration of the impulse effect on the concentration composition to return to quasi-steady condition. One method was to use a second burn to interrupt the composition decrease caused by the first burn, i.e., pure g-jitter effect, to produce a counterbalance force which would diminish flow fluctuation caused by the

first burn. In return the concentration distribution would be uniform along the growth interface to achieve high quality crystal

The basic idea in float zone (FZ) crystal growth is to move a liquid zone through the material. If properly seeded, a single crystal may result. The FZ method for producing single crystal Si takes place in an inert gaseous atmosphere, keeping a polycrystalline rod and a seed crystal vertically face to face. Both are partially melted by high frequency inductive heating at the (molten zone) liquid phase. In the next step, this molten zone is gradually moved upwards rotating with the seed crystal until the entire polycrystalline rod has been converted to a single crystal. Initially, this method was used for purification (zone melting) as mentioned in the CZ method. The impurities contained in the feed material would then prefer to remain in the melt and thus could be swept to the end of the feed stock. Since the melt never comes into contact with anything but vacuum (or inert gases), there is no incorporation of impurities that the melt picks up by dissolving the crucible material as in the CZ crystal growth method. This is especially true for oxygen, which can not be avoided in CZ crystal growth. Therefore, FZ crystals are always used when very low oxygen concentrations are important. Since the melt zone of this apparatus is supported by surface tension only, it is very hard to grow large wafer sizes. Therefore, this method is abandoned because of the need for mass production of high quality crystals. Other disadvantages in this method include the difficulty to impose forced convection and a restriction on the materials of the crystal growth since in the floating zone, materials with high vapor pressure cannot be grown [24].

Furthermore, the float zone technique commonly applied in microgravity conditions contains a melt zone between a lower seed material and an upper feed rod. This melt zone is maintained by applying localized heating where the melt zone is translated upwards along the rod so that the crystal is growing on the seed and at the same time melting the feed material. The system is kept

crucible free and the melt is held in place by surface tension. With terrestrial conditions the melt zone height is limited as the liquid will run if the molten zone is too large. This limits the possible diameter of crystals grown under gravity. In microgravity the maximum zone height is given by the circumference of the crystal [25].

Saghir et al. [26] studied a numerical simulation of float zone crystal growth of $Bi_{12}GeO_{20}$ under terrestrial and microgravity conditions. A three-dimensional asymmetrically heated molten rod model was developed to estimate the Rayleigh number and the Marangoni convection. Under terrestrial conditions, the surface tension imposed by the capillary pressure, gravity, and viscous forces deformed the free surface. Yet, under microgravity conditions this deformation was not noticed. The non-uniform axial heating created a three-dimensional flow in the radial direction and as it reached the free surface it splits into an upward and downward direction. This non-uniform heating created tangential flow which enhances the convection at the free surface. Under the microgravity condition, the convection was found to be weaker and as a result the float zone melt was more stable.

Unlike the other papers, Lan et al. [27] used axial vibration effect, which is equivalent to uniform frequency application under terrestrial condition, to improve crystal growth of GaAs using the vertical zone melting method. When vibration frequency is high enough the heat flow becomes harmonic. In return, this thermo-vibration induces the convection flow inward causing the concave growth of crystal at the interface to be inverted to a convex one indicating a uniformly distributed concentration composition at the interface. This theoretical analysis is logical as long as the frequency of vibration is high enough and far enough from the resonance frequency where chaotic disturbance would be encountered.

In every technique adopted by researchers, the main objective is to suppress the effect of convective flow. The Traveling Heater Method is a promising crystal growth technique because it offers high-quality bulk single crystals. It is used to grow a single crystal without the need to go through the melt phase as required by some of the other growth techniques. Therefore, using the THM, crystals can be grown at relatively low temperatures compared with the melt growth. Another advantage of this method is that crystals can be grown with less thermal stresses and high purity. Nevertheless, optimization of growth parameters is still required to obtain the required crystal quality.

THM is a solution growth technique in which an applied temperature profile with a precise temperature gradient is the driving force for growth. Growth is achieved by the movement of the crucible relative to the applied temperature profile. The main mechanism for the mass transport in the liquid solution is the diffusion combined with strong thermo-solutal convection due to large temperature and concentration differences. The ampoule in this technique contains the seed material at the bottom, the melt in the middle and the feed material in the top. The solution zone is heated by radiation usually given off by halogen lamps encompassed in a mirror furnace. When the temperature profile moves upwards, the solution-source interface (dissolution interface) hits the hotter section of the temperature profile and dissolves the polycrystalline source material. This dissolution provides constantly the needed material to the liquid solution. With the movement of the temperature profile, at the same time, the seed-solution interface (growth interface) hits the cooler section of the temperature profile, and the supersaturated solution in the vicinity of the growth interface solidifies on the seed crystals. With this process, a constant, controlled, but slow growth, i.e. in the range of 1mm/day, is achieved. The quality of grown crystals in THM is very sensitive to the relative movement of the temperature profile that determines the growth rate. THM has a number of advantages over melt techniques, namely less thermal stresses, growth of ternary alloys, and uniform crystal composition.

Ye et al. [28] studied the effect of the thermosolutal convection on CdTe growth by the traveling solvent method. This study was carried out both experimentally and numerically. Initially, a thermosolutal convection model was developed to simulate the couple heat, solute, and fluid fields in the growth ampoule. The results, both experimentally and numerically, showed that the solute distribution in the melt zone is greatly influenced by the convective mass transfer and therefore, the growth rate increases proportionally. It was also found that a smaller and uniform heater thermal gradient moderate the effect of free convection in the substrate interface region leading to better Cd distribution at the growth interface.

Boschert et al [29] have tackled the growth of S-doped InP crystals using the THM under space environment both experimentally on the EURECA-1 flight and analytically using a 3-D finite element model while considering the thermal as well as the solutal buoyancy effects. The obtained results indicate that even under fixed altitude, residual gravity is obtained due to the rotation of the satellite location with respect to the sun. This rotation results in a significant change of the residual convection level, where its maximum is obtained when the gravity is parallel to the growth interface. This effect was also noted to have a substantial influence on the concentration variations along the growth interface.

Jaber et al [30] have also conducted a 3D simulation of the effect of axial and rotational magnetic field on the SiGe crystal growth using the THM. The results indicated that axial magnet suppress convective flow leading to more stable and uniform crystal growth, while rotational magnetic field was found to change the behavior of silicon distribution at the growth interface from a convex shape to nearly flat at a limiting magnetic field intensity of 15 mT and 7 rpm.

1.5 Research Objective

A realistic set of data that represent the above jitter status would be complex to start with. Therefore, in order to understand the behavior of flow convection under these conditions, it is best to start with micro-gravitational, harmonic gravitational fluctuations then the real g-jitter effect. In this thesis, the $Ge_{0.98}Si_{0.02}$ single crystal will be grown under micro-gravitational conditions, as well as g-jitter conditions, i.e., sinusoidal fluctuations. Because g-jitter from different platforms follows a certain sinusoidal oscillation, different amplitude and frequencies will be implemented in the model to investigate their effect on the growth process.

Since previous studies have concentrated mostly on the usage of a magnetic field as a mean of suppressing convective flow in the melt regime, this thesis will be dedicated to the analysis of crystallization behavior of $Ge_{0.98}Si_{0.02}$ under micro-gravity environments. To further understand the effect of space gravity on crystal growth, simplified SiGe crystal growth experiments under static micro-gravity, sinusoidal microgravity and g-jitter will be studied thoroughly. The outcome of this thesis will enhance our fundamental understanding of fluid mechanics and thermal phenomena in space crystal growth systems as well as develop rational guidelines for both space experiment design and interpretation of experimental measurements.

1.6 Thesis Organization

This thesis consists of seven chapters organized as follows:

- Chapter one presents an introduction to semiconductors and a literature review.
- Chapter two displays governing equations which are used to solve the problem, as well as the full model and the boundary conditions applied to it. The finite element analysis method used to solve the equation is also discussed in detail. In this chapter, the mesh sensitivity is also analyzed.

- Chapter three contains the results of the static gravity condition, including terrestrial and microgravity conditions.
- In chapter four, the results and discussion of sinusoidal microgravity conditions will be considered. This includes the effect of amplitude and frequency of the oscillating microgravity. The actual g-jitter analysis results will also be discussed in this chapter.
- Finally, chapter five presents the conclusions.

Chapter 2

Mathematical Model and Numerical Solution

2.1 Model Description

2.1.1 Finite Element Model

The finite element model of the crystal growth of $Ge_{0.98}Si_{0.02}$ using the traveling heater technique (THM) is shown in Figure 2-1. The model is represented by a fixed cylinder with the coordinate system (r, φ, z) and the origin at the center base of the model. The model is 6.1 cm long and has a diameter 0.8 cm. It consists of a $Ge_{0.85}Si_{0.15}$ source rod (feed rod) having a length of 3.6 cm. This rod is located on top of a $Ge_{0.98}Si_{0.02}$ solvent having the same diameter and a length of 1.0 cm. At the bottom is the germanium seed (substrate) having a length of 1.5 cm and it also has the same diameter. Table 2- 1 highlight the main properties of the finite element model of this analysis in terms of the material compositions, dimensions and meshing scheme for both steady state and transient analysis. The total sample is enclosed in an ampoule (quartz tube) having a wall thickness of 0.1 cm. The non-uniform temperature profile is applied at the external surface of the quartz tube. Since the thermal effect will be highly focused on the solvent region, the meshing scheme is refined within this region to obtain better quality. Sensitivity analysis will be carried forward to assess the effect of the meshing scheme on the quality of the data.

Component	**Material Composition**	**Dimension**	**Mesh size** Length x Radial (nodes)
Substrate	100% Ge	Length: 1.5 cm Radius: 0.8 cm	60 x 60(Steady State Analysis) 5 x 40 (Transient Analysis)
Solvent	2% Si 98% Ge	Length: 1.0 cm Radius: 0.8 cm	240 x 60 (Steady State Analysis) 20 x 40 (Transient Analysis)
Source	15% Si 85% Ge	Length: 3.6 cm Radius: 0.8 cm	80 x 60 (Steady State Analysis) 5 x 40 (Transient Analysis)

Table 2- 1: Dimensions, composition and meshing scheme of the finite element model

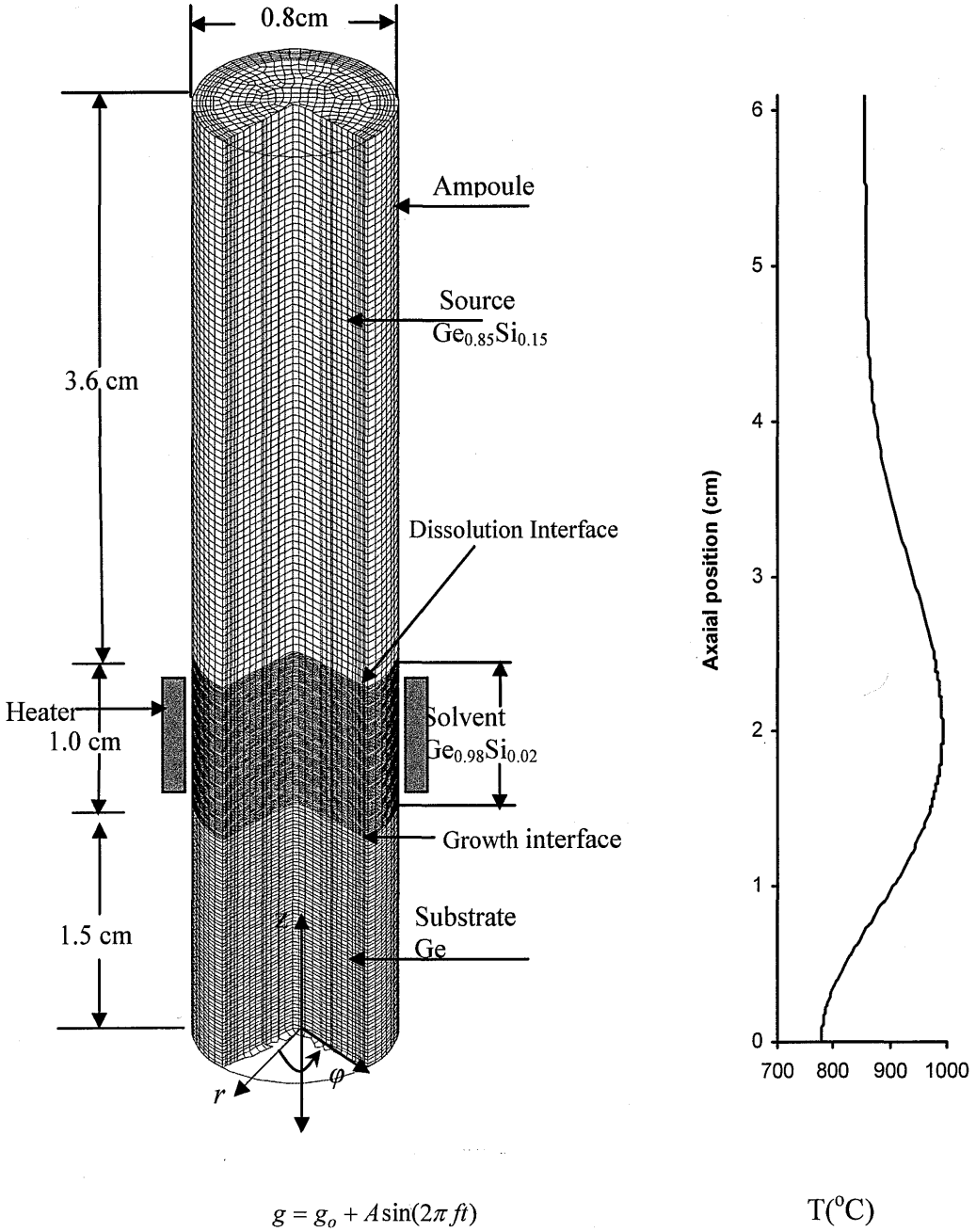

Figure 2-1: a) Finite element model and b) applied non-uniform thermal profile

2.1.2 TSM System Description

TSM system consists of a furnace with a cylindrical enclosure and the ampoule (quartz tube) containing the liquid-solid semiconductor materials, as shown in Figure 2- *2*. The heater thermal profile used for this simulation is measured experimentally at Dalhousie University and applied to the model in a non-dimensional form by using a best-fit 6-polynomial curve along the r direction at $\varphi=0°$ and at $\varphi=90°$. Dalhousie experiments provide data for symmetric and unsymmetrical heating profiles. The unsymmetrical heating profile is a result of a lagging furnace where heat is lost due to convective flow through the air. This loss normally is minimal. However, to study a more realistic crystal growth in a space, non-uniform heating profile will be applied throughout this analysis.

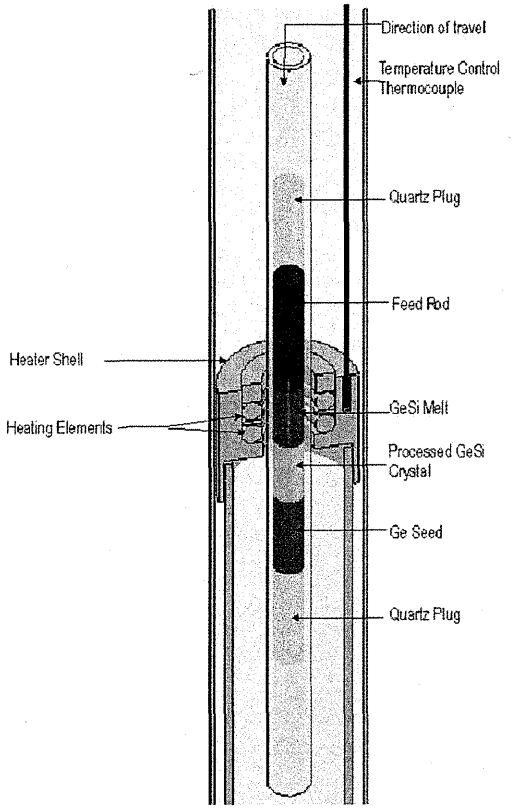

Figure 2- 2: The traveling solvent method process

2.2 Crystal Growth Technique

The basic concept of the Traveling Solvent method relies on the transient thermal profile along the feed rod. The TSM process has three main phases. Figure 2- *3* shows these phases. Initially, the $Ge_{0.85}Si_{0.15}$ polycrystalline feed rod is heated to the melting temperature of Germanium. Because Silicon (Si) has a higher melting temperature than Germanium (Ge), the solvent state becomes molten without melting the feed material and allowing the Silicon to be softened so it can slowly diffuse into the melt. Note: at the bottom of the initial melted phase, the composition is $Ge_{0.98}Si_{0.02}$, while at the top of melted region, a different composition of $Ge_{0.85}Si_{0.15}$ exists. Since the melting temperature of the solvent ($Ge_{0.98}Si_{0.02}$) at the bottom is less than the source rod ($Ge_{0.85}Si_{0.15}$) at the bottom, and silicon concentration at the top is higher than that at the bottom, Silicon will be segregating from the source rod toward the bottom rod at a rate driven by the buoyancy effect and silicon concentration variation. Once a steady state has been accomplished, the second phase begins where the heater begins to slowly translate up the polycrystalline feed rod, allowing the new single crystal to form along the growth interface. During this procedure, the silicon diffuses through the solvent from the dissolution interface to build up at a certain rate at the growth interface. This stage is complete once the heater has traveled the full length of the feeder rod. The speed at which the heater travels upward determines the composition and the growth rate of the crystal. Experimentally, the appropriate growth rate was found to be about 4 mm/day [30]. In the last phase, the heater is shut off and the molten region at the top of the formed single crystal is allowed to cool and solidify ending the crystal process.

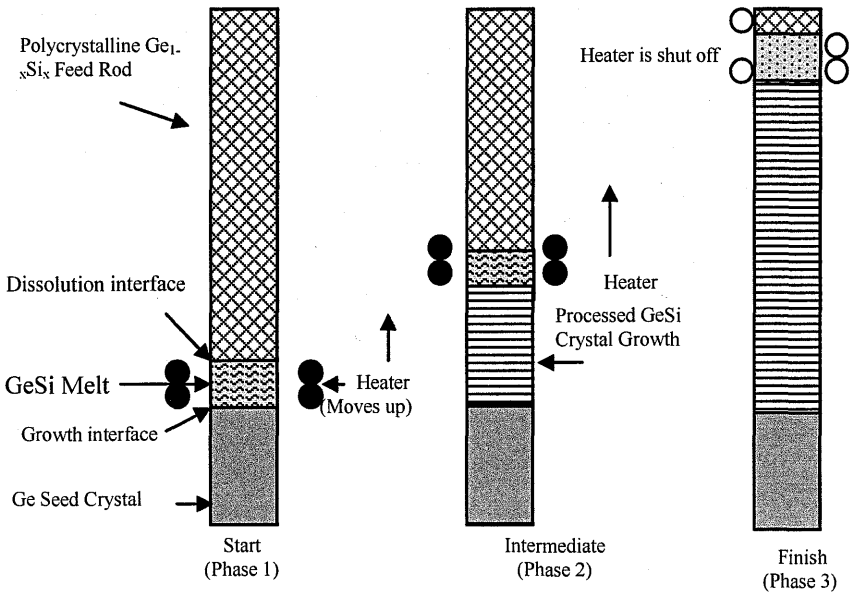

Figure 2- 3: Schematic Diagram of the TSM Phases

2.3 Governing Equations

The mathematical model for the growth process includes the three-dimensional steady- state Navier-Stokes equations (momentum equations) combined with the energy equation, the mass transport equation and the continuity equation. Cylindrical coordinates (r, φ, z) are used in this simulation.

Based on the above model, the flow in the melt regime will be unsteady, laminar and incompressible. The Navier-Stokes equations listed below with the addition of the Boussinesq approximation to account for the density variation are used in this model. The aim is to solve for the rate of flow, pressure and positions of any free surface. Since the two species (Si, Ge) interact in the melt, two transport equations are supposed to be solved in parallel. However, since our concern is about the Silicon distribution behavior, only one transport equation accounting for the Silicon distribution will be utilized in this analysis. Furthermore, in the final stage of this analysis,

axial magnetic force will be utilized to suppress any convective flow. Therefore, an additional body force representing the axial magnetic field will be embedded in the 3D momentum equations.

2.3.1 Navier-Stokes Equations

r – Component

$$\rho\left[u\frac{\partial u}{\partial t}+u\frac{\partial u}{\partial r}+\frac{v}{r}\frac{\partial u}{\partial \varphi}+w\frac{\partial u}{\partial z}-\frac{v^2}{r}\right]=-\frac{\partial p}{\partial r}+\mu\left[\nabla^2 u-\frac{u}{r^2}-\frac{2}{r^2}\frac{\partial v}{\partial \varphi}\right]+F_r^{\,g} \qquad (2\text{-}1)$$

φ - Component

$$\rho\left[\frac{\partial v}{\partial t}+u\frac{\partial v}{\partial r}+\frac{v}{r}\frac{\partial v}{\partial \varphi}+w\frac{\partial v}{\partial z}+\frac{vu}{r}\right]=-\frac{1}{r}\frac{\partial p}{\partial \varphi}+\mu\left[\nabla^2 v-\frac{v}{r^2}+\frac{2}{r^2}\frac{\partial v}{\partial \varphi}\right]+F_\varphi^{\,g} \qquad (2\text{-}2)$$

z - Component

$$\rho\left[u\frac{\partial w}{\partial t}+u\frac{\partial w}{\partial r}+\frac{v}{r}\frac{\partial w}{\partial \varphi}+w\frac{\partial w}{\partial z}\right]=-\frac{\partial p}{\partial z}+\mu\left[\nabla^2 w\right]+F_z^{\,g} \qquad (2\text{-}3)$$

Where u, v, and w corresponds to radial, angular and axial velocities respectively. The density is identified as ρ, the viscosity as μ and the pressure as p. T is the temperature, T_m is the melt temperature, c and c_o are the Si concentration and its reference concentration. The three forces F_r^g , F_φ^g and F_z^g denote the gravitational body force imposed along the r, φ, and z-direction in a space environment. Under the controlled gravitational environment, the gravitational forces are assumed to act along the z-direction only because it has been proven that the most severe effect of g-jitter is noted once gravitational forces are applied perpendicular to the growth interface [31], i.e., along the z-direction. In such case F_r^g and F_φ^g components will be dropped. Furthermore, the transient components of the above equations will also be dropped once analyzing the effect of static gravity only.

2.3.2 Energy Equation

The heat transfer is described by the Energy equation:

$$\rho c_p\left[\frac{\partial T}{\partial t}+u_r\frac{\partial T}{\partial r}+\frac{u_\varphi}{r}\frac{\partial T}{\partial \varphi}+u_z\frac{\partial T}{\partial z}\right]=k\left[\frac{1}{r}\frac{\partial}{\partial r}\left(r\frac{\partial T}{\partial r}\right)+\frac{1}{r^2}\frac{\partial^2 T}{\partial \varphi^2}+\frac{\partial^2 T}{\partial z^2}\right] \qquad (2\text{-}4)$$

Here C_p is the specific heat and k is the thermal conductivity.

2.3.3 Mass Transport Equation

To capture the Silicon distribution behavior along the melt zone, the Mass Transport Equation is used:

$$\frac{\partial c}{\partial t}+u\frac{\partial c}{\partial r}+\frac{v}{r}\frac{\partial c}{\partial \varphi}+w\frac{\partial c}{\partial z}=\alpha_C\left(\frac{1}{r}\frac{\partial}{\partial r}\left(r\frac{\partial c}{\partial r}\right)+\frac{1}{r^2}\frac{\partial^2 c}{\partial \varphi^2}+\frac{\partial^2 c}{\partial z^2}\right) \qquad (2\text{-}5)$$

α_c is the solutal diffusivity.

2.3.4 Continuity Equation

Finally, the Continuity Equation is applied as:

$$\frac{\partial \rho}{\partial t}+\frac{1}{r}\frac{\partial}{\partial r}(\rho r u)+\frac{1}{r}\frac{\partial(\rho v)}{\partial \varphi}+\frac{\partial(\rho w)}{\partial z}=0 \qquad (2\text{-}6)$$

2.3.5 Gravitational Body Force - G-Jitter

Normally, under the terrestrial condition, the gravitational body force is expressed in terms of a constant terrestrial gravity and thermal coefficient. β_T. However, since we are dealing with g-jitter and multi-species, the terrestrial gravity constant will vary and the solutal expansion coefficient β_c will be considered as well. Therefore, the general form of the gravitational body force will be:

$$F_z^g = -\rho_o g(t)[\beta_T(T - T_m) + \beta_C(C - C_o)] \qquad (2\text{-}7)$$

Note: since the model dimensions are very small and the gravitational environments are very small, i.e., microgravity, the difference in the resulting inertia within the solvent regime is very small. Consequently, this leads to negligible density difference within the solvent region. Therefore, it is valid to apply the Boussinesq approximation under the circumstances of the current analysis [32].

In a typical micro-gravity environment, the residual acceleration experienced by the spacecraft is composed of a steady component and a time-dependent component acting on the 3D. The magnitude of the time-dependent component is much greater than that of the steady state component. However, this study will analyze the effect of the two components extensively. Therefore, in this report the general form of the gravitational effect will be taken as:

$$g(t) = g_{st} + g_{vib} \qquad (2\text{-}8)$$

Where, $g_{vib} = \sum_{i=1}^{n} A_o \sin(2\pi f t)$

In this form g_{st} is the static or steady state gravity, g_{vib} is the vibration gravity or g-jitter as a function of the summation of Amplitude of the damping gravity A_o, frequency f in Hz and time t, for all the terms of g-jitter. In simple harmonic g-jitter, the vibrational gravity consist of one term only, i.e. n = 1.

2.4 Dimensional Analysis

Dimensional analysis is a tool for obtaining information about physical systems too complicated for full mathematical solutions to be feasible. In order to obtain a simplified set of equations, which can represent the physical model in a general format, dimensionless variables are used.

Non-dimensionalization is the full removal of units from a mathematical equation by a suitable substitution of variables. This technique can reduce the number and complexity of experimental variables. This leads to a better understanding of results so they may be applied appropriately in upcoming research. Note; detailed step non-dimensionalization is included in Appendix C. In our model the equations were rendered non-dimensional using the following term:

$$r = Rd,\ z = Zd,\ u = Uu_o,\ v = Vu_o,\ w = Wu_o,\ T - T_o = \Delta T\theta,$$

$$c - c_o = \Delta cC,\ p = \frac{P\mu u_o}{d},\ t = \frac{\tau d}{u_o} \qquad (2\text{-}9)$$

Where d is the reference diameter, u_o is the reference velocity, R, Z, U, V and W are non-dimensional radial, angular and axial coordinates, non-dimensional radial, angular and axial components of velocity, respectively. P is the non-dimensional hydrodynamic pressure, θ is the dimensionless temperature, C is the dimensionless solute concentration, and T_o is the reference temperature (it assumed to be the melt temperature of the Ge).

Using the above non-dimensional parameters, the non-dimensional differential equations are obtained as highlighted in the following sub-section.

2.4.1 Navier-Stockes Equations

r - Component

$$\mathrm{Re}\left[\frac{\partial U}{\partial \tau} + U\frac{\partial U}{\partial R} + \frac{V}{R}\frac{\partial U}{\partial \varphi} + W\frac{\partial U}{\partial Z} - \frac{V^2}{R}\right] = -\frac{\partial P}{\partial R} + \left(\frac{1}{R}\frac{\partial}{\partial R}\left(\frac{\partial U}{\partial R}\right) + \frac{1}{R^2}\frac{\partial^2 U}{\partial \varphi^2} + \frac{\partial^2 U}{\partial Z^2}\right) \qquad (2\text{-}10)$$

φ - Component

$$\mathrm{Re}\left[\frac{\partial V}{\partial \tau} + U\frac{\partial V}{\partial R} + \frac{V}{R}\frac{\partial V}{\partial \varphi} + W\frac{\partial V}{\partial Z} + \frac{UV}{R}\right] = -\frac{1}{R}\frac{\partial P}{\partial \varphi} + \left(\frac{1}{R}\frac{\partial}{\partial R}\left(\frac{\partial V}{\partial R}\right) + \frac{1}{R^2}\frac{\partial^2 V}{\partial \varphi^2} + \frac{\partial^2 V}{\partial Z^2}\right) \qquad (2\text{-}11)$$

z - Component

$$\mathrm{Re}\left[\frac{\partial W}{\partial \tau}+U\frac{\partial W}{\partial R}+\frac{V}{R}\frac{\partial W}{\partial \varphi}+W\frac{\partial W}{\partial Z}\right]=-\frac{\partial P}{\partial Z}+\left(\frac{1}{R}\frac{\partial}{\partial R}\left(\frac{\partial W}{\partial R}\right)+\frac{1}{R^2}\frac{\partial^2 W}{\partial \varphi^2}+\frac{\partial^2 W}{\partial Z^2}\right)+\frac{1}{\mathrm{Re}}(\mathrm{Gr_T}\theta-\mathrm{Gr_c}C) \qquad (2\text{-}12)$$

Where, Re, Gr_T, Gr_c are the Reynolds number, the thermal Grashof number, and the solutal Grashof number, respectively. The last two variables are a function of gravity, which is also a function of static and g-jitter gravity forms. Therefore, further non-dimensionalization of these variables is included in this analysis. Table 2- 2 defines some of these variables.

Name	Definition	Parameter
Reynolds	$\frac{\text{inertia force}}{\text{viscous force}}$	$\mathrm{Re}=\frac{\rho u_o D}{\mu}$
Prandtl	$\frac{\text{momentum}}{\text{thermal diffusivities}}$	$\mathrm{Pr}=\frac{c_p\mu}{\kappa}$
Schmidt	$\frac{\text{viscous force}}{\text{solutal diffusivity}}$	$Sc=\frac{\nu}{\alpha_c}$
Thermal Grashof	$\frac{\text{buoyancy force}}{\text{viscous force}}$	$Gr_T=\frac{\beta_T \Delta T g^* D^3 \rho^2}{\mu^2}$
Solutal Grashof	$\frac{\text{buoyancy force}}{\text{viscous force}}$	$Gr_c=\frac{\beta_C \Delta T g^* D^3 \rho^2}{\mu^2}$
Hartmann	$\frac{\text{magnetic force}}{\text{Viscous force}}$	$Ha=\lvert B_o\rvert D\sqrt{\frac{\sigma}{\mu}}$

Table 2- 2: Non-Dimensional Parameters

Where g* is expressed as:

$$g^*=\frac{g_{st}}{g_o}+\sum_{i=1}^{n}\frac{A_o}{g_o}\sin(2\pi ft) \qquad (2\text{-}13)$$

g_o is the gravitational magnitude at terrestrial condition

2.4.2 Energy Equation

To describe the change in temperature throughout the model the energy equation is used:

$$\mathrm{Re}\,\mathrm{Pr}\left[\frac{\partial\theta}{\partial\tau}+\mathrm{U}\frac{\partial\theta}{\partial\mathrm{R}}+\frac{\mathrm{V}}{\mathrm{R}}\frac{\partial\theta}{\partial\varphi}+\mathrm{W}\frac{\partial\theta}{\partial\mathrm{Z}}\right]=\left(\frac{1}{\mathrm{R}}\frac{\partial}{\partial\mathrm{R}}\left(\frac{\partial\theta}{\partial\mathrm{R}}\right)+\frac{1}{\mathrm{R}^2}\frac{\partial^2\theta}{\partial\varphi^2}+\frac{\partial^2\theta}{\partial\mathrm{Z}^2}\right) \qquad (2\text{-}14)$$

2.4.3 Continuity Equation

The continuity equation must be satisfied and have the following form

$$\frac{\partial\,\mathrm{Re}}{\partial\tau}+\mathrm{Re}\left[\frac{1}{\mathrm{R}}\frac{\partial\mathrm{U}}{\partial\mathrm{R}}+\frac{1}{\mathrm{R}}\frac{\partial\mathrm{V}}{\partial\varphi}+\frac{\partial\mathrm{W}}{\partial\mathrm{Z}}\right]=0 \qquad (2\text{-}15)$$

2.4.4 Mass Transport Equation

In order to account for the silicon diffusion into the melt, the mass transfer equation must be solved as well;

$$\mathrm{Re}\,\mathrm{Sc}\left[\frac{\partial\mathrm{C}}{\partial\tau}+\mathrm{U}\frac{\partial\mathrm{C}}{\partial\mathrm{R}}+\frac{\mathrm{V}}{\mathrm{R}}\frac{\partial\mathrm{C}}{\partial\varphi}+\mathrm{W}\frac{\partial\mathrm{C}}{\partial\mathrm{Z}}\right]=\left(\frac{1}{\mathrm{R}}\frac{\partial}{\partial\mathrm{R}}\left(\frac{\partial\mathrm{C}}{\partial\mathrm{R}}\right)+\frac{1}{\mathrm{R}^2}\frac{\partial^2\mathrm{C}}{\partial\varphi^2}+\frac{\partial^2\mathrm{C}}{\partial\mathrm{Z}^2}\right) \qquad (2\text{-}16)$$

2.5 Boundary Conditions

The boundary conditions used in this analysis can be expressed as follows:

1. At the vertical wall of the ampoule (in the source, solvent, and substrate) as well as on the top and bottom of the ampoule:

$$\mathrm{U=V=W=0\ (Non\text{-}slip\ condition)\ and}\ \frac{\partial\mathrm{C}}{\partial\mathrm{R}}=0 \qquad (2\text{-}17)$$

2. Silicon in the source and at the dissolution interface:

$$C=C_1=15\% \qquad (2\text{-}18)$$

3. Silicon concentration at the growth interface:

$$C=C_2=2\% \qquad (2\text{-}19)$$

Note, the concentration values are obtained from the Ge-Si phase diagram discussed in detail in reference [33] and shown in Figure 2.4. The model uses the latent heat of the material and the continuity of the velocities and temperature to be exchanged along the solid-liquid interface. This is given by:

$$\kappa\frac{\partial T}{\partial z}-\kappa_s\frac{\partial T_s}{\partial z}=\rho_s L_f\left(w_s-w_{\text{int}\,erface}\right) \qquad (2\text{-}20)$$

where L_f is the latent heat.

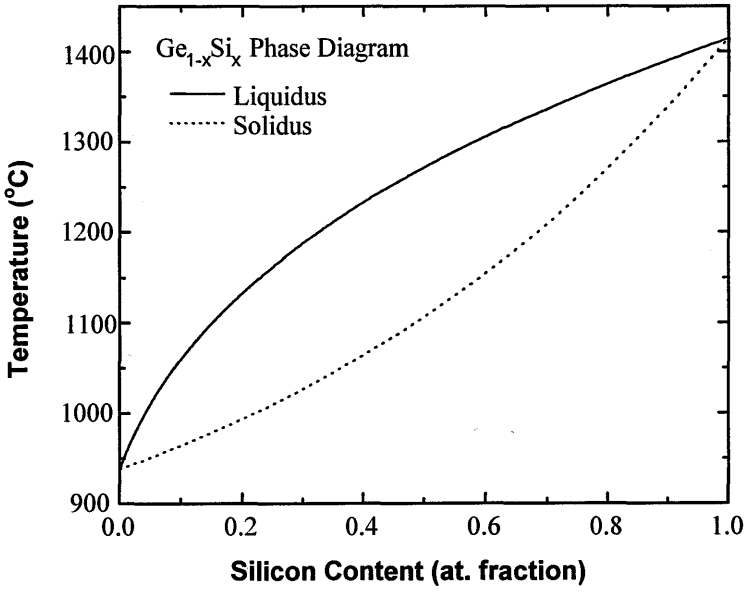

Figure 2- 4: Ge-Si phase Diagram

2.6 Numerical Solution

Equations (2-20) to (2-22) and (2-24) to (2-26), representing the non-dimensional governing equations along with the boundary conditions, represented by equations (2-27) to (2-29), are solved numerically by the Galerkin finite element method. The commercial CFD software, FIDAP, is built on this method. Therefore, it will be used as a means to solve the above equations.

Initially, the three-dimensional meshed model is created using a Fluent software, Gambit, which is used to generate detailed meshes for complicated geometries. After the physical model and its mesh scheme are generated by Gambit, the model is exported to the commercial computational code FIDAP. FIDAP is a general-purpose software package for the simulation of incompressible or compressible flows. It offers numerous physical and numerical models for simulations ranging from highly viscous laminar flows to fully turbulent flows. In addition, it provides robust calculations. FIDAP's capabilities include fluid flow, heat and free surface modeling. FIDAP has the capacity to perform all steps of a fluid flow simulation, which include pre-processing including model building, mesh generation, data input, solution, and post processing. A complete input to the FIDAP program, including the subroutine of the g-jitter body force, is included in Appendix D.

The mathematical model for the growth process includes the energy equation, mass transport equation, momentum equations (non-linear Navier-Stokes) and the continuity equation. To be able to solve for this mathematical model, certain assumptions have to be made. The fluid is assumed to be an incompressible viscous Newtonian fluid. The Boussinesq approximation is introduced to account for density variations. Also, since the growth rate is small, 4mm/day, the quasi-steady-state model, where the transient effect of heat, mass and fluid are considered small enough to be negligible, is used. The quasi-steady-state assumption is valid under micro-gravity

only, therefore, the time dependent terms in the above mathematical model will be dropped out. As far as the g-jitter is concerned, the gravitational fluctuation is a function of time, therefore, the transient effect of heat, mass and fluid will be considered. Nevertheless, a translating growth interface will not be considered since only the silicon distribution along a stable growth interface is of interest to our analysis. As a result, the requirement to analyze two-phase interaction is eliminated.

2.7 Finite Element Analysis

The finite element method (FEM) was used to solve partial differential equations (PDE). Solutions were approximated by either eliminating the differential equation completely (steady state problems), or rendering the PDE into an equivalent ordinary differential equation, which is solved using standard techniques such as finite differences in our case. This method has proven to be an efficient technique for the simulation of crystal growth processes because of its versatility. The well-known mixed velocity/ pressure finite element formulation involves six unknowns (u, v, w, T, C and p), and requires significant computational effort and complex programming. The equations described above, along with the boundary conditions, are solved using the Galerkin method of Weight Residual. This method enables the computation of crystal properties for both steady and transient simulation while taking into consideration additional body forces such as the fluctuation of the gravitational forces. However, because of the large scale of the transient simulation, a segregated algorithm is used to solve sequentially for the non-linear system of matrix equations arising from the FEM discretization of the flow equations. For steady state simulation, fully coupled equations described by the global system matrix are obtained using the above finite element method. A fully coupled solution approach is cost effective in comparison with the segregated algorithm solution. Yet, the fully coupled approach is limited by the peripheral storage requirement to process and store the variables of the global system matrix

representing the discretized problem, which can be expressed as a combination of the CPU and peripheral disk storage. Therefore, throughout our analyses, the segregated solver will be adopted. Because of this restriction on the size of the simulation, the convergence criterion was determined to be 10^{-4} for all velocity, temperature and concentration variations.

Note: the convective terms represented by the gravitational force couples the energy and the transport equations. Since the g-jitter forces have a very weak effect in the Navier-Stokes equations, the energy equation and the solute transport equations are decoupled. Therefore, one would not expect the Silicon concentration distribution to be a function of the thermal distribution. To avoid decoupling these equations in order to take the gravitational fluctuation into consideration, the g-jitter force will be imposed on the z-momentum equation as a separate additional force in the case of synthetic gravity and along the three axes in the case of real g-jitter. This is possible to implement through the FIDAP software.

2.8 Mesh Sensitivity

To validate the results obtained through the commercial software used for the analysis, FIDAP [34], mesh dependency had to be tested. In this study, Gambit software is used to generate three-dimensional meshes for our model. Once the geometry and the mesh are done, they are exported to the commercial computational code FIDAP where the mathematical model was solved. The initial mesh sensitivity analysis was performed by Jaber et al. [35] for the same model on the solvent entity. The Nusselt number was used as a mean to measure the mesh sensitivity. As a result, the final finite element mesh used for the static micro-gravity simulations was an optimum number of 33,000 8-node hexahedral elements, where the Nusselt number deviation does not exceed 10^{-4}.

However, special consideration had to be given for the mesh sensitivity of the g-jitter simulations. Since CPU and peripheral disk storage restrict FIDAP analysis, it was impossible to run g-jitter simulation with the above meshing criterion. Therefore, a second mesh sensitivity analysis was performed to account for the size of the analysis. As a result, the number of elements was dropped down to 3,060. Since our main concern is the status of the properties at the growth interface, the average specie concentration was calculated using various mesh sizes. As shown in Figure 2- 5, the species variation is in the range of 10^{-6} %C as the number of mesh is increased or decreased relative to 3,060. Therefore, the employed mesh is concluded to be good enough to validate our results.

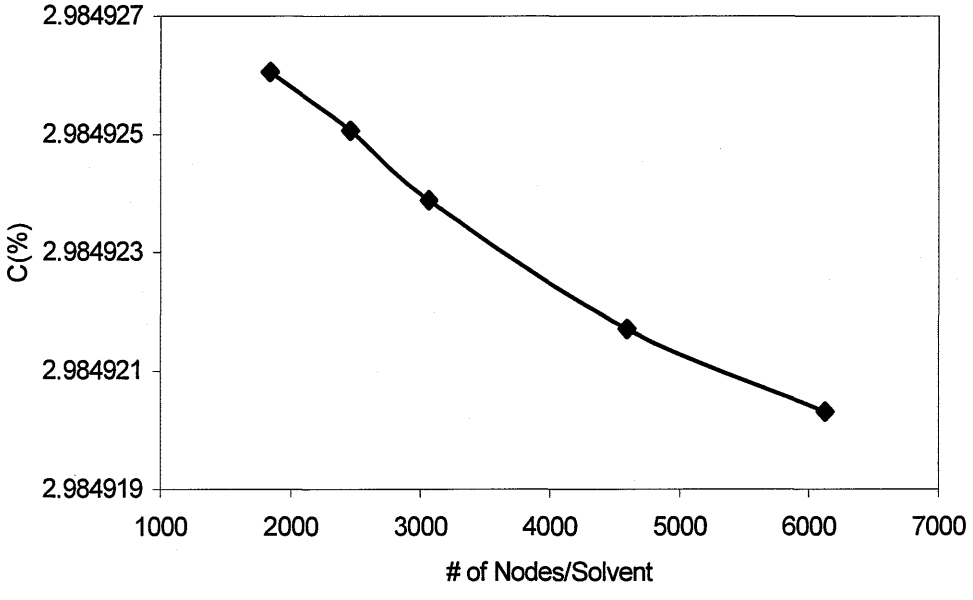

Figure 2- 5: Mesh Sensitivity Analysis

Chapter 3

Effect of Static Gravity

The main objective of this chapter is to study the effect of reduced gravity on the growth of $Ge_{0.98}Si_{0.02}$ by using the THM in space conditions. In order to understand the flow behavior under a space station environment, the influence of static gravity has to be studied first. Therefore, this chapter will include a detailed analysis of the effect of the convective flow under terrestrial conditions, i.e., worst growth conditions, and under reduced gravity conditions. Since the final goal of this research is to analyze the effect of g-jitter imposed on the sample during the crystal growth in space, it is best to analyze a simulation of crystal growth under static gravity similar to that imposed in space. Based on previously collected data, a realistic static gravity encountered in a space environment is within the range of $10^{-6}g_o$. Also, to further understand the effect of varying the static microgravity during the crystal growth, other growth environments, such as $10^{-4}g_o$ and $10^{-3}g_o$, were studied as well.

3.1 Terrestrial and Zero Gravity Conditions

To better understand the flow phenomenon and the resulting Silicon distribution along the growth interface, the driving forces have to be examined. The computed flow field, solute concentration distribution and temperature distribution are shown in Figure 3-1 and 3-2 for the terrestrial and zero gravity cases, respectively.

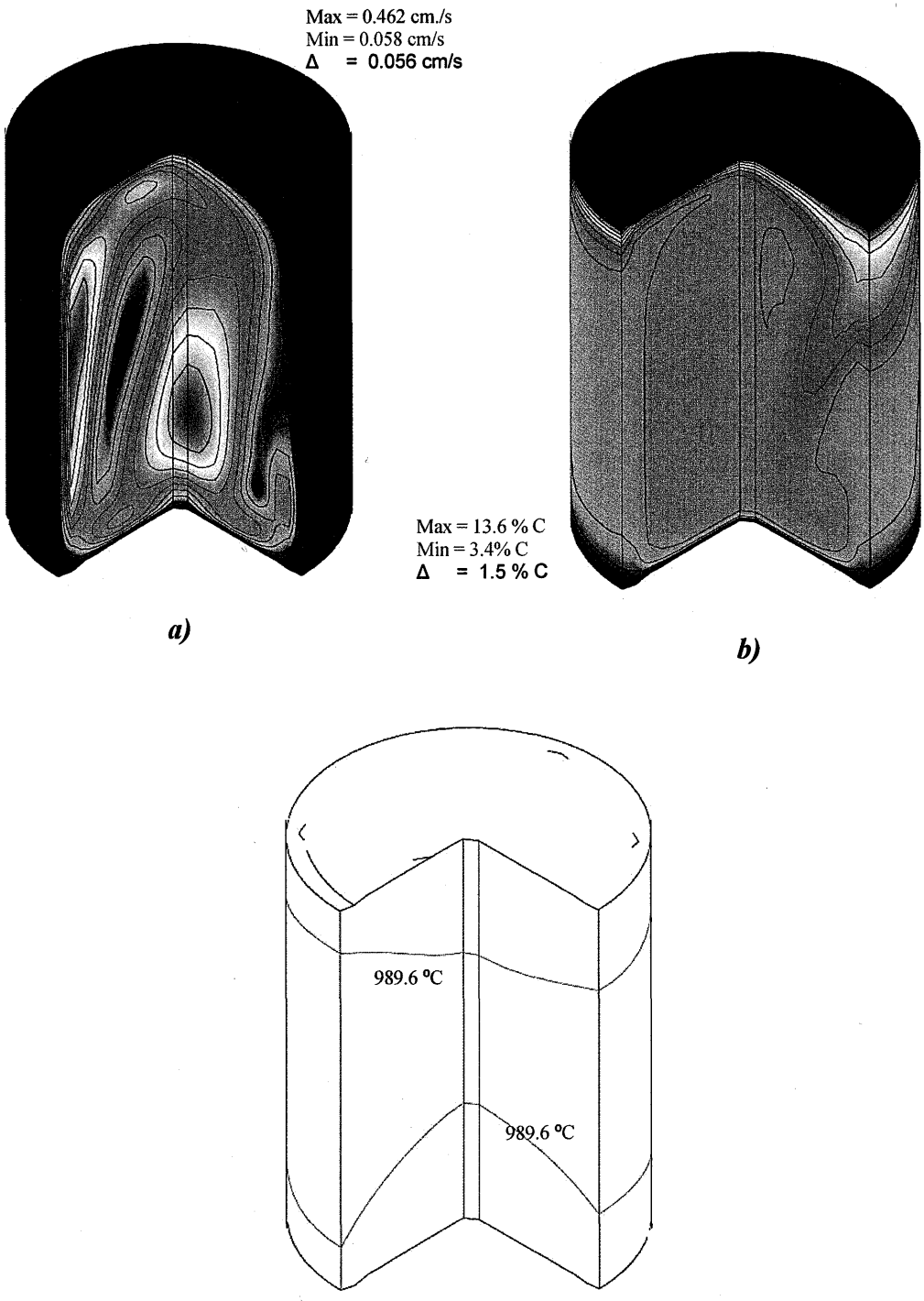

Figure 3- 1: Resulting Solvent Properties under Terrestrial Conditions, g = 1 g_o

a) Flow Profile
b) Silicon Concentration Distribution
c) Thermal Profile

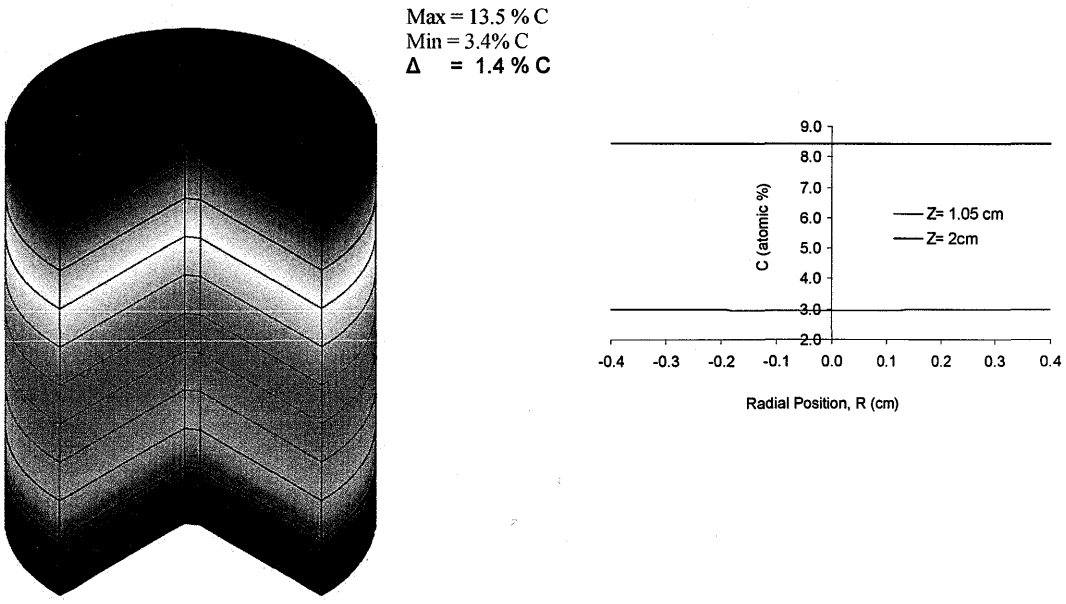

a)

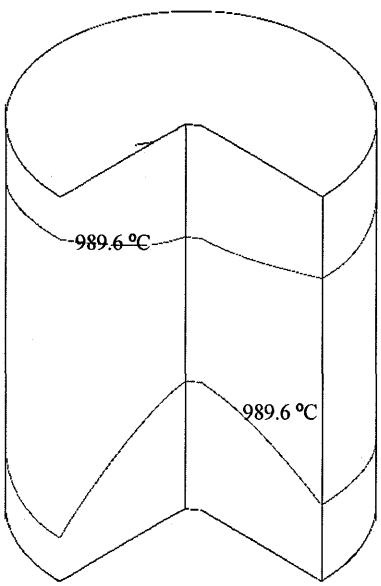

b)

Figure 3- 2: Resulting Solvent Properties in the absence of gravity, ie, zero gravity

a) Silicon Concentration Distribution

b) Thermal Profile

As mentioned previously, to obtain a realistic analysis, non-uniform heating is considered. The resulting thermal profile is seen in Figure 3-1c and 3-2b for terrestrial and zero gravity conditions, respectively. In both cases the thermal distribution is convex near the source and concave near the growth interface. Furthermore, in both cases the thermal variation is small. The reason behind such behavior is that the heat transfer process in the semiconductor materials is dominated by conduction rather than convection. Under zero gravity, convection is eliminated. SiGe is a semiconductor with a low Prandlt number. Therefore, heat transfer dominated by conduction rather than convection is expected in this case. However, under terrestrial growth conditions, convection in the solvent region is not strong enough to effect thermal variation. Convection is driven by the buoyancy effect in terms of the gravitational forces and the horizontal thermal gradients between the sides of the sample and mid-solvent. Consequently, the terrestrial gravitational force does not have an effect on the heat transfer process.

On the other hand, the thermal gradient existing between the feeding source and the growth interface has a direct influence on the thermal diffusion of silicon. Also, the thermal gradient existing between the sides of the solvent and mid-solvent has direct influence on the flow convection. The Travelling Heater method relies on these thermal gradients to drive the silicon migration. However, this migration can be categorized to be a result of thermal convection due to the buoyancy effect, induced by the thermal gradient, as well as the gravitational effect, and thermal diffusion, induced by thermal gradients and the molecular diffusion of silicon into germanium.

Under terrestrial conditions, the complexity of the flow due to buoyancy-induced flow can be seen clearly in Figure 3-1a. A maximum flow of 0.393 cm/s is attained along the middle of the solvent region and 0.29 cm/s near the growth interface. As a result, the silicon distribution along

the middle of the solvent region was obtained to vary between 7.94 %C and 5.81 %C. This concentration decreases to a range of 7.35 %C to 4.38 %C near the growth interface.

As indicated in Figure 3-2, in the absence of the gravity effect, the convective flow is eliminated. This leaves us with pure diffusion of silicon to the growth interface. As a result, the concentration distribution has a linear behavior. Note, for this particular case, the flow pattern is not supplied because there is no convective flow in the solvent regime at all. As a result, the silicon distribution, captured in Figure 3-2a, is almost uniform within the range of 2.99 %C to 2.97 %C along the growth interface and between 8.42 %C to 8.43 %C along mid-solvent at Z = 2 cm. This case would be the ideal situation to obtain pure and highly defined crystal growth. However, in reality, there will always be a convective flow due to gravity gradients.

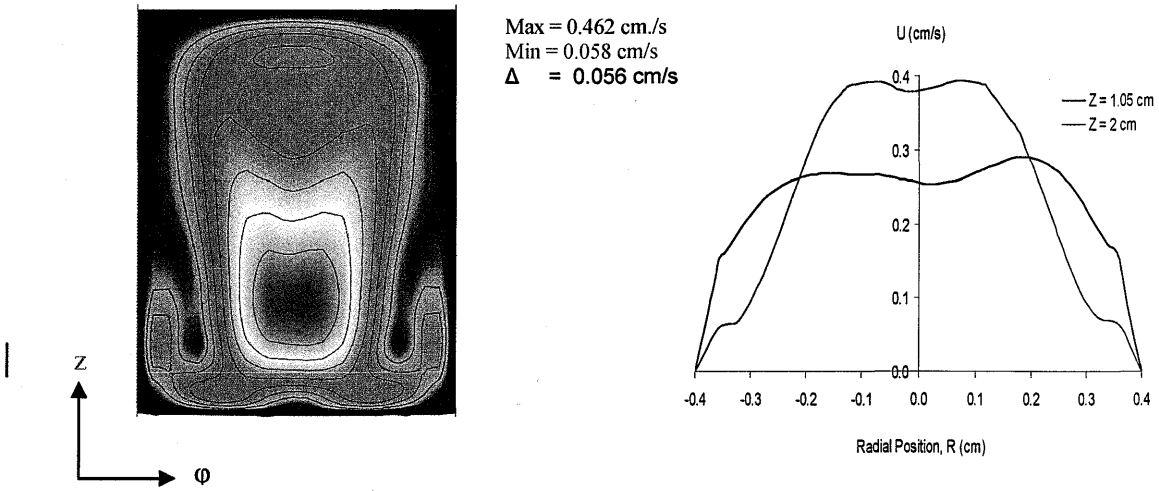

a) Flow, $\varphi = 0°$

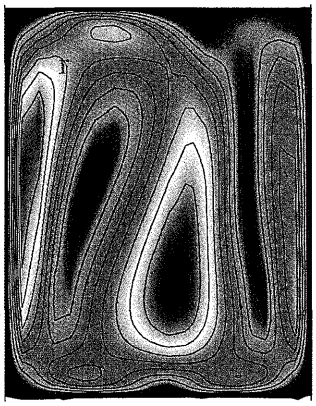

Max = 0.462 cm./s
Min = 0.058 cm/s
Δ = 0.056 cm/s

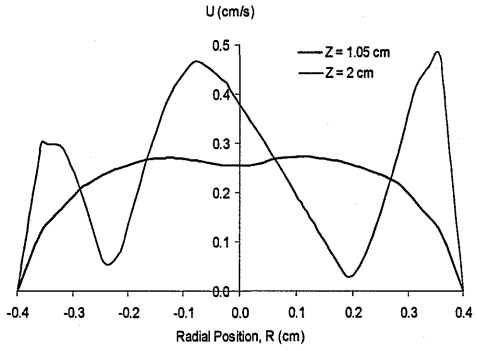

b) Flow, φ = 90°

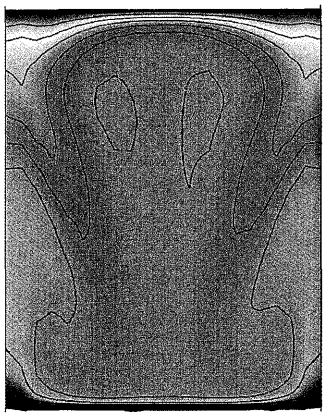

Max = 13.6 % C
Min = 3.4% C
Δ = 1.5 % C

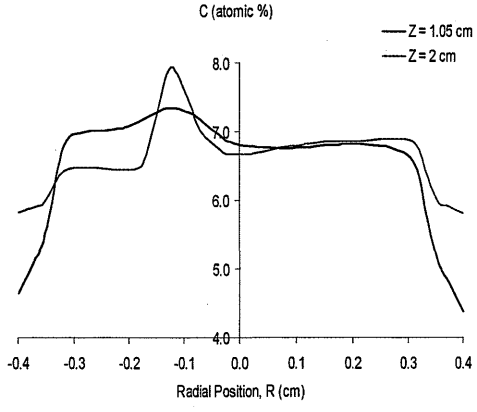

c) Si, φ = 0°

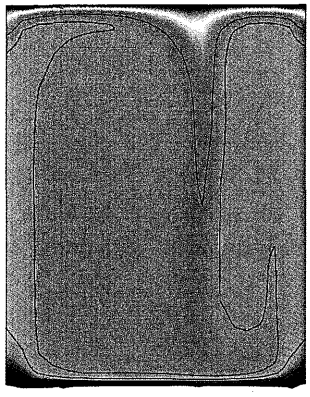

Max = 13.6 % C
Min = 3.4% C
Δ = 1.5 % C

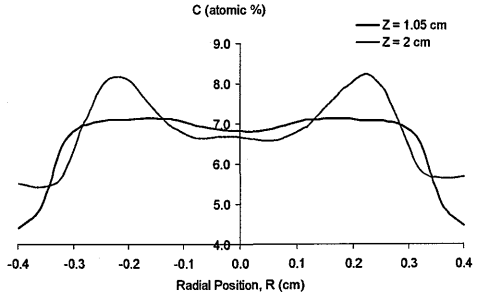

d) Si, φ = 90°

Figure 3- 3: Complexity of flow and Silicon distribution along the φ = 0 and φ =90 directions under terrestrial conditions

Under terrestrial conditions, the complexity of the flow is noted through Figure 3-3. The irregularity of the flow in the solvent regime can have an influence on the Silicon transportation. The flow pattern along the radial direction, where $\varphi = 0°$, is illustrated in Figure 3-3a. The flow pattern consists of two convective flow cells with each cell located symmetrically on each half of the solvent. However, Figure 3-3b shows the formation of three flow cells as the angle along the radial direction is moved 90° counter clockwise. In both directions the flow is noted to be more irregular at the center of the cells, where the stagnation of the flow cells is located. The combined effect of thermal gradient and gravity causes a convection pattern to form. Along this pattern the cold molten particles of silicon migrate from feeder source down the center of the solvent region towards the growth interface. This phenomenon controls the flow pattern of the silicon particles as well as the level of concentration. Under the acceleration of terrestrial gravity the silicon particles are forced to follow the flow of the cells formed within the solvent region. As a result, more silicon is forced to travel downward to the growth interface. Consequently, high silicon concentration build up is attained mainly near the middle of growth interface. The location along the growth interface with the highest silicon concentration is also noted to be the same as that with the highest flow intensity. This behavior is noted in figure 3-3a and b where the flow intensity along the radial direction at both mid-solvent and near the growth interface is relatively the highest near the center as well. Yet, non-symmetrical flow behavior about the z-axis still applies. Similarly, the silicon concentration is noted in figure 3-3c and d to build up non-symmetrically near the center of the growth interface. This is an indication that under terrestrial conditions the resulting convective flow is three dimensional and complex in nature. This behavior leads to a similarly complex silicon distribution as well.

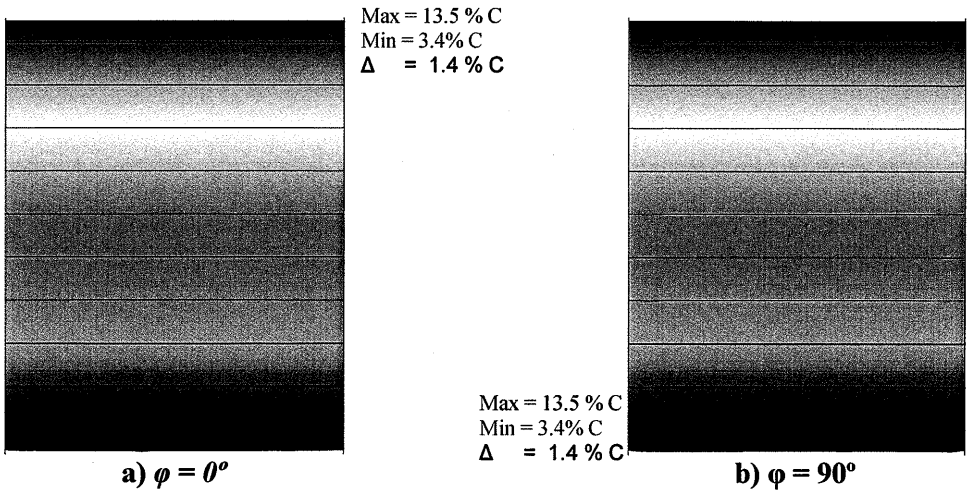

Figure 3- 4: Silicon distribution along the φ = 0° and φ =90° directions under zero gravity

As noted in Figure 3-4, in the absence of gravity, the silicon particles propagate downward with constant speed. There is no flow pattern to influence the migration of silicon. Therefore, it is safe to conclude that the silicon diffusion is two dimensional in nature.

Comparing the silicon concentrations in the absence of gravity to those obtained under terrestrial condition, it is noted that the silicon distribution at mid-solvent is higher in the absence of gravity. However, the silicon concentration is noted to be lower in the absence of gravity, near the growth interface. Such behavior is attained because more time is required in the absence of gravity to reach quasi-steady state compared to that under terrestrial condition. In the absence of gravity silicon is allowed to diffuse to the growth interface. While under terrestrial conditions, the gravitational forces accelerate the migration of silicon particles to the growth interface. As a result, there will be less silicon residue at mid-solvent under terrestrial conditions compare to the absence of gravity condition.

3.2 Reduced Gravity in Space, 10^{-6} g_o

A realistic static gravity encountered in space environment is within the range of $10^{-6}g_o$. Under such growth environment, the flow is weak. Yet it still exhibits some multi-cells complex behavior as noted in Figure 3-5a. Yet, according to Figure 3-5 b, the silicon distribution in this case is similar to that obtained in the absence of gravity. This is an indication that under realistic static gravity conditions silicon propagation to the growth interface is governed by diffusion. To confirm this behavior, the flow within the solvent regime has to be examined closely.

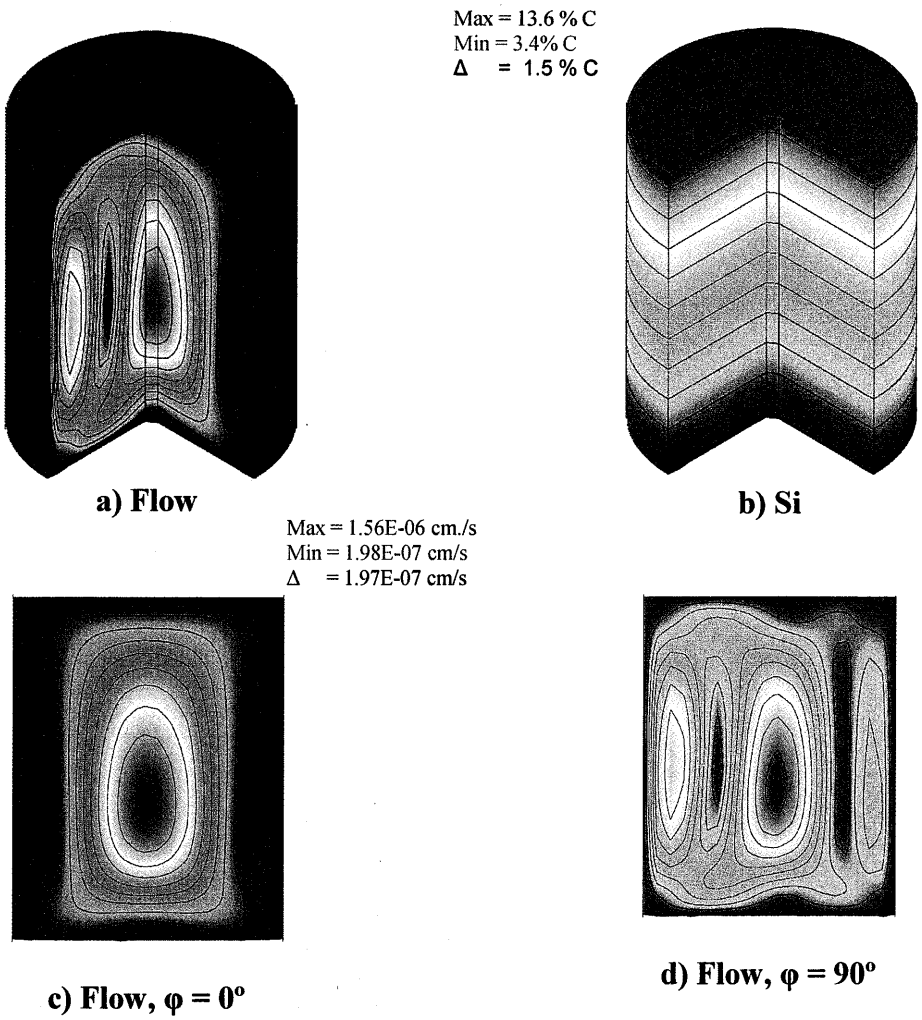

Figure 3- 5: Resulting Solvent Properties under micro-gravity of 10^{-6} g_o

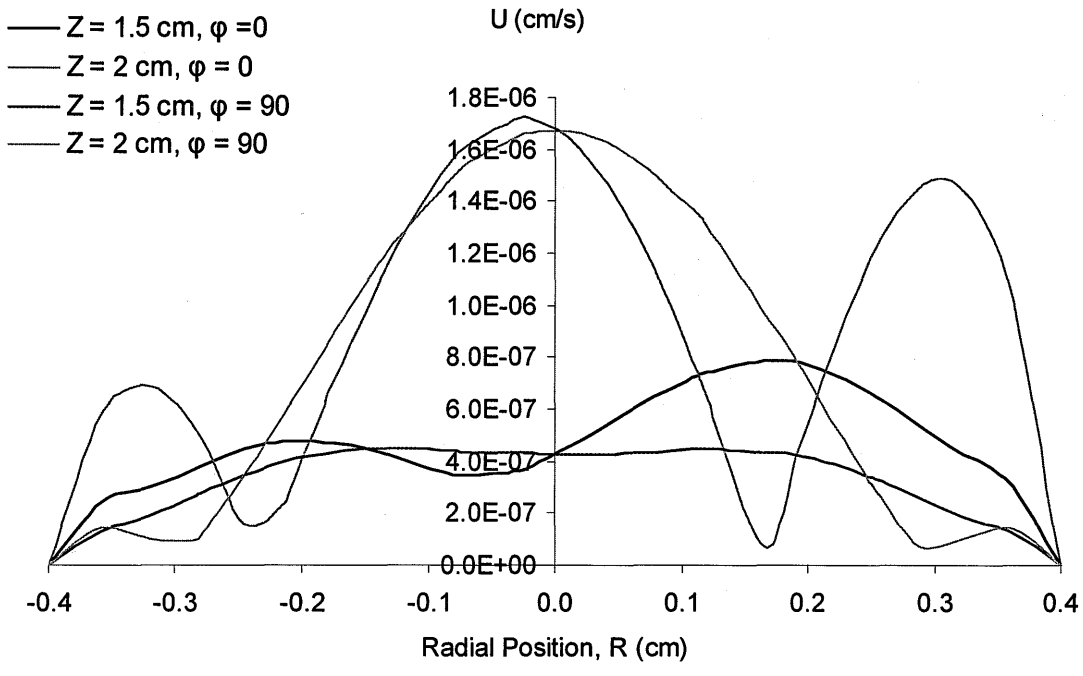

Figure 3- 6: Flow Profile at various locations and directions along the solvent regime under Micro-static gravity of 10^{-6} g_o

Another way to show the complexity of the flow is through figure 3-6. The irregularity of the flow in the solvent regime is expected to have an influence on the Silicon transportation. However, in our case the intensity of the convective flow is within the range of 10^{-6} cm/s. This intensity is relatively small compare to the flow intensity under terrestrial condition.

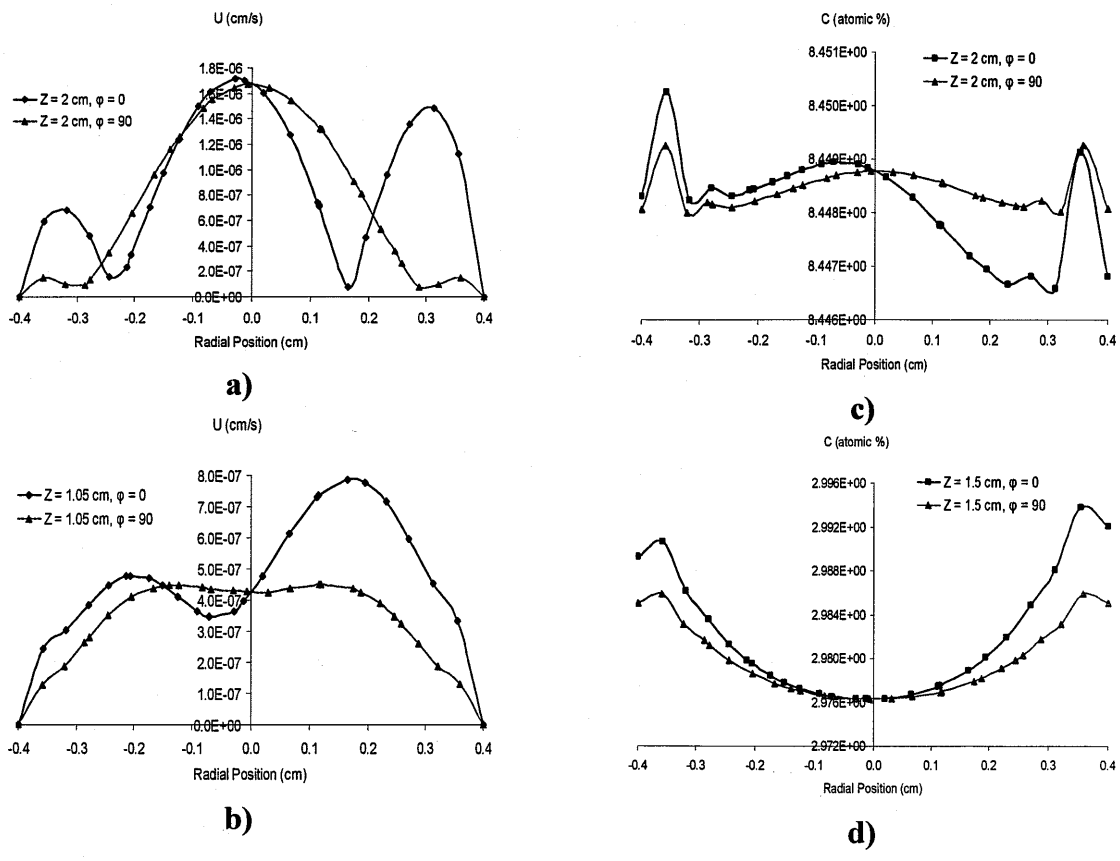

Figure 3- 7: Flow and Silicon Concentration Profiles along the solvent regime under micro-static gravity of $10^{-6}g_o$.

a) Flow at Mid-Solvent along $\varphi = 0^\circ$ and $\varphi = 90^\circ$ plans.
b) Flow near the growth interface along $\varphi = 0^\circ$ and $\varphi = 90^\circ$ plans.
c) Silicon distribution at Mid-Solvent along $\varphi = 0^\circ$ and $\varphi = 90^\circ$ plans
d) Silicon distribution near the growth interface along $\varphi = 0^\circ$ and $\varphi = 90^\circ$ plans.

By further studying figure 3-7, it is noted that the silicon distribution pattern is not the same as that of the flow pattern. Still, this figure demonstrates a complex three-dimensional behavior. As a matter of fact, the fluctuation of the silicon distribution within the solvent regime is also noted to be very weak compare to the flow fluctuation. Figure 3-7a and b indicate that there are two flow cells along $\varphi=0^\circ$ radial direction and three flow cells along $\varphi=90^\circ$ radial direction. In both directions the maximum flow intensity is the same 1.8×10^{-6} cm/s at mid-solvent and 8×10^{-7} cm/s near the growth interface. Furthermore, the flow fluctuation and complexity is also noted to

subside near the growth interface, as seen in figure 3-7b. However, the silicon distribution at mid-solvent and near the growth interface is within the range of 8.45 %C and 2.99 %C respectively. At both locations the silicon concentration fluctuates within a range of 10^{-3} %C regardless of the variation in the previously noted complexity of the flow fluctuations at these locations. Such fluctuation of silicon concentration is very minor in crystal growth.

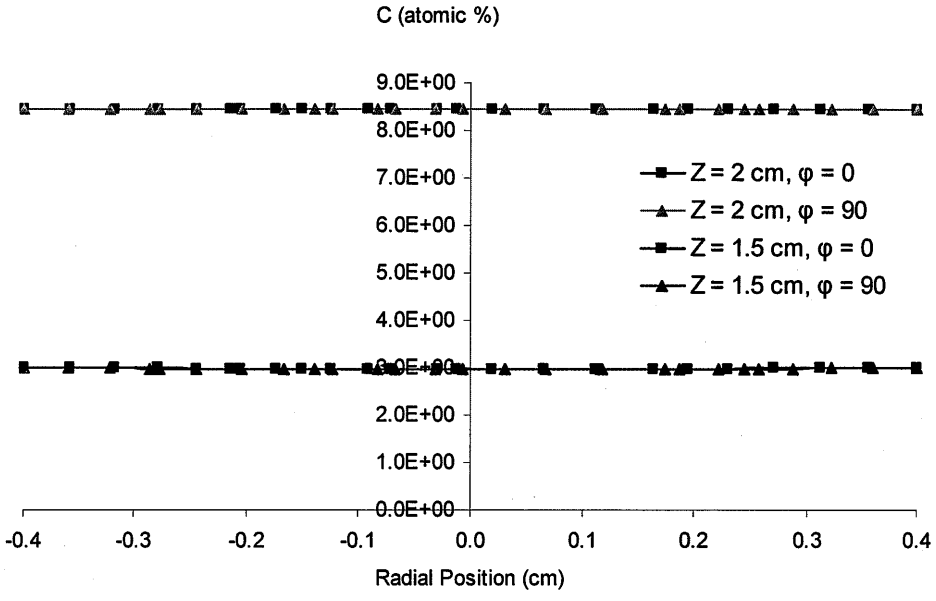

Figure 3- 8: Silicon Distribution Profile at various locations and directions along the solvent regime under micro-static gravity of $10^{-6}g_o$

This behavior can be further noticed in Figure 3-8, where silicon distribution at mid-solvent seems to be parallel to that near the growth interface. This figure clearly demonstrates that silicon migration is governed by diffusion. Therefore, it is valid to conclude that micro-gravity in the order of 10^{-6} g_o has negligible effect on the silicon migration.

3.3 Effect of Different Low Gravity Conditions

To further understand the effect of static micro-gravity on the flow and species behavior, other gravity levels have been investigated and compared to both the ideal zero gravity case and the terrestrial case. Based on the collected data from difference space environments, possible static

microgravity conditions that could be encountered in space were specified to be $10^{-3}g_o$ and $10^{-4}g_o$. Figure 3-9 to 3-14 provide a clear picture of the flow within the solvent region for growth conditions of $1g_o$, $10^{-3}g_o$, $10^{-4}g_o$, $10^{-6}g_o$ and zero gravity, respectively. While Figures 3-15 to 3-19 provide a clear picture of the silicon distribution within the solvent region for those growth conditions, respectively as well.

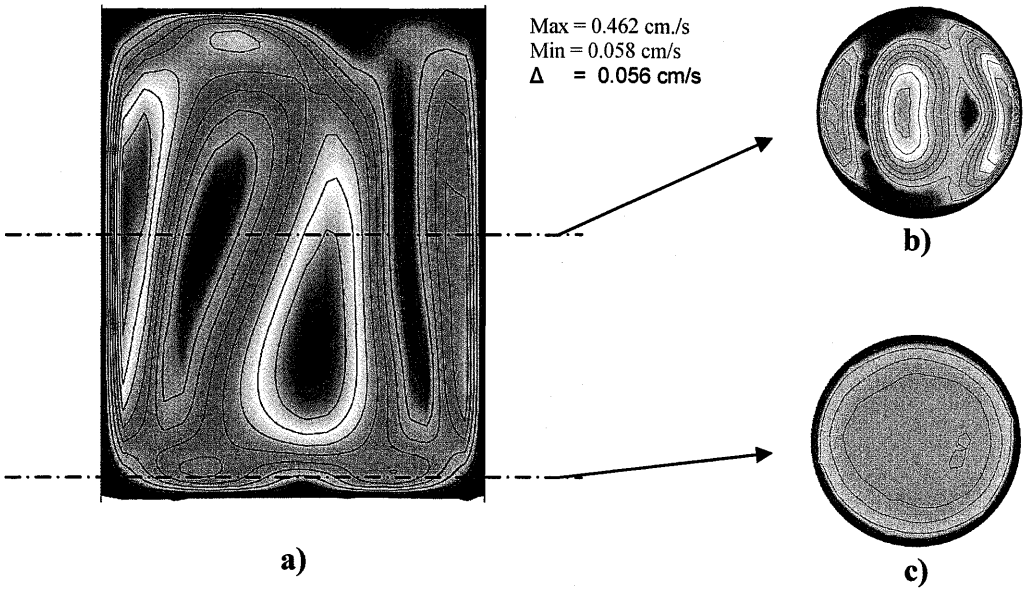

Figure 3- 9: Flow and silicon distribution under terrestrial growth conditions:

a) Along the Radial direction.
b) At mid-solvent along the horizontal plan z=2 cm
c) Near the interface along the horizontal plan z=1.5 cm

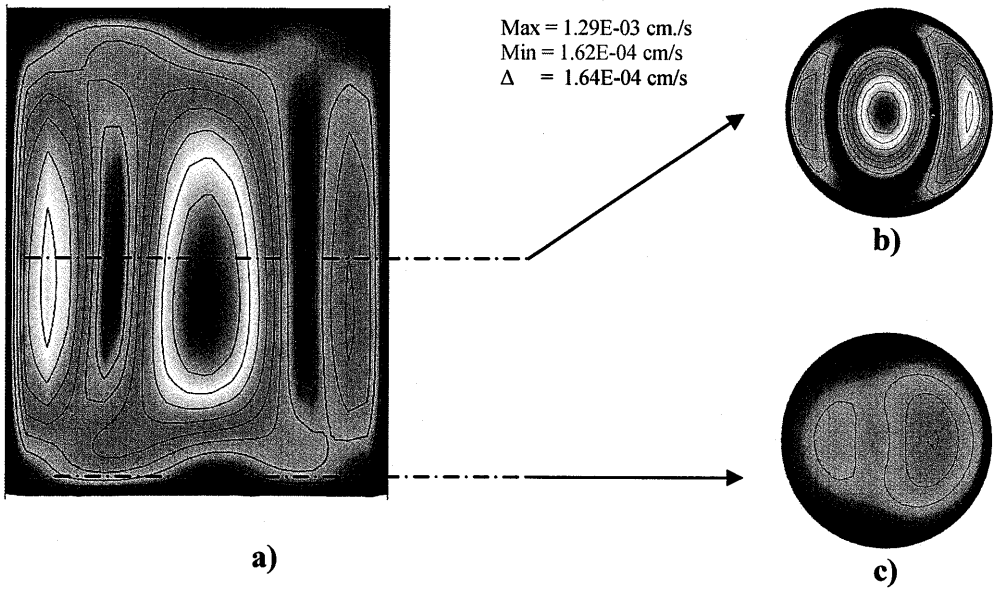

Figure 3- 10: Flow distribution under static micro-gravity of $10^{-3}g_o$:

a) Along the Radial direction.
b) At mid-solvent along the horizontal plan z=2 cm
c) Near the interface along the horizontal plan z=1.5 cm

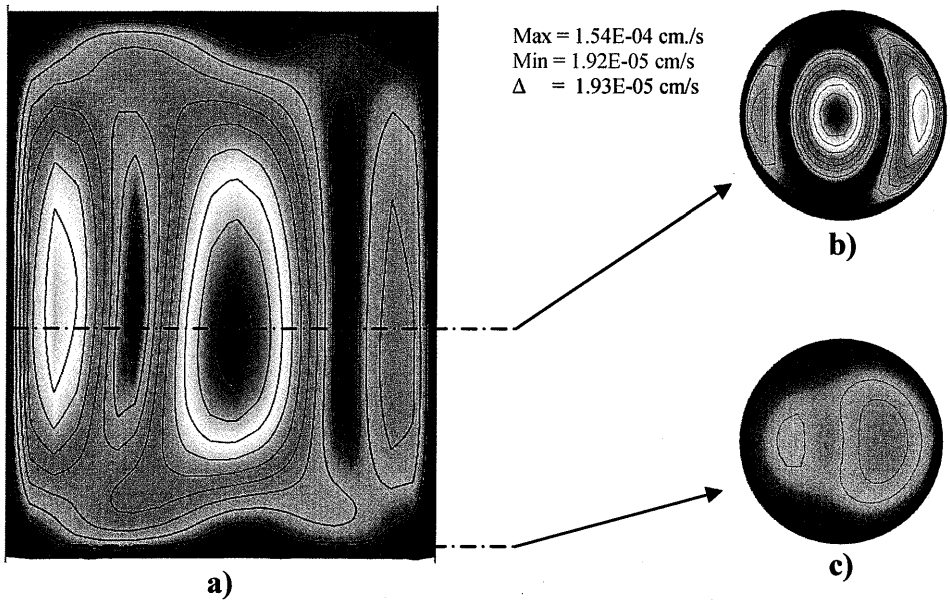

Figure 3- 11: Flow distribution under static micro-gravity of $10^{-4}g_o$:

a) Along the Radial direction.
b) At mid-solvent along the horizontal plan z=2 cm
c) Near the interface along the horizontal plan z=1.5 cm

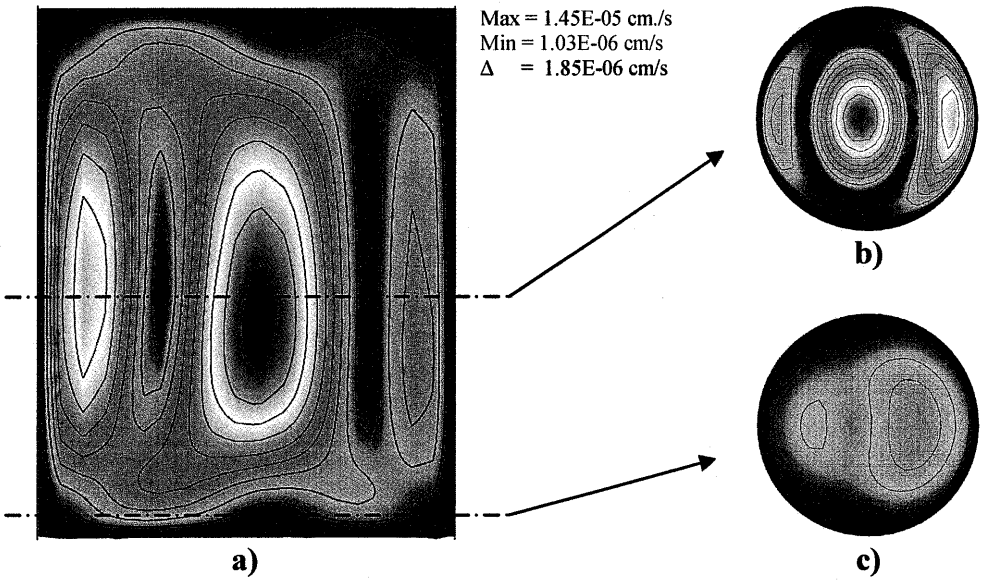

Figure 3- 12: Flow distribution under static micro-gravity of $10^{-6}g_o$:

a) Along the Radial direction.
b) At mid-solvent along the horizontal plan z=2 cm
c) Near the interface along the horizontal plan z=1.5 cm

Part a of Figures 3-9 to 3-12 show the flow variation along the radial directions. While, Parts b and c show the flow variation at mid-solvent and near the growth interface respectively. To understand the effect of varying the static microgravity on the flow behavior the results obtained under these different growth conditions will be examined extensively. In parts a of these figures, it is noted that the complex flow pattern is relatively the same for all cases and match the terrestrial growth condition flow pattern. The flow is still a three dimensional complex one with two convective flow cells along $\varphi = 0°$ radial direction and a three convective cells along the $\varphi = 90°$ radial direction. The non-symmetric flow behavior about the Z-axis is clearly observed in part b and c of these figures. It is also worth noting that, similar to the terrestrial case, the flow at mid-solvent, shown in parts b, is irregular and more complex compare to the flow near the growth interface, shown in parts c. Based on these observation it is valid to conclude that intensity of the micro-gravity does not have an effect on the shape of the flow profile.

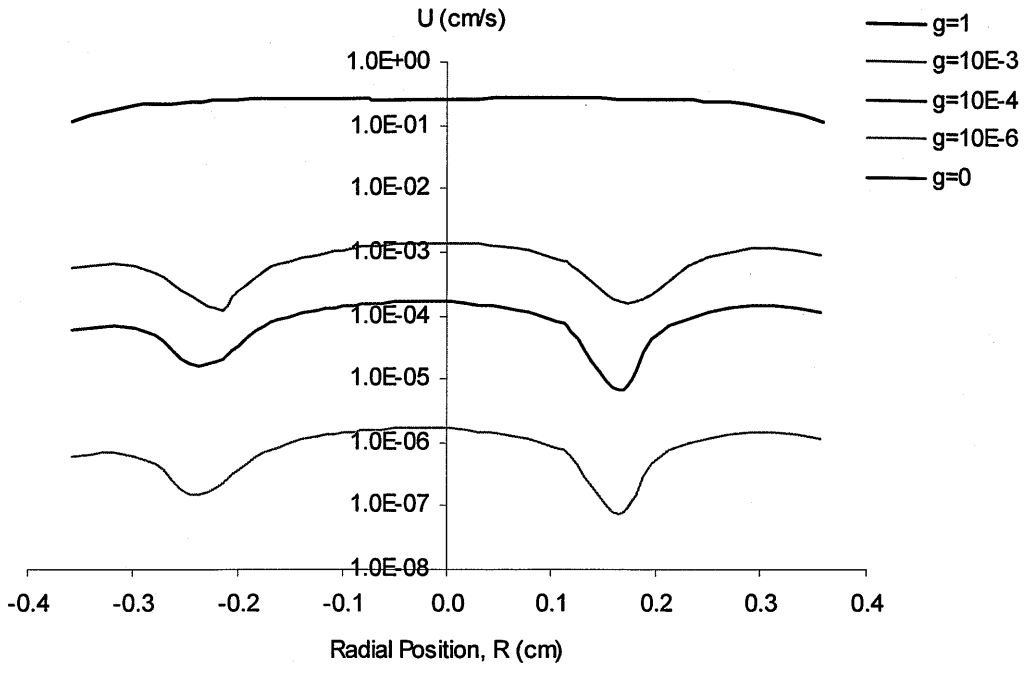

Figure 3- 13: Flow along the Radial plan, $\varphi = 0°$, at Mid-solvent under various gravitational growth conditions

The flow intensity was also examined as the static microgravity is decreased. Figure 3-13 indicates that the flow intensity is reduced accordingly to the micro-gravity level under which the crystal is grown. Under terrestrial conditions the flow intensity within the solvent regime was found to be within the range of 10^{-1} cm/s. By decreasing the static gravity from $1g_o$ to $10^{-3}g_o$, $10^{-4}g_o$, $10^{-6}g_o$ and $0g_o$, the flow intensity was noted to decrease to the range of 10^{-3} cm/s, 10^{-4} cm/s, 10^{-6} cm/s, and 0 cm/sec respectively. According to this observation it is valid to conclude that the intensity of the complex 3D flow is positively proportional to the intensity of the gravitational growth conditions.

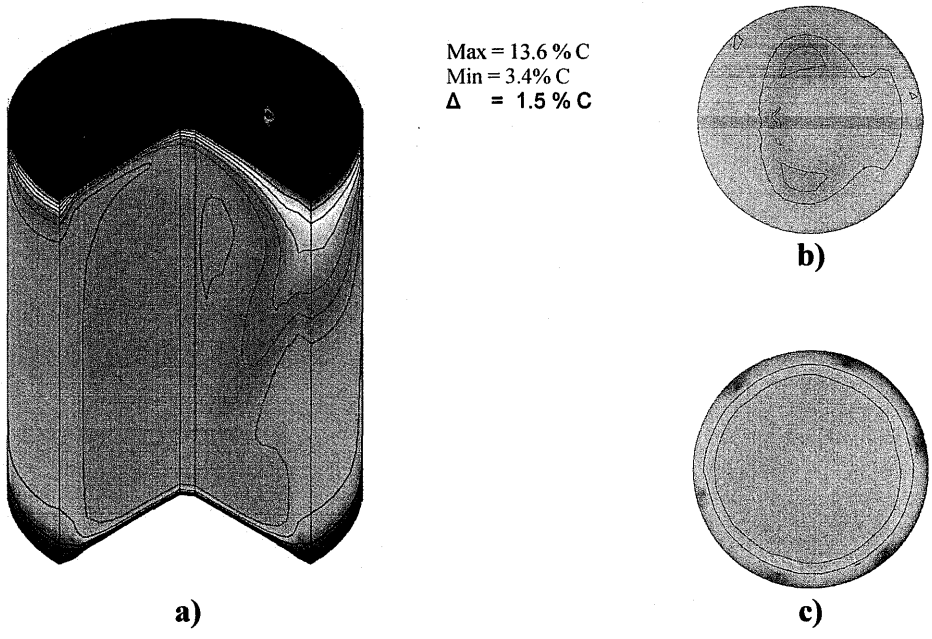

Figure 3- 14: Silicon distribution under terrestrial growth conditions:

a) 3D view of cross section at φ=0° and φ=90°
b) At mid-solvent along the horizontal plan z=2 cm
c) Near the interface along the horizontal plan z=1.5 cm

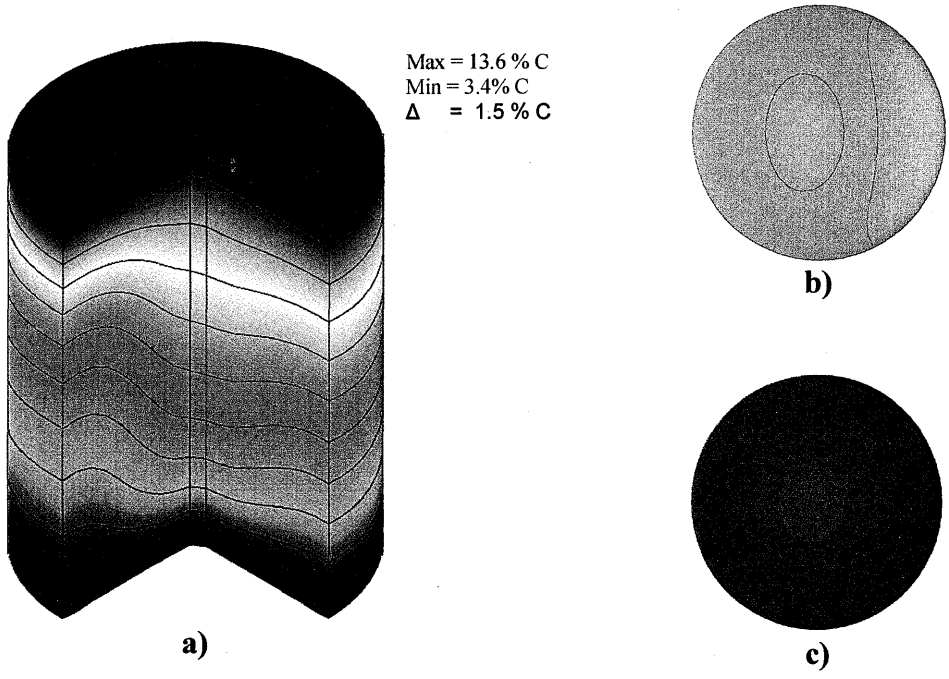

Figure 3- 15: Silicon distribution under static micro-gravity of $10^{-3}g_o$:

a) 3D view of cross section at φ=0° and φ=90°
b) At mid-solvent along the horizontal plan z=2 cm
c) Near the interface along the horizontal plan z=1.5 cm

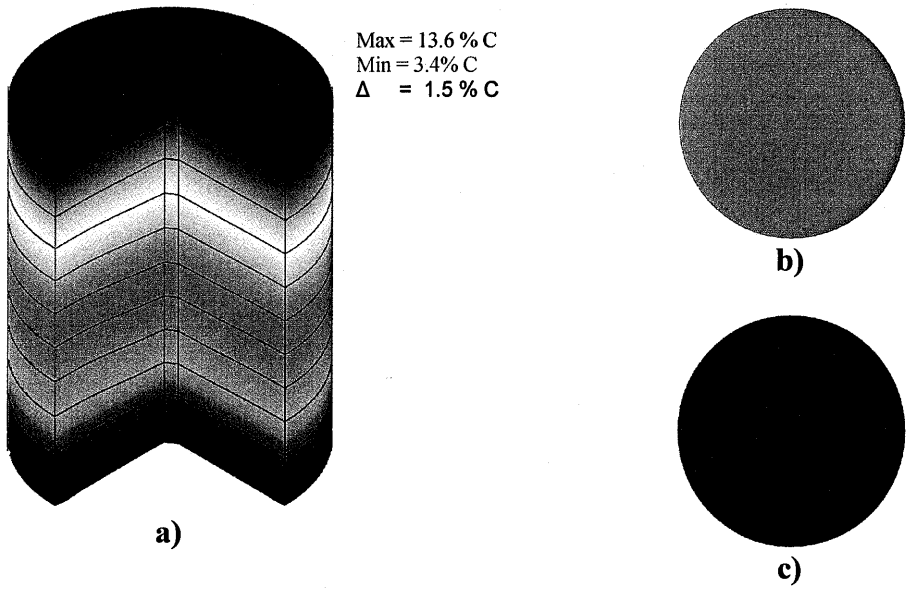

Figure 3- 16: Silicon distribution under static micro-gravity of $10^{-4}g_o$:

a) 3D view of cross section at φ=0° and φ=90°
b) At mid-solvent along the horizontal plan z=2 cm
c) Near the interface along the horizontal plan z=1.5 cm

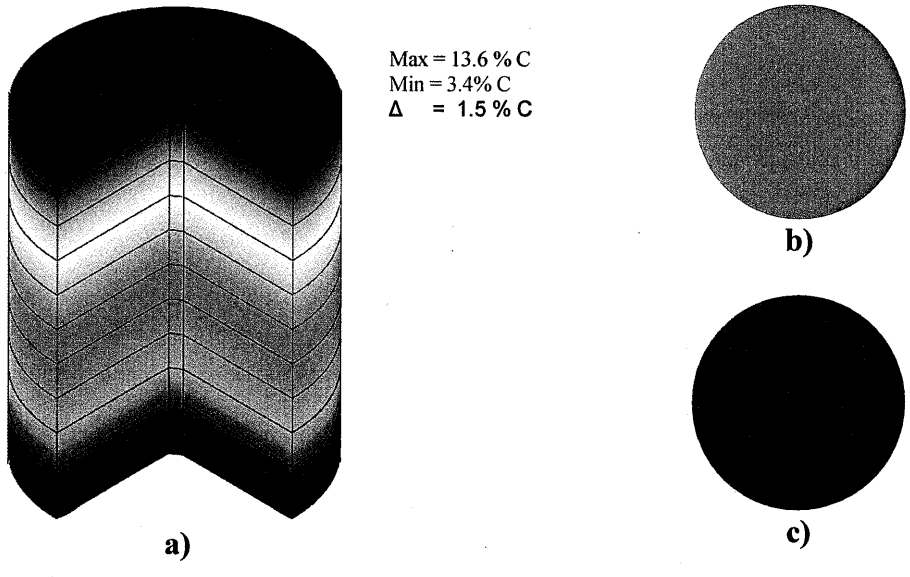

Figure 3- 17: Silicon distribution under static micro-gravity of $10^{-6}g_o$:

a) 3D view of cross section at φ=0° and φ=90°
b) At mid-solvent along the horizontal plan z=2 cm
c) Near the interface along the horizontal plan z=1.5 cm

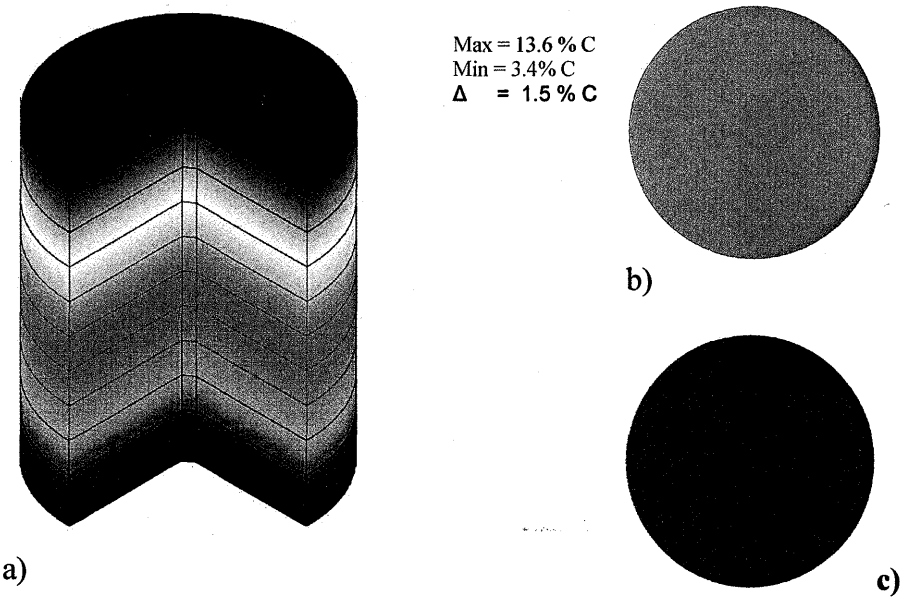

Figure 3- 18: Silicon distribution in the absence of gravity

a) 3D view of cross section at $\varphi=0°$ and $\varphi=90°$
b) At mid-solvent along the horizontal plan z=2 cm
c) Near the interface along the horizontal plan z=1.5 cm

Figures 3-14 to 3-19 capture the behavior of the silicon concentration within the solvent region as the gravitational growth condition is decreased from 1go to 10^{-3} g_o, 10^{-4} g_o, 10^{-6} g_o and $0g_o$, respectively. Part a of these figures show the three-dimensional silicon distribution behavior, While parts b and c show the silicon variation at mid-solvent and near the growth interface, respectively. Examining these figures it is noted that the silicon distribution does not follow the same behavior as that of flow. Figure 3-14 shows that under terrestrial conditions, the silicon distribution exhibit complex behavior. The convective flow in this particular case is the highest in terms of the intensity and the complexity. In return, this complexity is reflected on the radial concentration variation. Comparing Figure 3-14b to Figure 3-14c, significant concentration gradient is noted near the growth interface compare to that at mid-solvent. This is an indication that under terrestrial conditions silicon migration is driven by buoyancy convection to a certain level. As the static micro-gravity is reduced to 10^{-3} g_o, shown in Figure 3-15, the complexity of the silicon distribution reduces becoming more uniform.

The ideal desirable case of crystal growth is in the absence of gravity where the flow is purely diffusive. Therefore, by decreasing the static micro-gravity further to 10^{-4} g_o and 10^{-6} g_o, and zero gravity as demonstrated in Figures 3-16, 3-17 and 3-18, respectively, the silicon migration to the growth interface slows down in the absence of convection allowing silicon particle to slowly diffuse through the melt to the growth interface. As a result, less silicon concentration settles down near the growth interface compare to that at mid-solvent. Consequently pure silicon concentration is obtained along the radial plan near the growth interface and at mid-solvent, as seen in parts b and c of these figures. This comparison can also be verified by examining Figure 3-19.

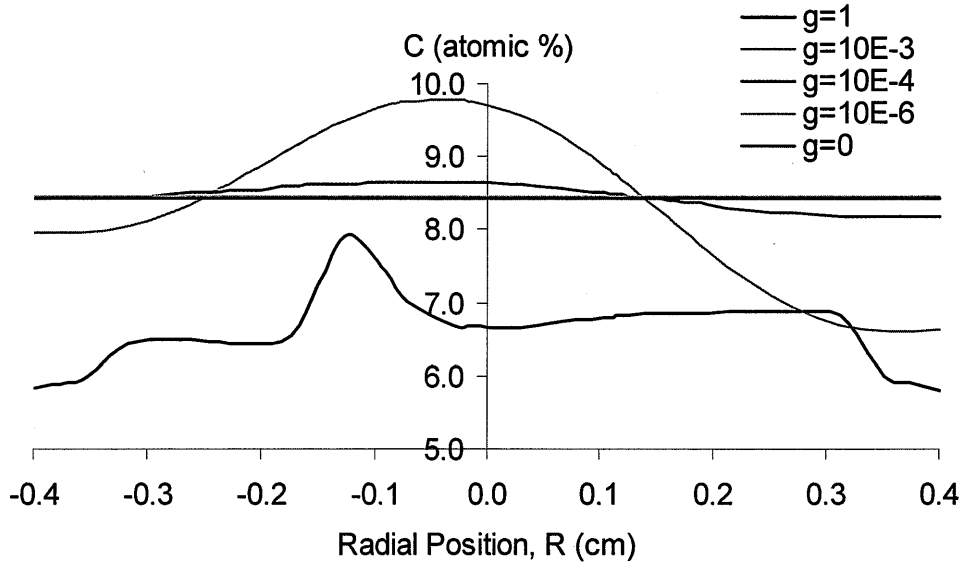

a)

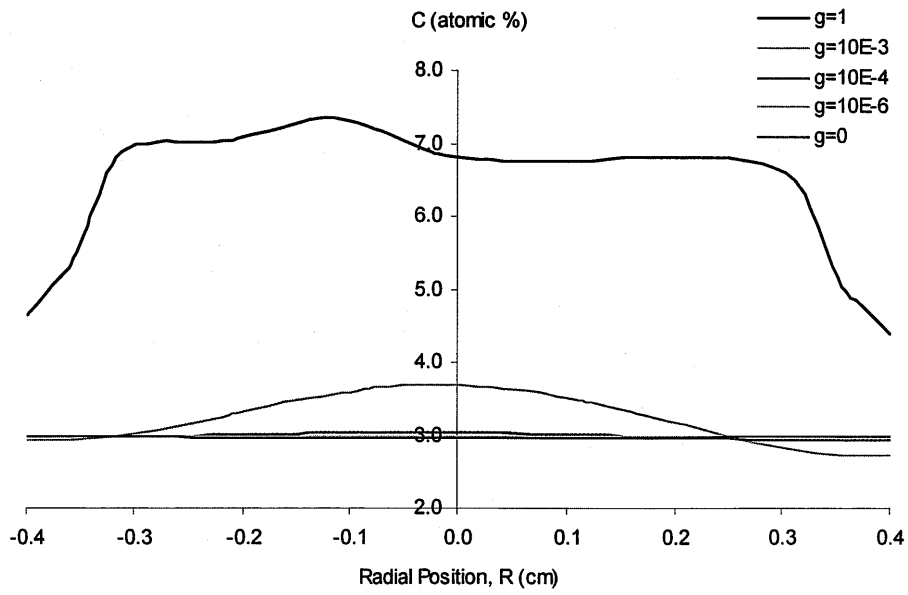

b)

Figure 3- 19: Silicon Distribution along the Radial Direction under various gravitational growth conditions at

a) Mid-solvent, i.e. Z = 2 cm at φ=0°
b) Near the growth interface, i.e. Z = 1.5 cm at φ=0°

Yet, one may ask at what level of static micro-gravity convective flow would be considered to have an effect on the silicon transportation. To answer such question, the silicon concentration at each micro-gravity level has to be examined closely. For crystal growth under gravity conditions of 1go, $10^{-3}g_o$, $10^{-4}g_o$, $10^{-6}g_o$ and $0g_o$, the silicon concentration at the growth interface was found to fluctuate in the range of 7.35 %C to 4.38 %C, 3.69 %C to 2.73 %C, 3.04 %C to 2.93 %C, 2.994 %C to 2.976 %C and 2.987 %C to 2.970 %C, respectively. As can be noted the degree of fluctuation decreases as the micro-gravity level decreases. At a micro-gravity level of $10^{-6}g_o$ the difference in fluctuation is around 0.017 %C, while in the absence of gravity the difference in fluctuation is around 0.016 %C. Therefore, $10^{-6}g_o$ is a level of micro-gravity where the silicon migration can be considered to be the result of pure diffusion. Note, our mesh validation still apply in this comparison since the quality of the mesh is valid for up to 10^{-4} %C as discussed in chapter 2.

Chapter 4

Sinusoidal Micro-gravity Effect

In a typical microgravity environment, the residual acceleration experienced by the spacecraft is composed of a quasi-steady component and many time-dependent components. This chapter will analyze a simplified form of acceleration, which consists of one quasi-steady component and one time-dependent component. The non-dimensional form of this sinusoidal gravity is expressed as follows:

$$g^* = g_1^* + A^* \sin(2\pi F^* \tau) \qquad (4\text{-}1)$$

Where, g^*_1 is the non-dimensional static gravity, A^* is the non-dimensional amplitude and F^* is the non-dimensional frequency.

The main concept is to suppress the intensity of the convective flow as much as possible to obtain pure diffusive transportation of silicon in the growth interface. In order to do so, the factors controlling the intensity of the convective flow have to be examined thoroughly and individually. These factors were identified to be the sinusoidal amplitude effect, A, the frequency effect, F, and the combined static gravity effect.

Initially, this chapter will study the SiGe crystal growth under a synthetic gravity similar to that encountered in space. The effect of static micro-gravity, as part of the synthetic gravity, will also be analyzed to weight its effect compared to that of amplitude and frequency. This case will be followed up by a detailed analysis of the gravitational amplitude and the gravitational frequency effect. Once the effect of each variable is identified, the crystal growth under a realistic space environment will be simulated and studied extensively.

4.1 Study of Realistic Space Sinusoidal Gravity Effect

As a mean to further mimic the space gravitational environment, a single frequency perturbation is studied first of all. In reality, g-jitters aboard space shuttles vary within a wide range of frequencies and amplitudes, in addition to the quasi steady residual gravity. More simulations will be discussed in the following sections to capture the effect of these variables on the crystal growth. An ideal sinusoidal disturbance that can be encountered in the space environment is written in the non-dimensional form as follows:

$$g^* = 10^{-6} + 2\times10^{-3}\sin(\frac{2\pi f \tau D}{u_o}) \quad \text{Where f} = 2.8 \text{ x } 10^{-2} \text{ Hz} \qquad (4\text{-}2)$$

Note, this disturbance is assumed to be perpendicular to the growth interface.

To track the evolution of the flow as a function of time within the solvent regime, four randomly selected nodes will be used for comparison purposes. Figure 4- *1*a demonstrates the physical location of these nodes, while Figure 4- *1*b provides the coordinate location of these nodes.

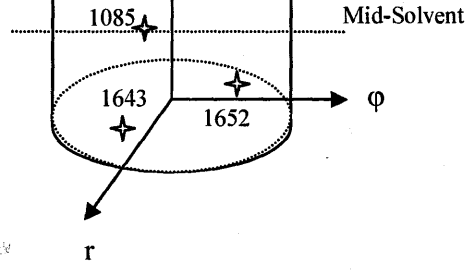

a)

	Coordinate System (cm)		
Node	r	φ	z
1085	-3.94E-01	-6.25E-02	2.00E+00
1652	2.20E-01	1.83E-01	1.60E+00
1643	-1.57E-01	-2.20E-01	1.60E+00
3930	2.20E-01	1.83E-01	2.44E+00

b)

Figure 4- 1: Pre-selected Nodes used for behavioral comparison

a) Physical Locations

b) Coordinate Locations

Since the g-jitter is a function of time, a transient simulation was carried out. As a result, the gravitational fluctuation effect was noted to influence the behavior of the flow and specie variation as it evolves into quasi-steady state. Figure 4- *2* traces the silicon concentration evolution and flow variation at different locations of the solvent. This figure indicates that quasi-steady state is obtained at approximately 177 seconds at every node. This is an indication that viscous, thermal and diffusive resonance are reached throughout the solvent region after 177 seconds to effect on the specie oscillation. Node 1085 is located in the dead zone of the flow cell. Therefore, the silicon concentration evolves slowly at this location. Silicon Particles are carried out with high concentration along the rims of the two cells to obtain quick and high concentration of Silicon at nodes 1643 and 1652. However, more silicon concentration is obtained at node 3930 because this node is closest to the source. Zooming closer to silicon concentration pattern and the flow pattern at around 300 to 400 seconds, the flow periodic oscillation was found to be 37.5 seconds, which is the same as that specified by the frequency of the g-jitter. This periodic oscillation of the flow is confirmed to be the same as the silicon concentration oscillation at all locations with a lagging phase difference of around 9 seconds. There is no phase difference between the period imposed by the frequency and the period of the flow oscillation because the sample of the crystal growth is too small to notice a lagging phase difference as would happen in a larger reservoir. It is also worth noting that the flow intensity at node 1643 is half that at node 1652 even thought they are on the same plan above the growth interface, i.e. Z =1.5 cm, yet the silicon concentration evolution is almost identical at the two locations. This is an indication that the flow intensity at these locations does not contribute to the silicon build up regardless of the complexity of the flow. The maximum flow intensity was found to be in the range of 10^{-3} cm/s.

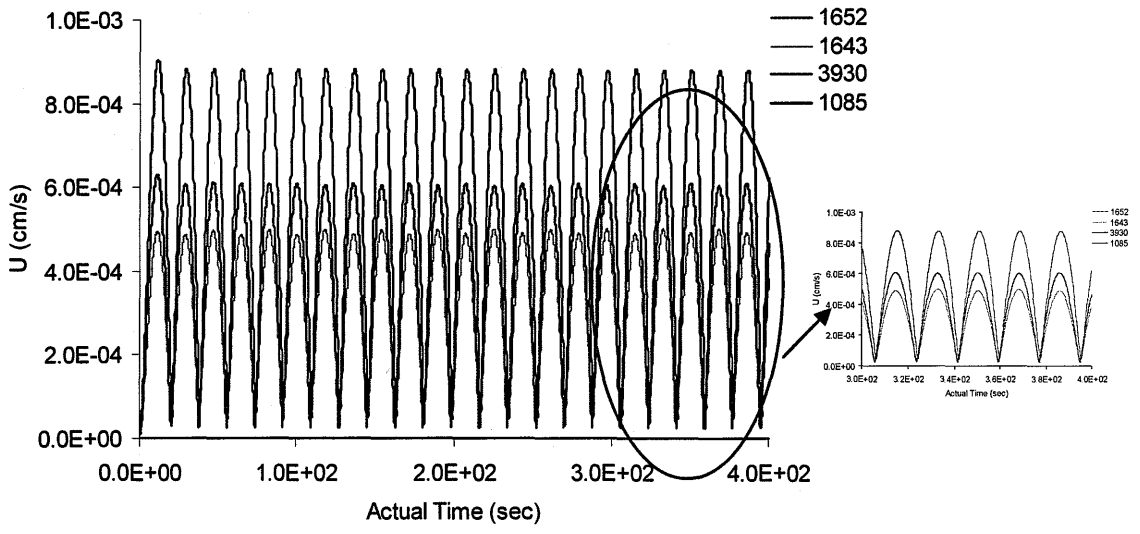

a)

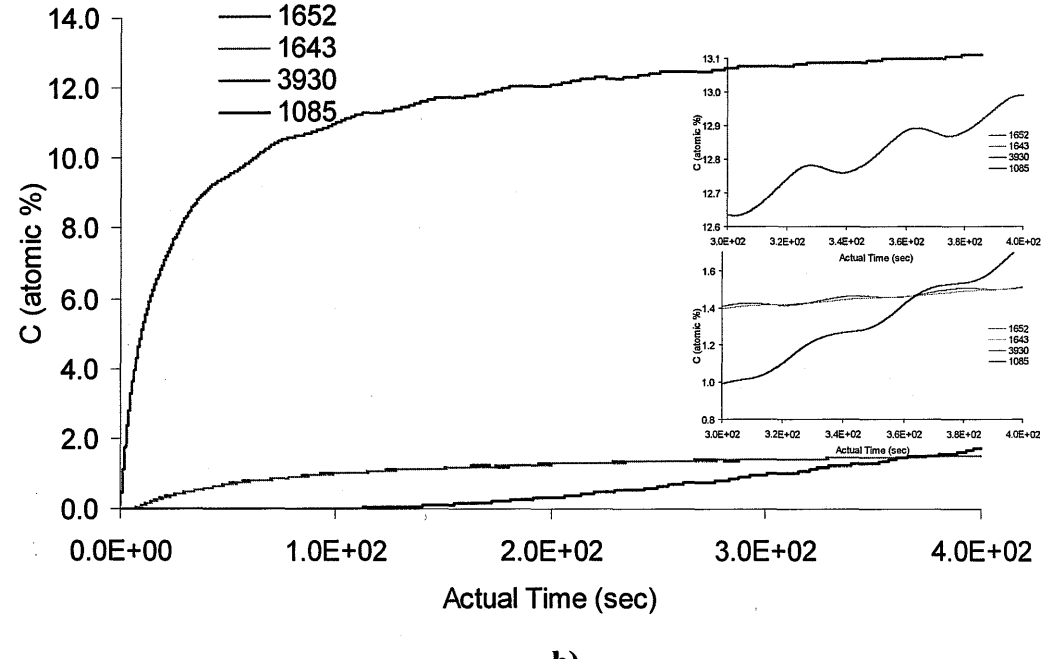

b)

Figure 4- 2: Transient behavior at Various Nodes under an ideal sinusoidal gravity in terms of:

a) The Flow Behavior

b) The Silicon Distribution

Figure 4- *3* indicates that the diffusive flow consists of two cells oscillating in one direction then reversing its rotating direction with the same periodic oscillation, found previously, of 35.7 seconds.

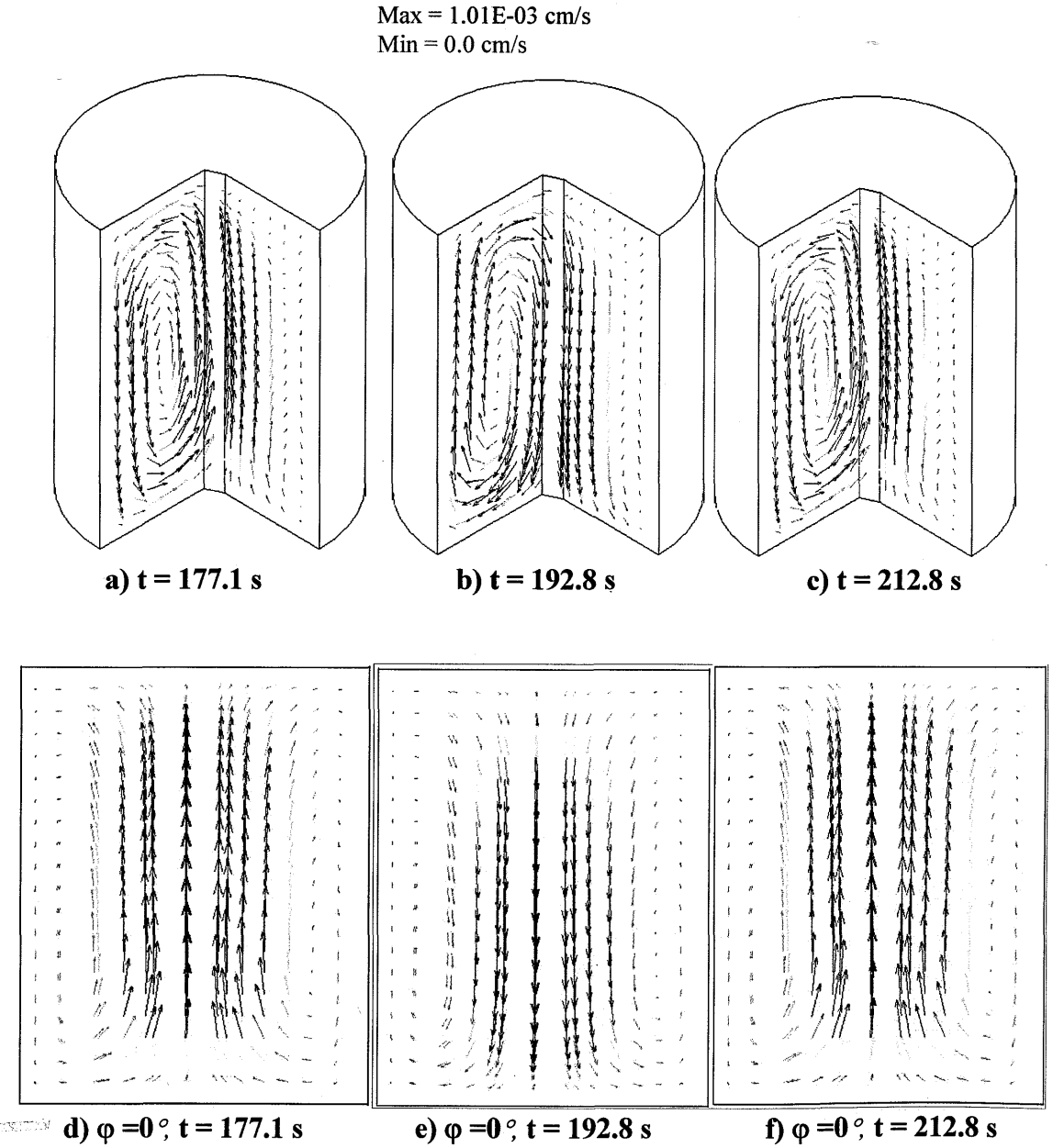

Figure 4- 3: Transient Flow Pattern under Realistic Sinusoidal Gravity in space:

To a certain degree, the species concentration also illustrate similar behavioral pattern, as seen in Figure 4- *4*, 4-5 and 4-6. Once quasi-steady state of specie variation is achieved, very weak fluctuations of silicon variation appear gradually as the silicon concentration propagates down toward the growth interface. Again the periodic behavior of the silicon fluctuation is the same as the imposed body force of g-jitter. Since the silicon particles are force to follow the flow of the cells formed within the solvent regime, the periodic behavior of the flow is inherited by the silicon migration to the growth interface.

Figure *4- 4* clearly illustrates this behavior.

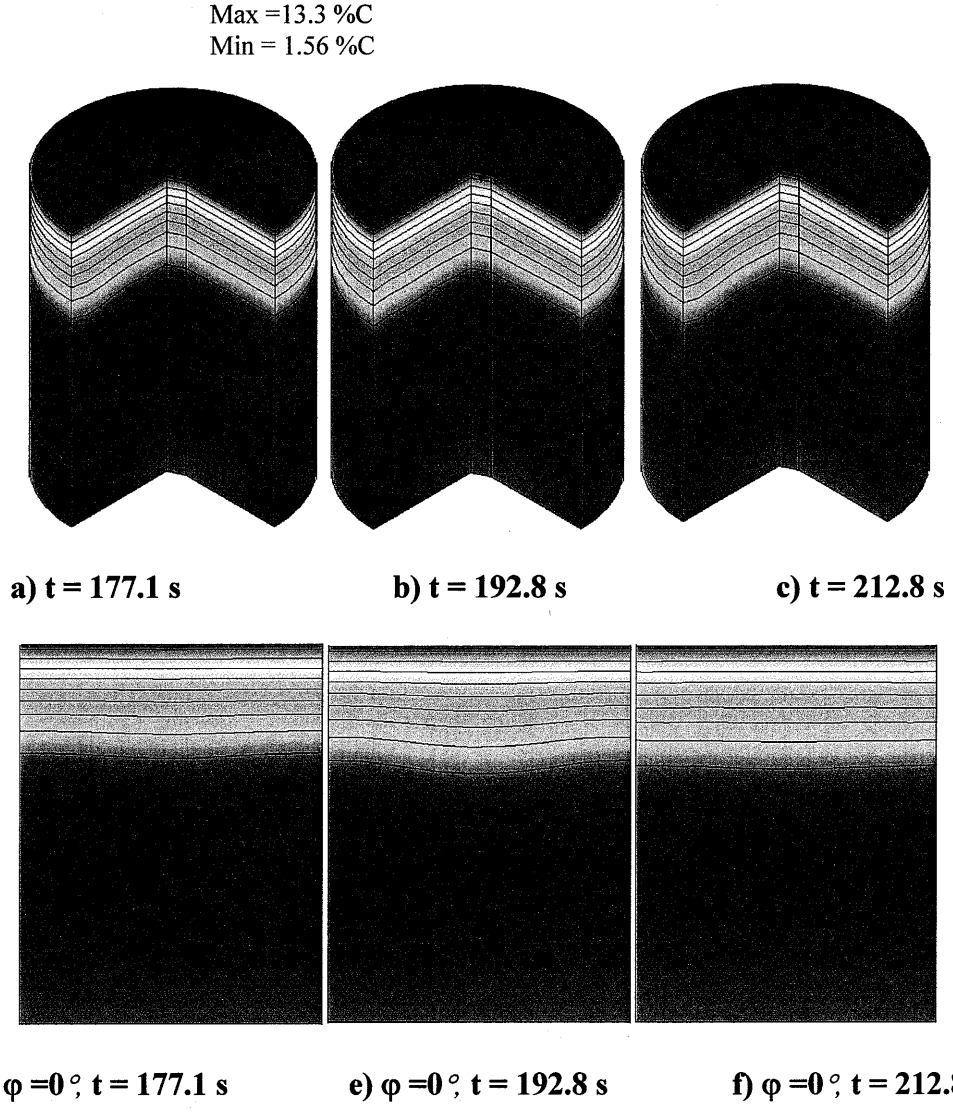

Figure 4- 4: Transient Silicon Migration under a realistic Sinusoidal Gravity in Space

Figure 4-5 illustrates the evolution of the flow behavior near the growth interface. This Figure indicates that under ideal sinusoidal gravity affect the complexity of the 3D flow increases compared to the previous static micro-gravity case of $10^{-6}g_o$, which was discussed in Chapter 3. The flow build up on left side would be expected to have a measurable effect on the silicon distribution as well, provided that its intensity is within convective flow range.

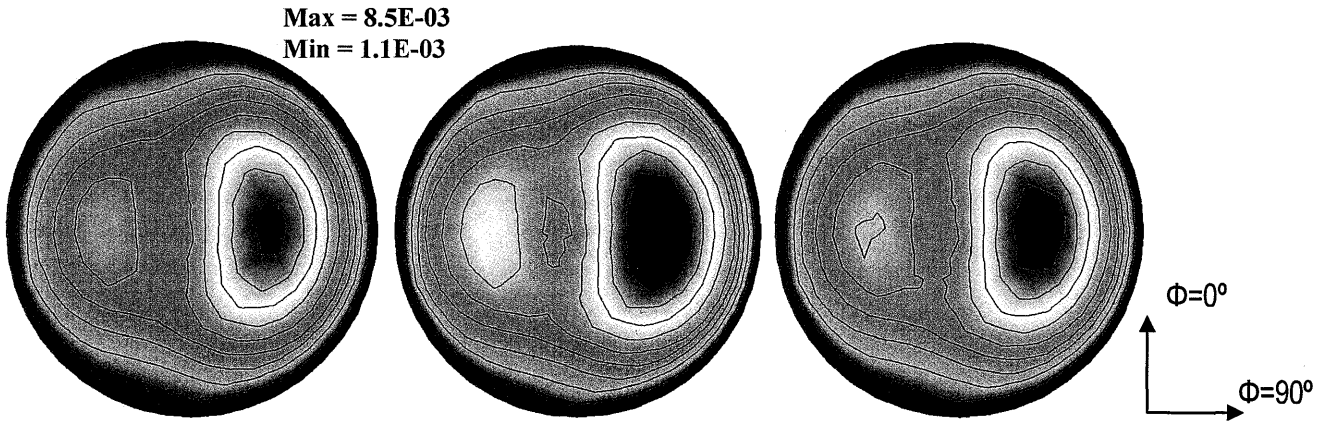

a) t = 177.1 s **b) t = 192.8 s** **c) t = 212.8 s**

Figure 4-5: Transient Flow Behavior under a realistic Sinusoidal Gravity in Space near the growth interface along the horizontal plan z=1.5 cm

In chapter 3, based on static gravity analysis, we concluded that the intensity of the complex 3D flow is positively proportional to the intensity of the gravitational growth conditions. Under ideal sinusoidal gravitational growth condition, the static gravity was set to 10^{-6} g_o while the amplitude of the synthetic gravity was set to 10^{-3} g_o. According to these results, the obtained flow intensity is positively proportional to the dominating gravitational variable, which is the amplitude of the synthetic gravity in this case. To confirm this conclusion, further tests on the effect of static gravity are compared to that of the amplitude and will be discussed in section 4.2.

The combination of the thermal solute effect and the buoyancy effect, imposed by the synthetic gravity effect, reflect on the crystal growth near the growth interface, as seen in Figure 4-6. Surprisingly it was found that the complexity of the flow, especially along the axial direction at $\varphi = 90°$, contributes to the mixing of the solvent leading to a more uniform distribution of silicon compare to the results obtained under static gravity of $1g_o$ and 10^{-3} g_o, as seen through out chapter 3 compare to the results seen in Figure 4- *6*. This is possible because the flow is more in a diffusive mode than it is convective under sinusoidal g-jitter. This statement apply regardless of the previously noted flow build up along on the $\varphi=90°$ direction near the growth interface.

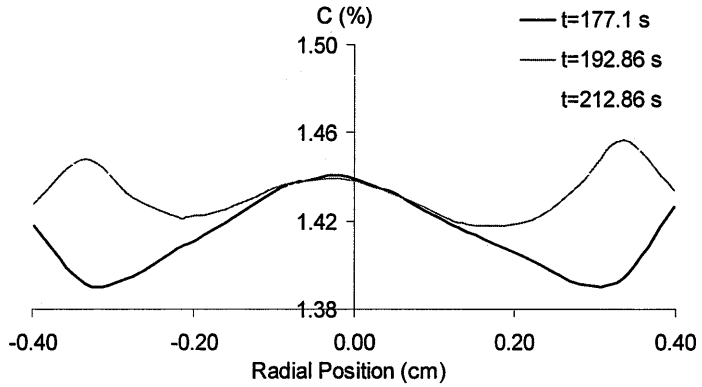

a) $\varphi = 0°$

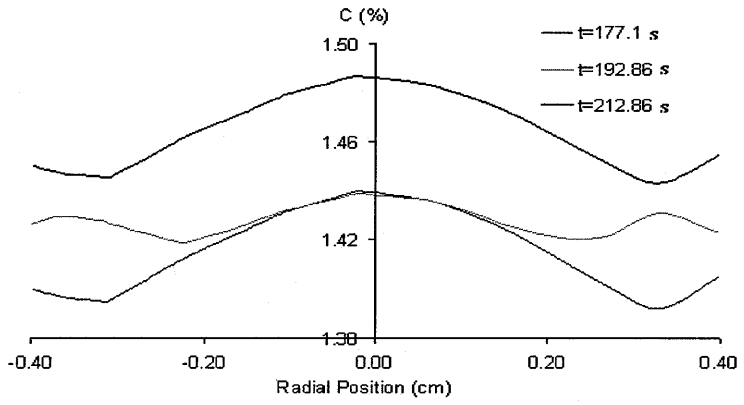

b) $\varphi = 90°$

Figure 4- 6: Transient Silicon distribution Near the Growth Interface at Z =1.5 cm under sinusoidal gravity effect in space

Figure 4- *6* shows a symmetrical silicon distribution near the growth interface. The silicon concentration along the radial direction at both $\varphi=0^{\circ}$ and $\varphi=90^{\circ}$ demonstrate similar fluctuating behavior, which indicate the absence of 3-D silicon concentration complexity. By comparison, the quality of symmetry obtained under the influence of sinusoidal g-jitter is more uniform than that obtained under static gravity only, as captured and discussed in chapter 3. Furthermore, the silicon concentration under static microgravity is higher because more time is allowed for the solution to reach steady state compare to the time allowed for the transient sinusoidal simulation to reach quasi-steady state. Therefore, under static microgravity only, more silicon particles would build up near the growth interface compare to crystal growth under sinusoidal gravity, where transient silicon migration is being traced. Nevertheless, the transient pattern we obtained for the transient simulation under sinusoidal growth condition provides us with a better understanding of the silicon behavior within the solvent regime. Under static gravity, the direction of the flow at the center of the solvent is always upward. Since the silicon transportation is dependent on the flow variation, an opposing flow stream, such as that encountered under sinusoidal g-jitter, would slow the migration of silicon to the growth interface leading to a lower silicon concentration distribution at the interface. This phenomenon leads to slower crystal growth. Yet, it is appreciable because it offers better silicon distribution along the growth interface, which indicates high quality crystal growth, as desired.

4.2 Static Residual Gravity Effect

One would expect the static residual gravity to have a decent effect on the flow behavior since microgravity cases, examined in chapter 3, have shown complex 3D flow. Therefore, the static gravity component is eliminated from the realistic space sinusoidal gravity case, examined above to obtain a single Fourier component.

$$g^* = 3x10^{-3} \sin(\frac{2\pi f \tau D}{u_o}) \text{ Where f} = 2.8 \text{ x } 10^{-2} \text{ Hz} \qquad (4\text{-}3)$$

Since the flow behavior has a direct influence on the silicon build up near the interface, the silicon concentration evolution is analyzed extensively then compared to the results obtained under the assumed realistic sinusoidal g-jitter. The main objective is to capture the static residual gravity effect compare to the Fourier component of the g-jitter.

Figure 4- *7* indicates that under pure sinusoidal g-jitter, without static gravity, the evolution of silicon concentration near the growth interface is identical to that under the same sinusoidal g-jitter with the addition of static gravity, except along the radial direction at φ=90°. As discussed in the previous section, the silicon transportation is dependent on the flow variation pattern. In the absence of static gravity, the migration of silicon to the growth interface at mid-solvent zone would be, relatively, faster. At mid-solvent, the two flow cells merge to travel upward against silicon migration direction creating an opposing gravitational force. The strength of this force would be less under sinusoidal gravity growth condition compare to growth condition, where both sinusoidal and static gravity are present. This is particularly true along the radial direction at φ=90°, where the flow is more complex in nature. As a result, the species concentration is elevated at the middle of the growth interface relative to the case with the combined effect of static and sinusoidal gravity. Nevertheless, this elevation is very small that it could be ignored.

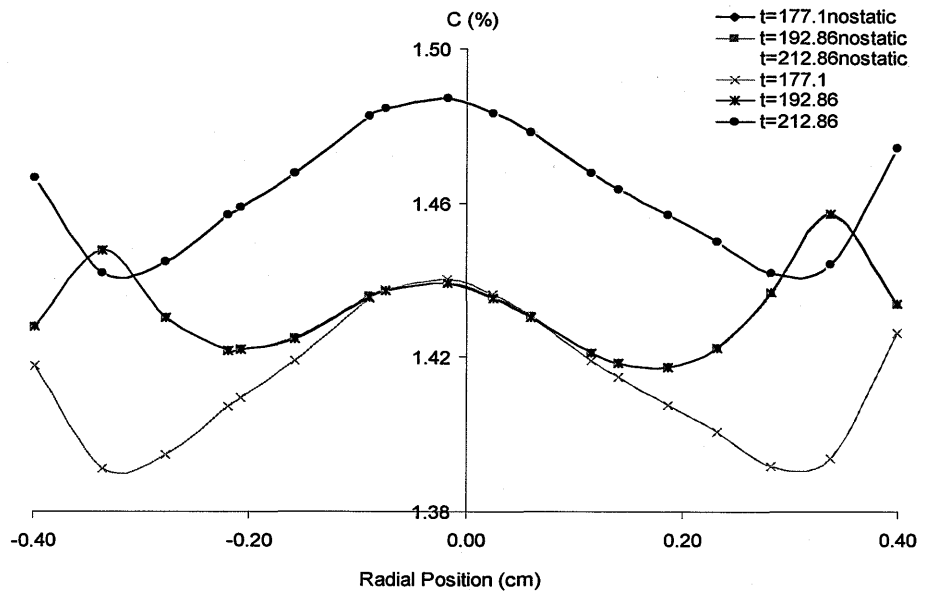

a) $\varphi = 0^o$

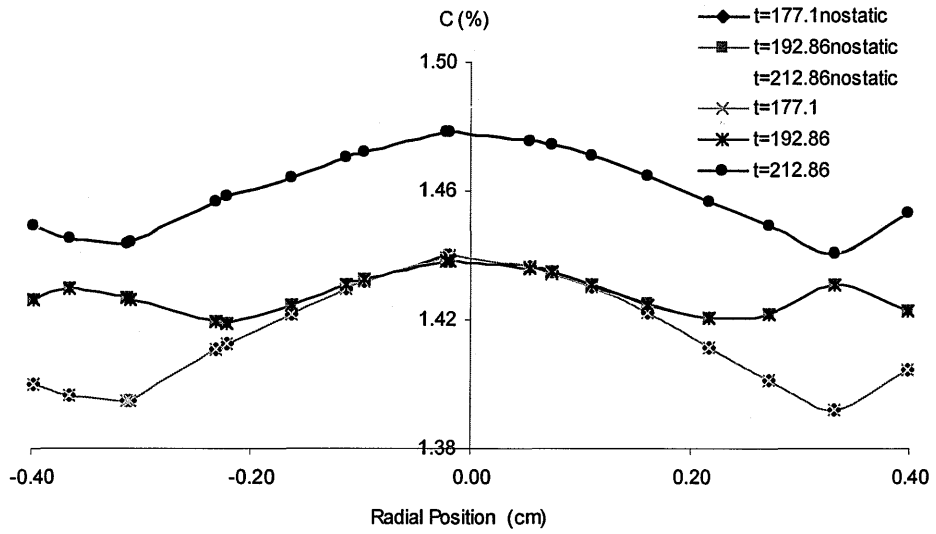

b) $\varphi = 90^o$

Figure 4- 7: Silicon Concentration Distribution Near the growth Interface under realistic sinusoidal g-jitter with static/no-static gravity components effect along the radial direction

The fact that under static gravity of 10^{-6} g_o, the flow is diffusive in nature in the range of 10^{-6}cm/s, which can be considered very weak, as shown previously. Under realistic sinusoidal g-jitter, the flow intensity was found to be in the range of 10^{-3} cm/s. Therefore, the addition of flow intensity of 10^{-6} cm/s, caused by the additional static microgravity, will not have a noticeable effect on the flow behavior, as shown in

Figure *4- 8*. Consequently, it will not have noticeable effect on the silicon transportation. Therefore, the flow is still in diffusion mode and it can be concluded that sinusoidal g-jitter does not disturb the nature of the flow within the solvent regime regardless of whether it contain a static component or not.

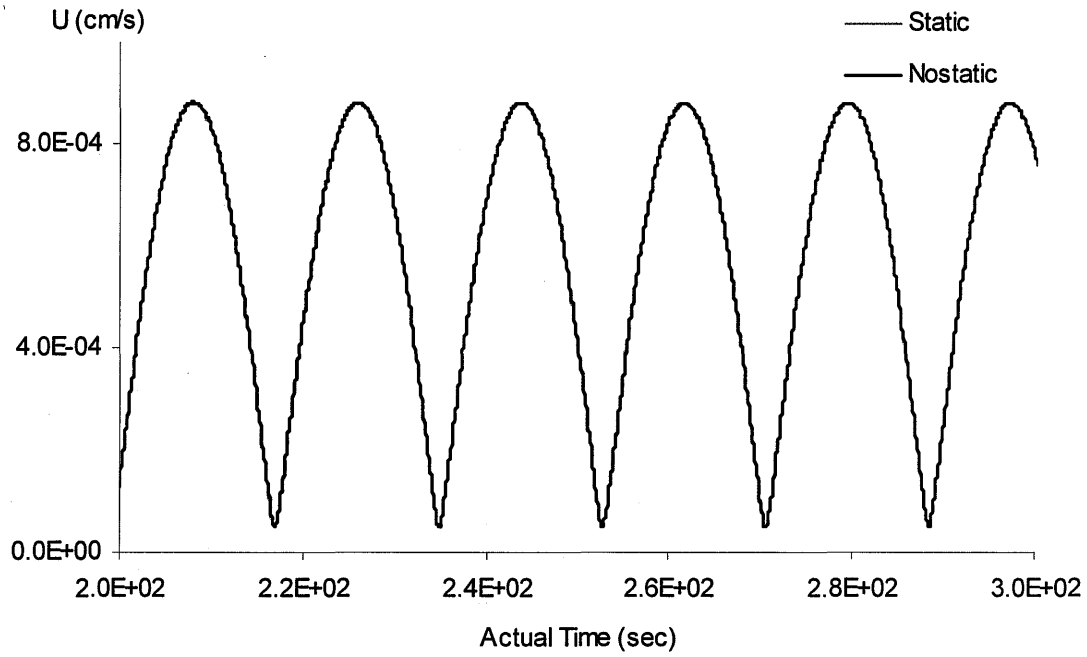

Figure 4- 8: The Transient Flow Distribution at node 1652 under realistic sinusoidal g-jitter with static gravity components and with no-static gravity effect

4.3 Amplitude Effect

The static gravity was determined to have the least effect on the silicon distribution. Therefore, the next step is to examine the effect of varying the amplitude in the sinusoidal g-jitter. Starting with the assumed realistic sinusoidal gravity specified above, the amplitude decreased to match that of the FOTTON 11 collected data. The main equation representing the sinusoidal gravity was set as:

$$g^* = 10^{-6} + A^* \sin(\frac{2\pi f \tau D}{u_o}) \qquad (4\text{-}4)$$

During this analysis, the frequency was kept constant at 2.8 x 10^{-2} Hz, while the amplitude was decreased gradually from 2 x 10^{-3} g_o to 2 x 10^{-4} g_o, 2 x 10^{-5} g_o, and 2 x 10^{-6} g_o. Initially, a thorough study of the flow intensity due to different g-jitter amplitudes was conducted. Part a of Figure 4- *9* to 4-12 capture the transient behavior at various locations within the solvent region simultaneously for each case. Based on the flow behavior captured at nodes 3930, 1652 and 1643, quasi-steady state is reached at the same time in every case to be at 177 seconds. Therefore, one can assume that silicon propagation rate toward the growth interface is not influenced by the amplitude variation of g-jitter. However, zooming into the quasi-steady state as shown in part b of Figure 4- *9* to 4-12, the average silicon concentration is higher under high g-jitter amplitude. Equivalently, the maximum flow intensity is positively proportional to the intensity of the g-jitter amplitude. Yet, comparing the effect of the amplitude intensity on both flow fluctuation and silicon concentration, both these variables are noted to experience a sudden decrease as the g-jitter amplitude is decreased from 2 x 10^{-3} g_o to 2 x 10^{-4} g_o. This is more noticeable at both nodes 1652 and 1643 where the quasi-steady state of the silicon concentration is decreased by 0.2 %C. This increase is still relatively small; therefore, it can be ignored.

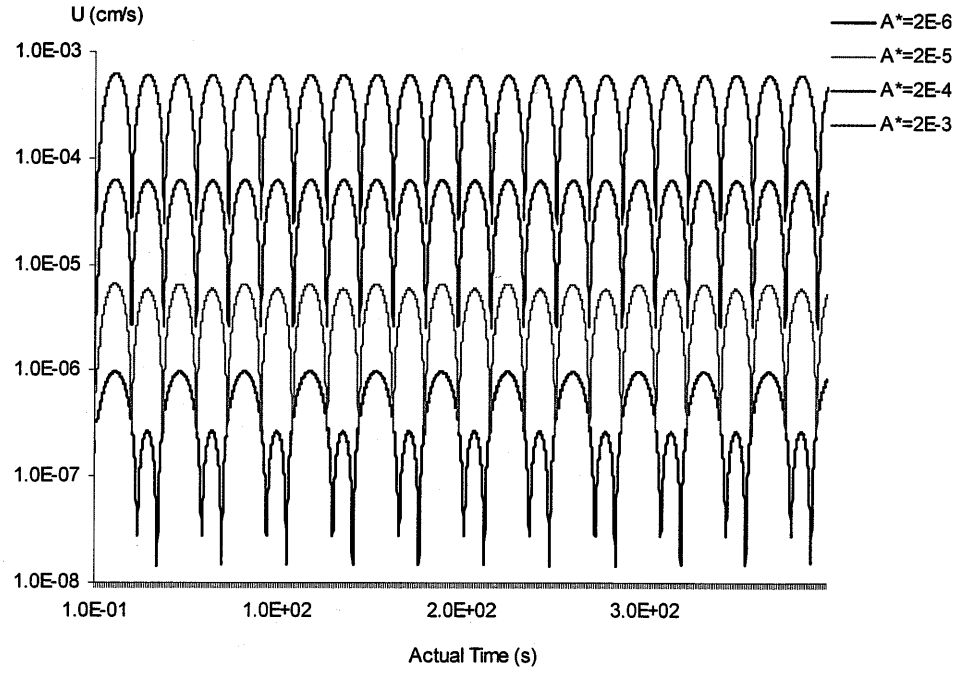

a)

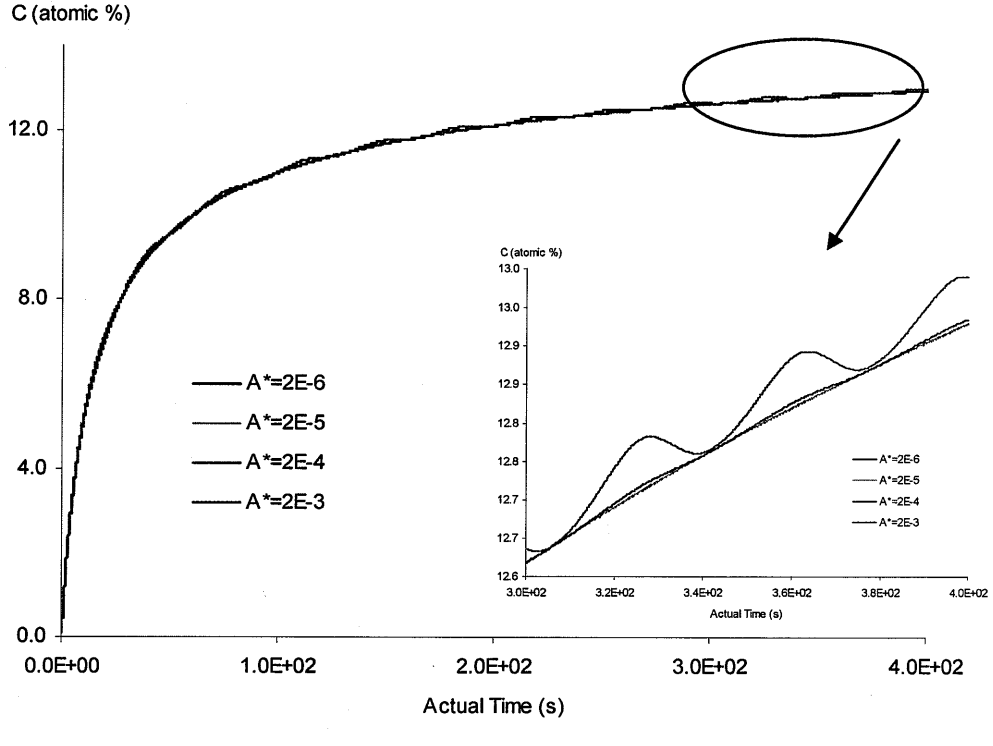

b)

Figure 4- 9: Transient behavior at node 3930 within the solvent regime under various sinusoidal amplitudes in terms of:

a) Flow behavior
b) Silicon Evolution

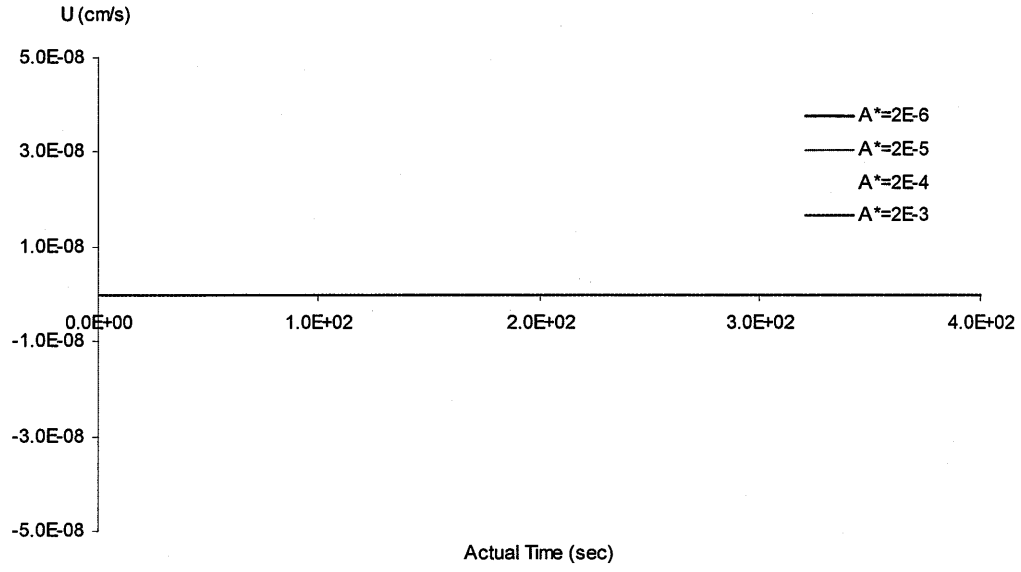

a)

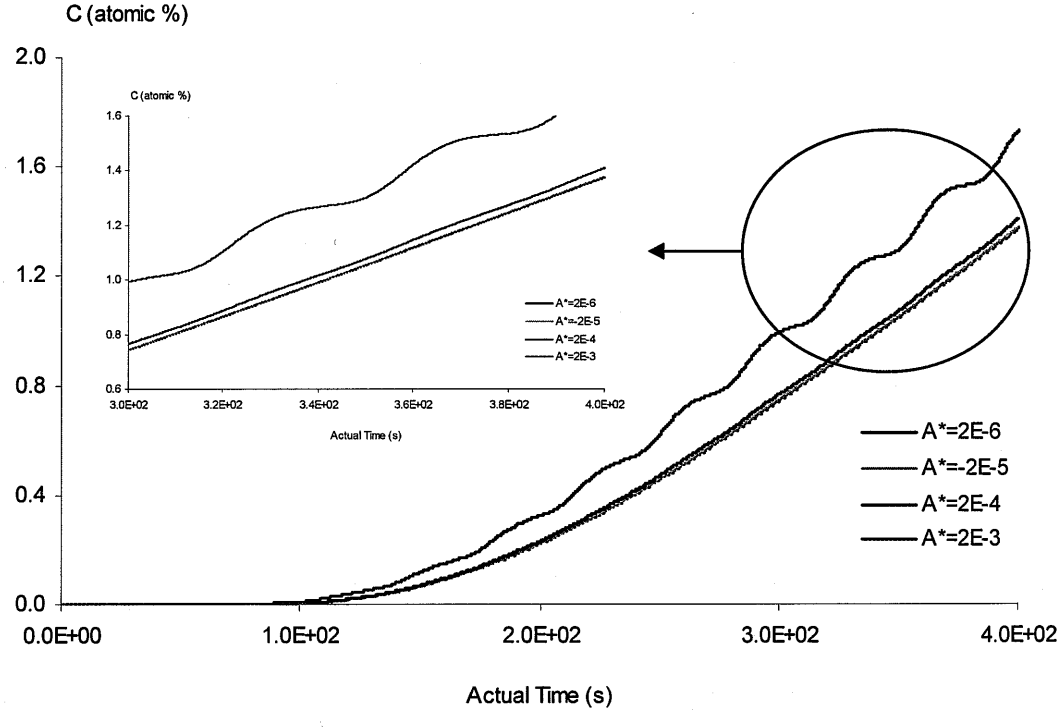

b)

Figure 4- 10: Transient behavior at node 1085 within the solvent regime under various sinusoidal amplitudes in terms of:

a) Flow behavior
b) Silicon Evolution

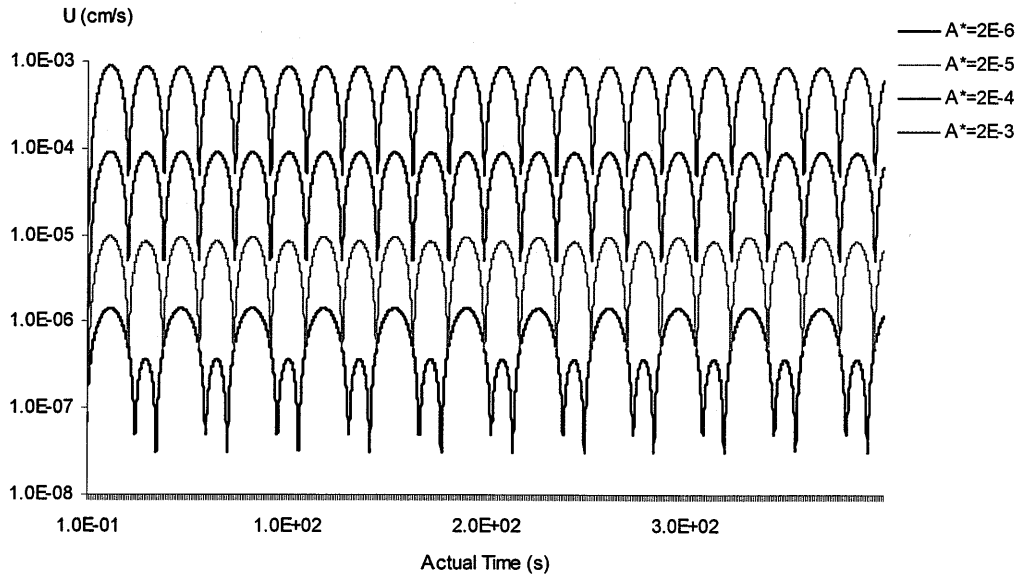

a)

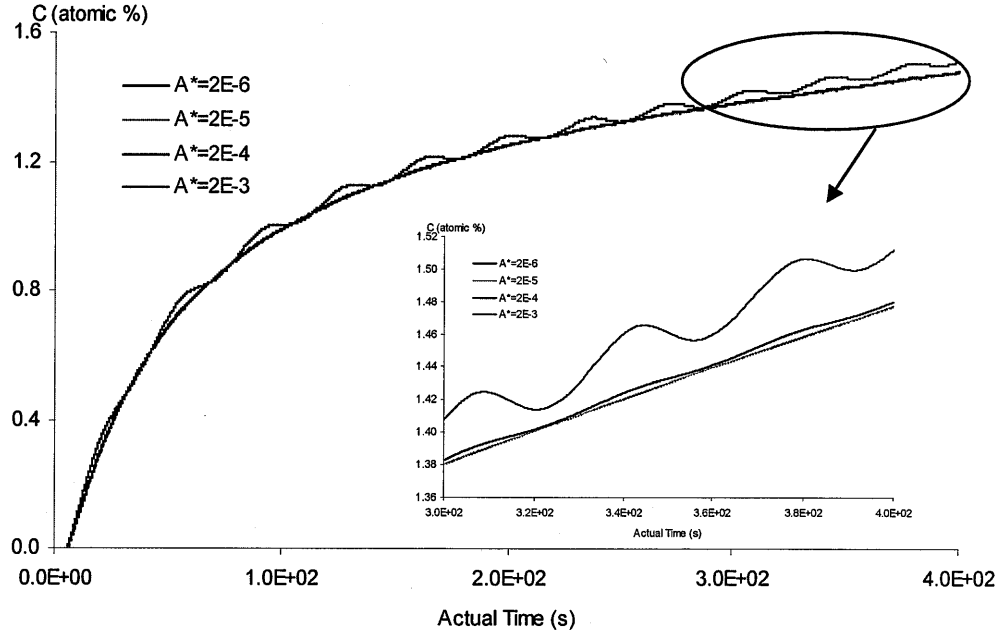

b)

Figure 4- 11: Transient behavior at node 1652 within the solvent regime under various sinusoidal amplitudes in terms of:

a) Flow behavior
b) Silicon Evolution

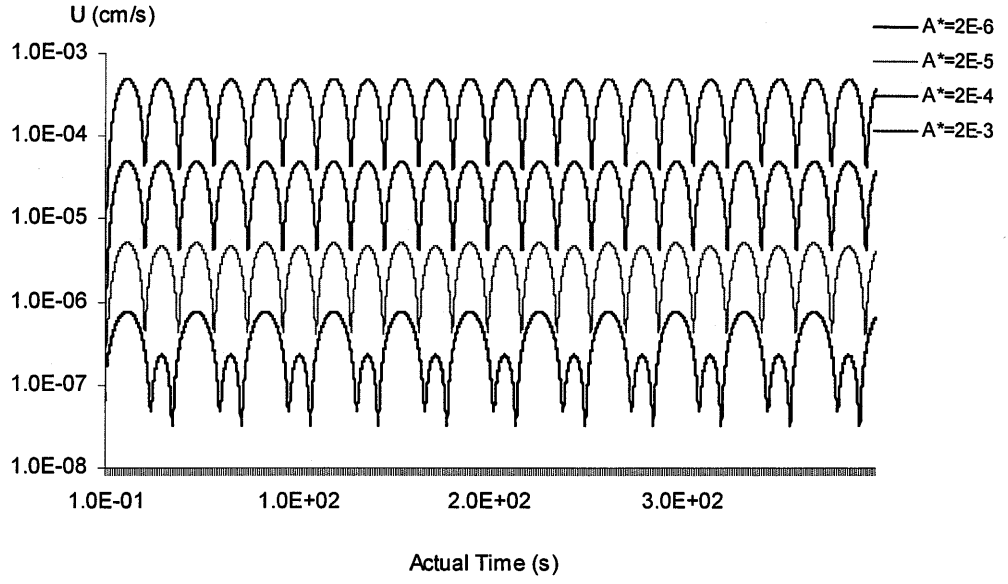

a)

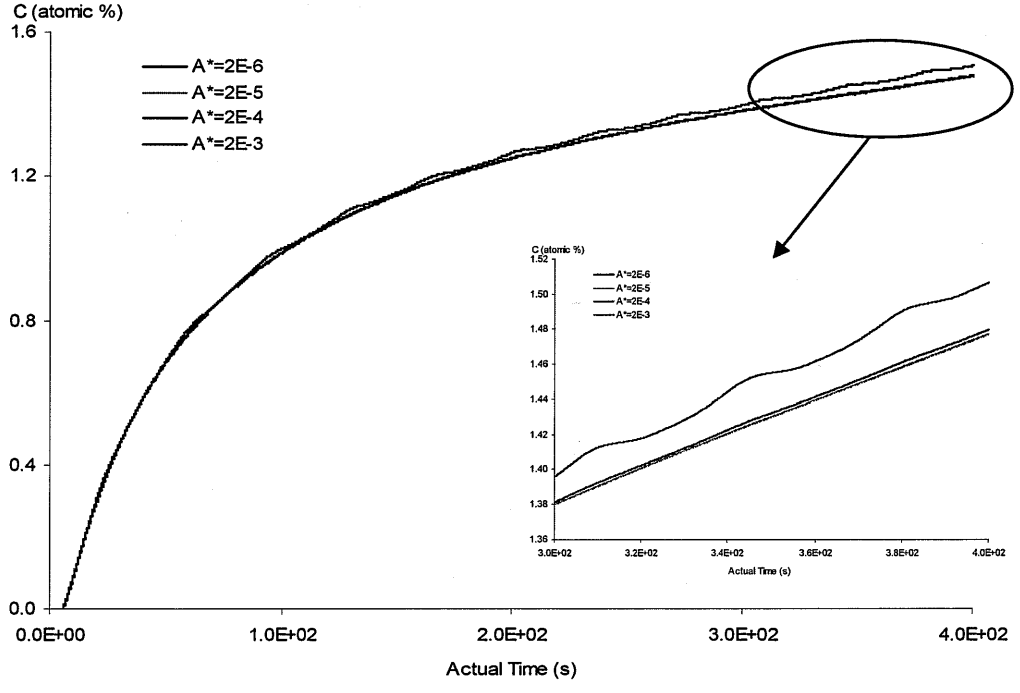

b)

Figure 4- 12: Transient behavior at node 1643 within the solvent regime under various sinusoidal amplitudes in terms of:

a) Flow behavior
b) Silicon Evolution

The decrease of silicon distribution as the amplitude is decreased from 2 x 10^{-3} g_o to 2 x 10^{-4} g_o indicates that amplitude variation of g-jitter has an effect on the diffusion of silicon. The fluctuation of the flow, seen in parts a of Figure 4- *9* to 4-12, becomes more noticeable as well as the amplitude is increased. Note: the g-jitter amplitude variation has an influence on the intensity of the flow, which has a proportional influence on the intensity of the silicon concentration at the various locations. Therefore, comparing the flow intensities at nodes 1652 and 1643, it is noted that flow still indicate the existence of complex 3D flow, which in return reflect proportionally on the intensity and complexity of the silicon concentration variation. Yet, under no circumstances it has an influence on the fluctuation period, which was noted to be constant at 37.5 seconds at every node.

This behavior is further captured in Figure 4- *13* to 4-16. Therefore, the silicon concentration oscillation will always be lagging with a phase difference of around 9 seconds. Based on this analysis it can be concluded that the g-jitter amplitude variation has an influence on the intensity of the flow, which in return affect the intensity of the silicon diffusion. As a result, faster crystal growth is attained as more build up of silicon concentration is achieved. Yet, amplitude variation does not have an effect on the nature of the flow because it is still within diffusive flow range compared to terrestrial crystal growth condition.

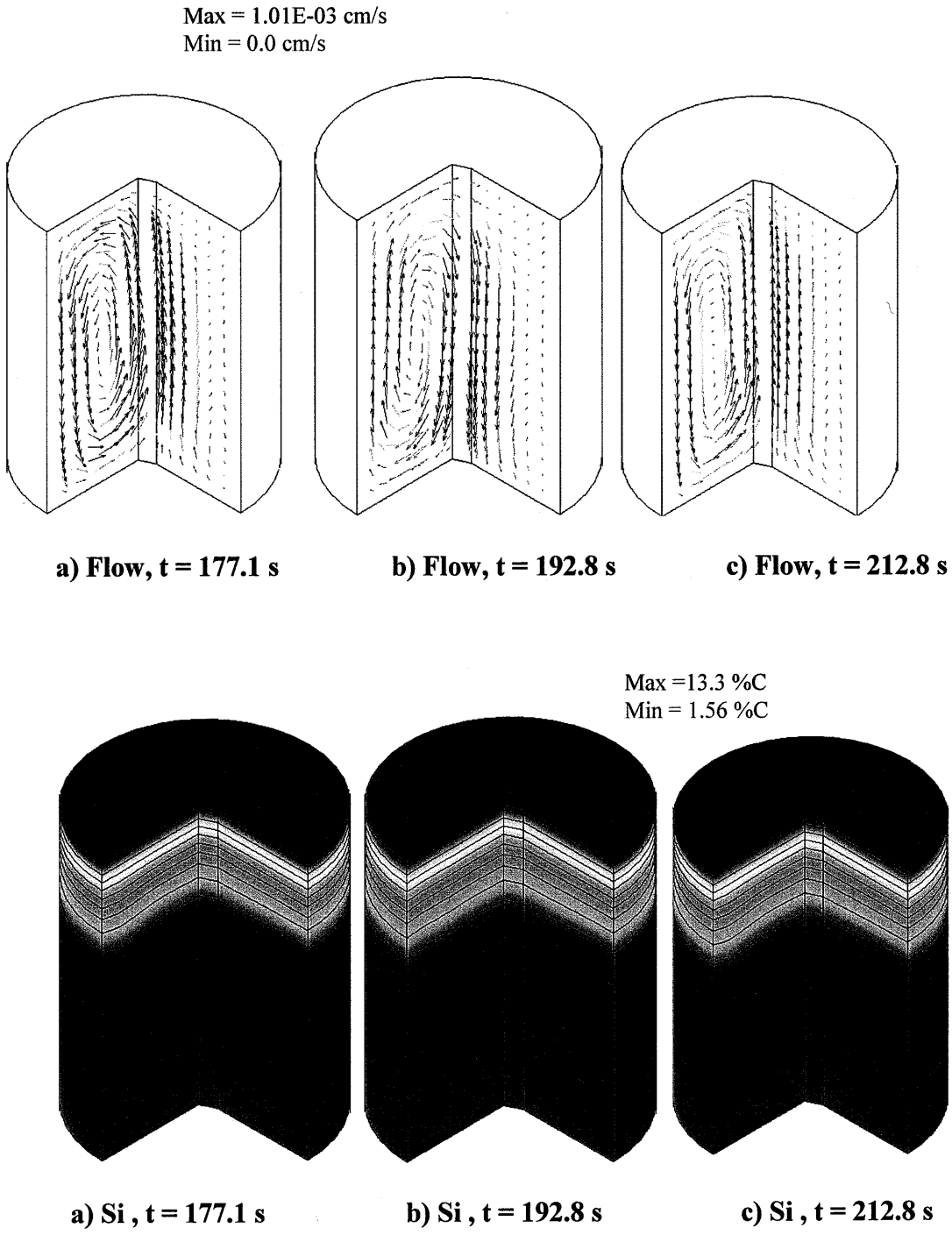

Figure 4- 13: 3D View of the Transient Pattern of Crystal solution under synthetic g-jitter with amplitude of 3x 10^{-3} g_o terms of Flow behavior and Silicon Concentration

Max = 1.01E-04 cm/s
Min = 0.0 cm/s

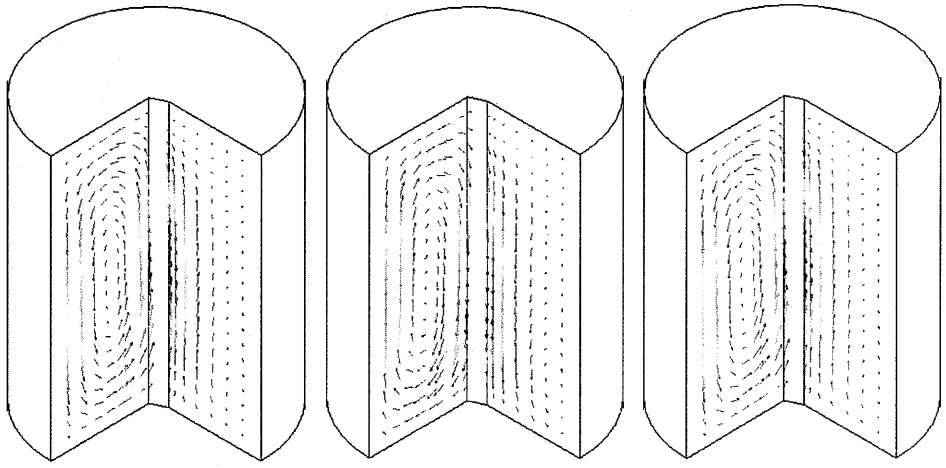

a) Flow, t = 177.1 s **b) Flow, t = 192.8 s** **c) Flow, t = 212.8 s**

Max = 13.3 %C
Min = 1.65 %C

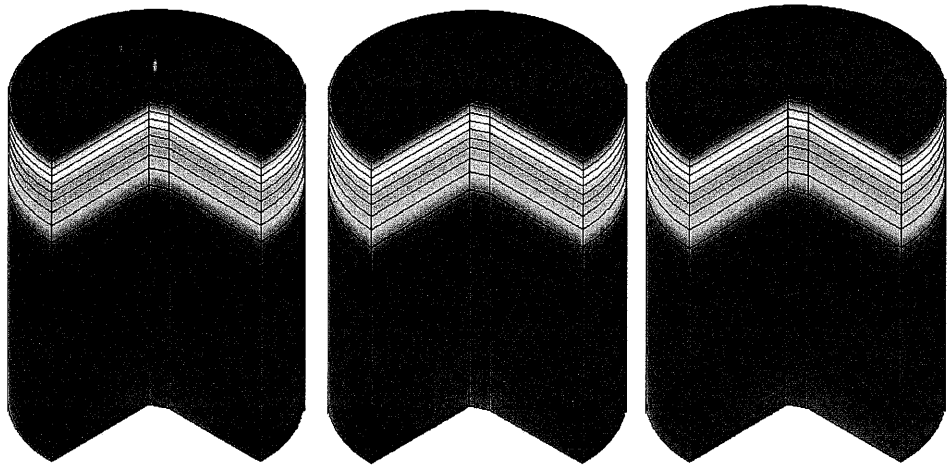

a) Si, t = 177.1 s **b) Si, t = 192.8 s** **c) Si, t = 212.8 s**

Figure 4- 14: 3D View of the Transient Pattern of Crystal solution under synthetic g-jitter with amplitude of 3x 10^{-4} g_o terms of Flow behavior and Silicon Concentration

Max = 1.09E-05 cm/s
Min = 0.0 cm/s

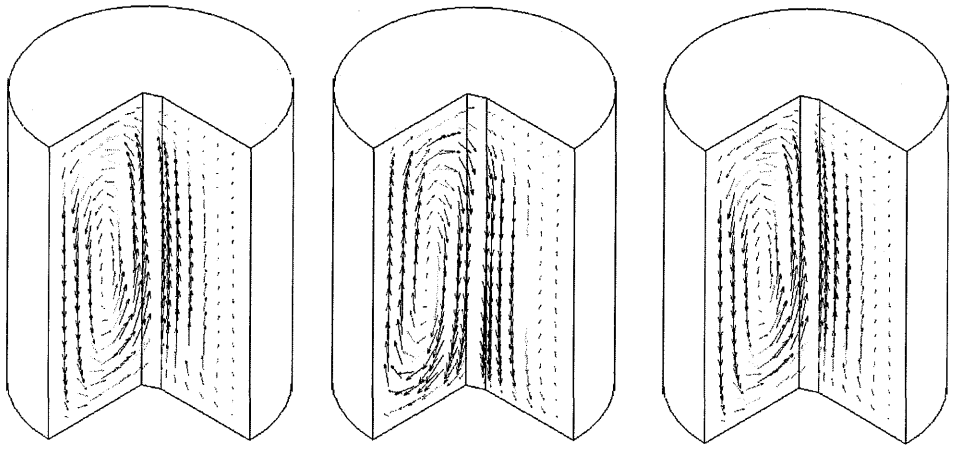

a) Flow, t = 177.1 s **b) Flow, t = 192.8 s** **c) Flow, t = 212.8 s**

Max = 13.3 %C
Min = 1.65 %C

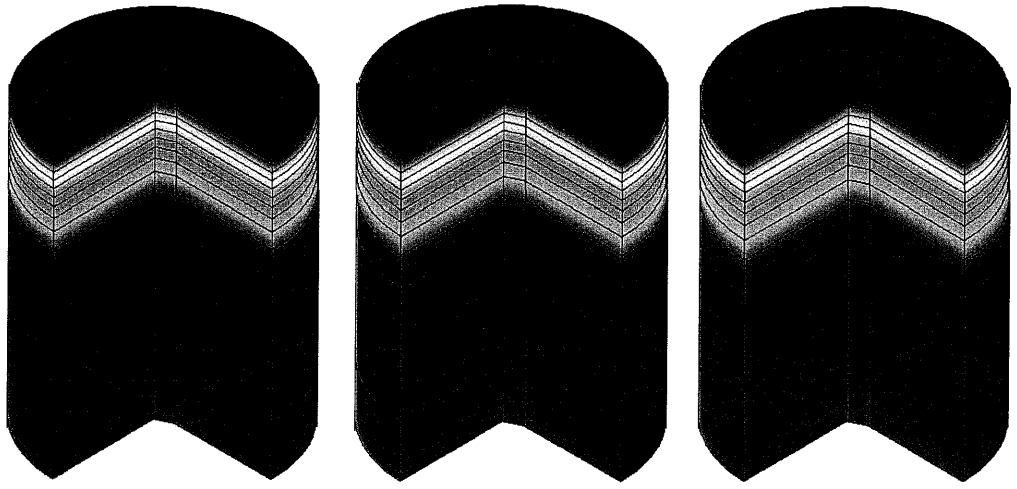

a) Si, t = 177.1 s **b) Si, t = 192.8 s** **c) Si, t = 212.8 s**

Figure 4- 15: 3D View of the Transient Pattern of Crystal solution under synthetic g-jitter with amplitude of 3x 10^{-5} g_o terms of Flow behavior and Silicon Concentration

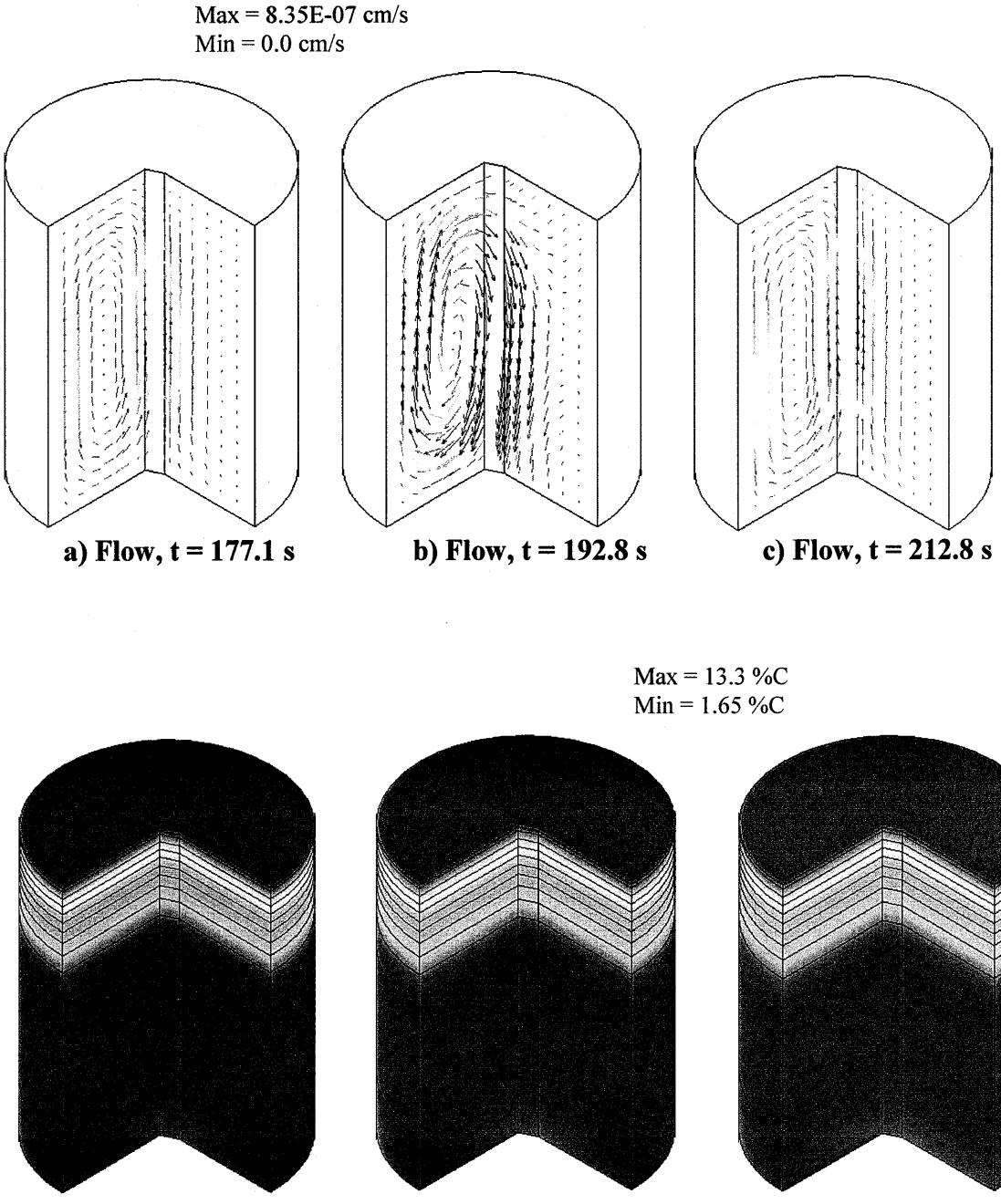

Figure 4- 16: 3D View of the Transient Pattern of Crystal solution under synthetic g-jitter with amplitude of 3×10^{-6} g_o terms of Flow behavior and Silicon Concentration

Figure 4- *17* captures the silicon concentration along the growth interface under the synthetic sinusoidal gravity with the various amplitudes. According to this figure, the silicon concentration decrease, as the amplitude of the synthetic g-jitter is decrease. This figure also demonstrates how the silicon distributions along the growth interface flatten out, as the amplitude is decreased. By examining the average silicon concentration along the growth interface captured in Figure 4- *17*, under the synthetic g-jitter amplitudes of $2x10^{-3}g_o$ to $2\ x10^{-4}g_o$, $2\ x10^{-5}g_o$, and $2\ x10^{-6}g_o$ the average silicon concentration was found to be 1.41 %C, 1.39 %C, 1.39 %C, and 1.39 %C respectively. These data confirms that a drop of g-jitter amplitude from $2\ x10^{-3}g_o$ to $2\ x10^{-4}g_o$ causes the silicon concentration to drop by 0.2%, while under lower sinusoidal amplitude the silicon concentration along the growth interface is relatively constant. As a matter of fact, this figure also indicates that the silicon particle distribution is purely diffusive at a cut off sinusoidal amplitude of $2\ x10^{-4}g_o$.

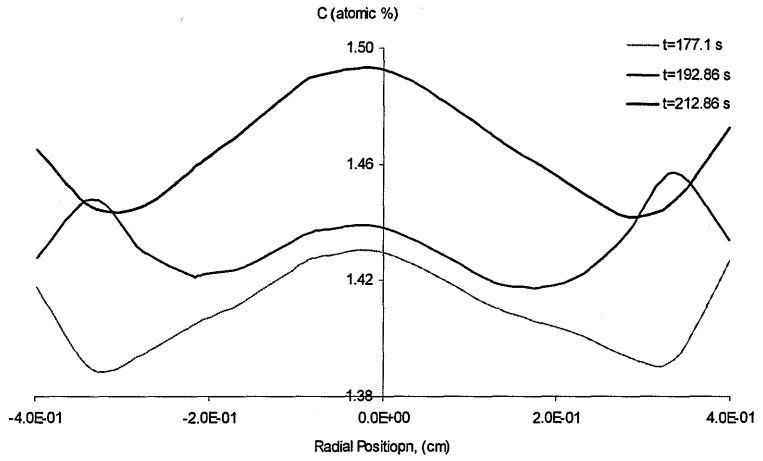

a) $A^* = 3 \times 10^{-3}$

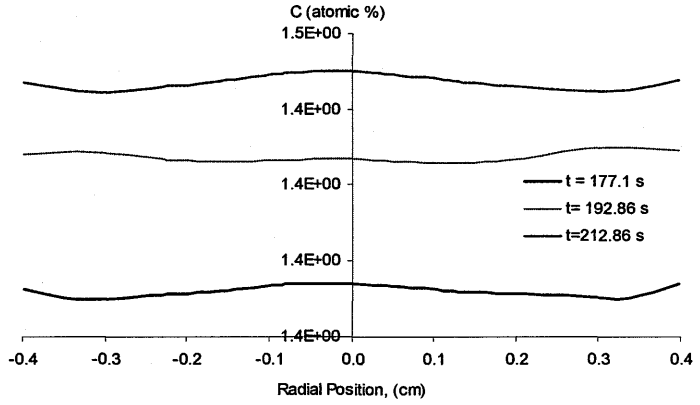

b) $A^* = 3 \times 10^{-4}$

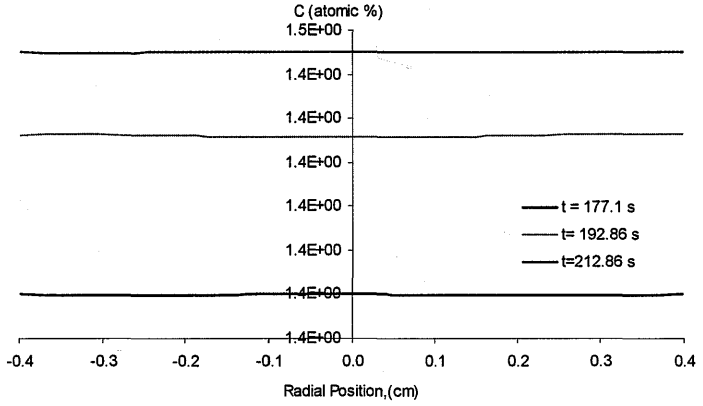

c) $A^* = 3 \times 10^{-5}$

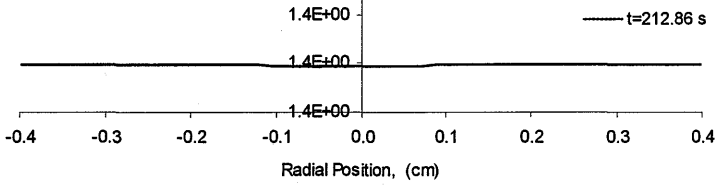

d) $A^* = 3 \times 10^{-6}$

Figure 4- 17: Silicon Concentration Profile near the growth interface along the radial direction $\varphi = 0°$ under sinusoidal gravitational effect with various amplitudes

4.4 Frequency Effect

The next step is to examine the effect of varying the frequency in the sinusoidal g-jitter. Similar to the amplitude analysis carried out in section 4.1 of this chapter, the realistic sinusoidal gravity case is used as the focal comparison case. A set of other different frequency cases, chosen to match that of the FOTTON 11 collected data, will be examined thoroughly to capture the effect of varying the frequency on the crystal growth process in space. The main equation representing the sinusoidal gravity was set as:

$$g^* = 10^{-6} + 3x10^{-3}\sin(\frac{2\pi f \tau D}{u_o}) \qquad (4\text{-}5)$$

Where, the frequency was varied from 2.8 x10^{-2} Hz to 5.6 x10^{-2} Hz, 0.1 Hz, and 1 Hz.

Initially, the gravitational effect on the solvent transient behavior, under the various frequencies of 2.8 x10^{-2} Hz to 5.6 x10^{-2} Hz, 0.1 Hz, and 1 Hz, were examined extensively. Based on the flow profiles, captured in Figure 4- 18 to 21, respectively at the various nodes location, it is noted that quasi-steady state is reached at 177 seconds in every case. Furthermore, the flow fluctuation period is also noted to correspond to the frequency of the sinusoidal gravity. At node 3930, the fluctuation period under sinusoidal gravity with frequency of 0.028, 0.056, 0.1, and 1 Hz are found to be around 37, 18, 10, and 1 seconds respectively, which do match the corresponding frequency. Note: because the size of the model being analyzed is very small, there is no phase lag between the applied frequency and the periodic behavior of the flow and silicon fluctuations. Previously in the amplitude effect analysis, it was seen that silicon migration to the growth interface is smoother under lower flow intensity. The same conclusion applies here since the silicon migration at the various nodes, as captured in parts b of Figure 4- *18* to 21 becomes smoother and slower as the frequency is increased.

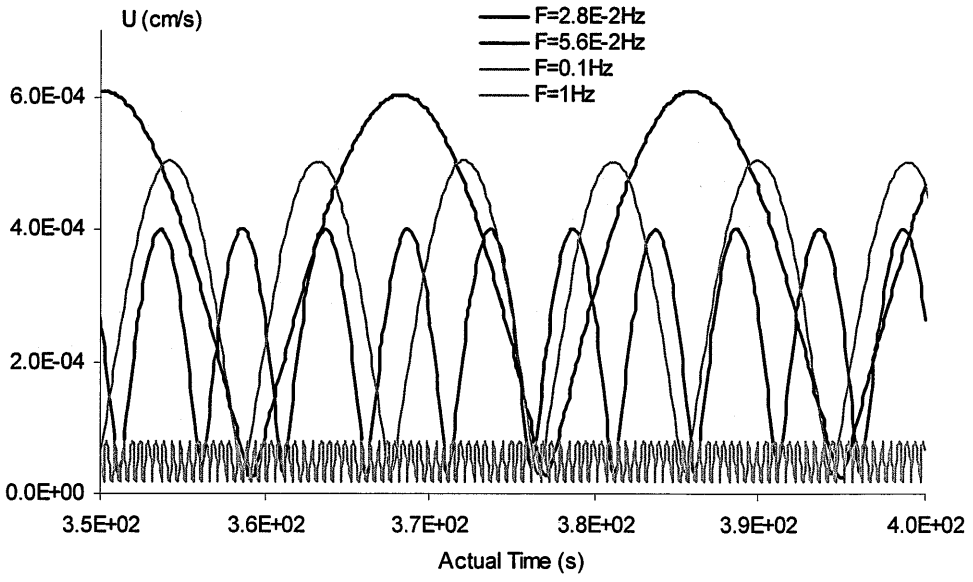

a)

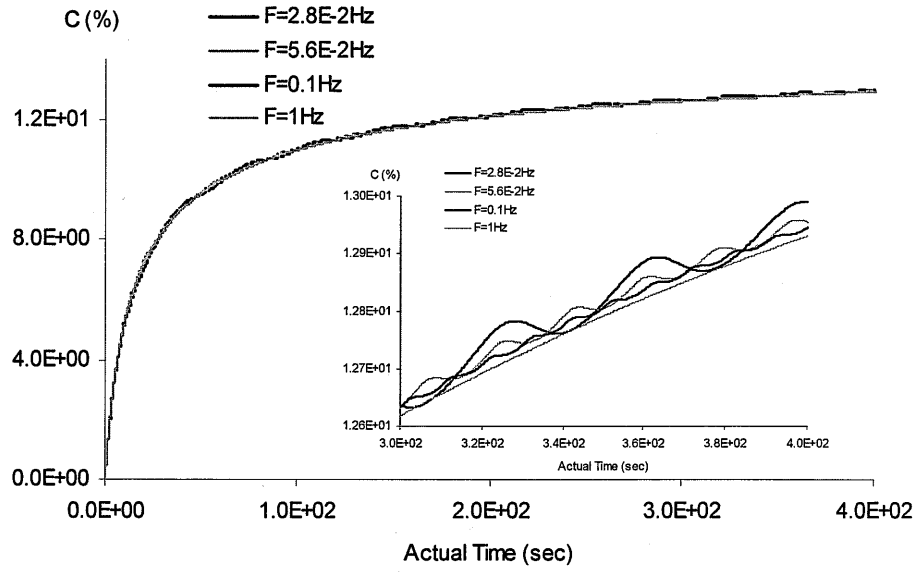

b)

Figure 4- 18: Transient behavior at node 3930 within the solvent regime under various sinusoidal Frequencies in terms of:

a) Flow behavior
b) Silicon Evolution

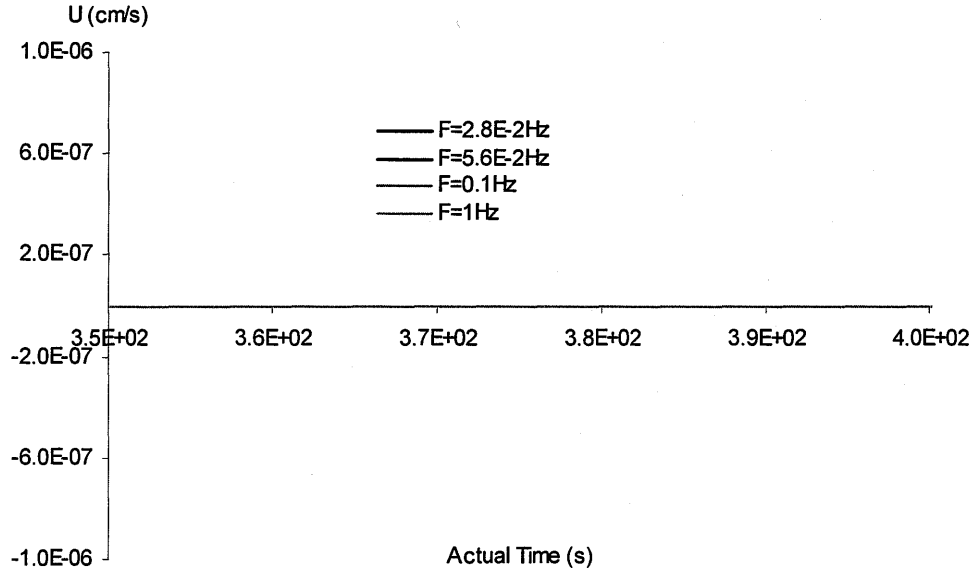

a)

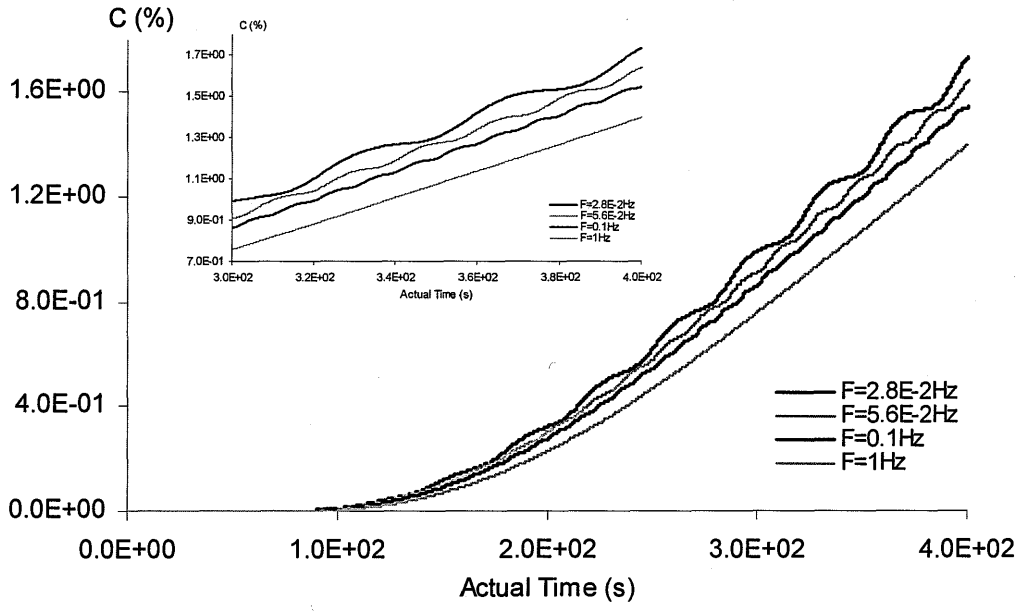

b)

Figure 4- 19: Transient behavior at node 1085 within the solvent regime under various sinusoidal Frequencies in terms of:

a) Flow behavior
b) Silicon Evolution

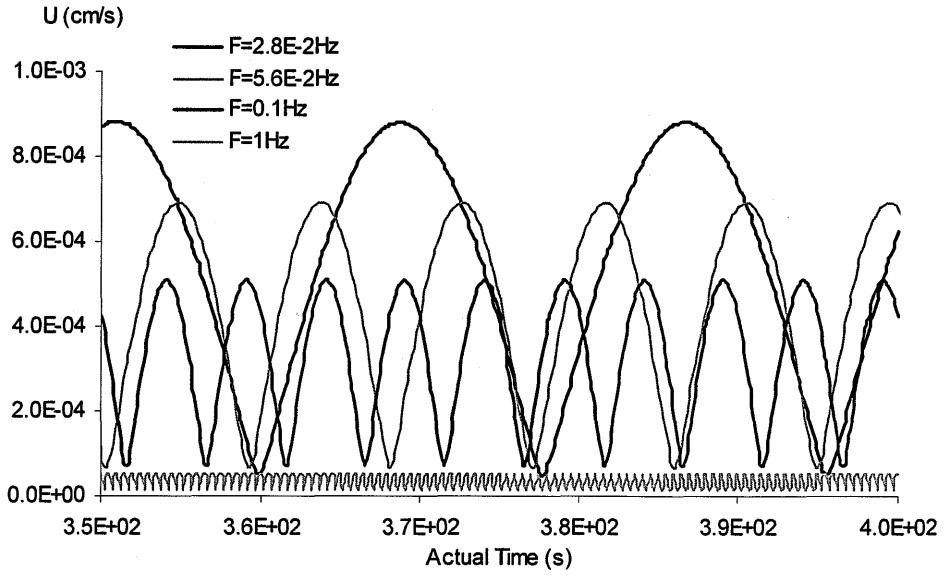

a)

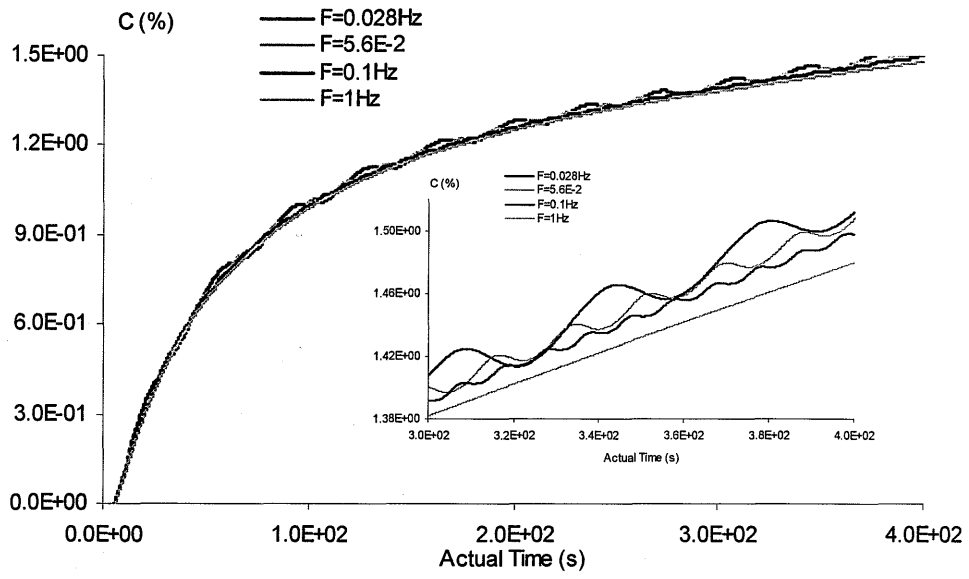

b)

Figure 4- 20: Transient behavior at node 1652 within the solvent regime under various sinusoidal Frequencies in terms of:

a) Flow behavior
b) Silicon Evolution

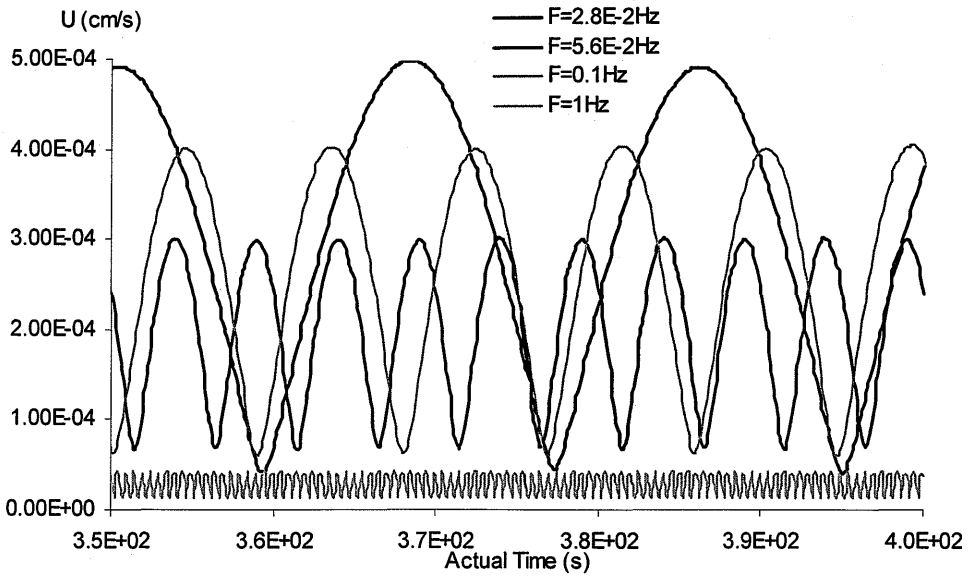

a)

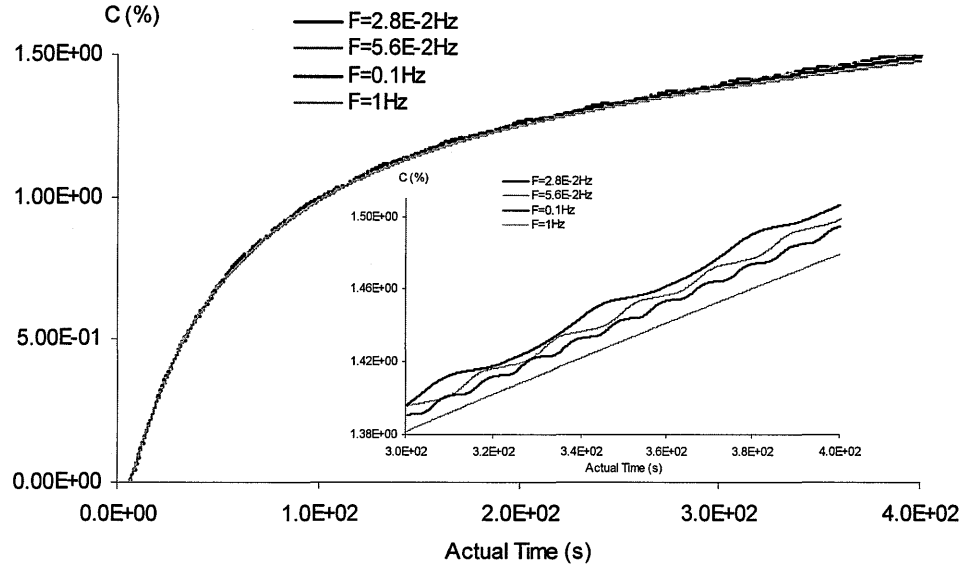

b)

Figure 4- 21: Transient behavior at node 1643 within the solvent regime under various sinusoidal Frequencies in terms of:

a) Flow behavior
b) Silicon Evolution

For completeness, the three dimensional transient behavior of the solvent regime is captured in Figure 22 to 25. Note, the transient flow behavior captured in parts a, b and c are with respect to

the oscillation period of flow, which is enforced by the applied frequency in every case. The same methodology is applied in capturing the transient silicon distribution behavior in parts d, e and f of every case. These figures clearly show that as the applied frequency is increased from $2x10^{-2}$ Hz to 5.6 $x10^{-2}$ Hz, 0.1 Hz and 1Hz, the maximum flow intensity gradually decreases from 1.01 $x10^{-4}$ cm/s to 8.31 $x10^{-4}$ cm/s, 6.02 $x10^{-4}$ cm/s, and 1.31 $x10^{-4}$ cm/s, respectively. This is a confirmation that flow intensity is negatively proportional to the frequency level. The same conclusion cannot be drawn in regards to the silicon distribution. According to the figures at hand the silicon distribution is not influenced by the frequency level.

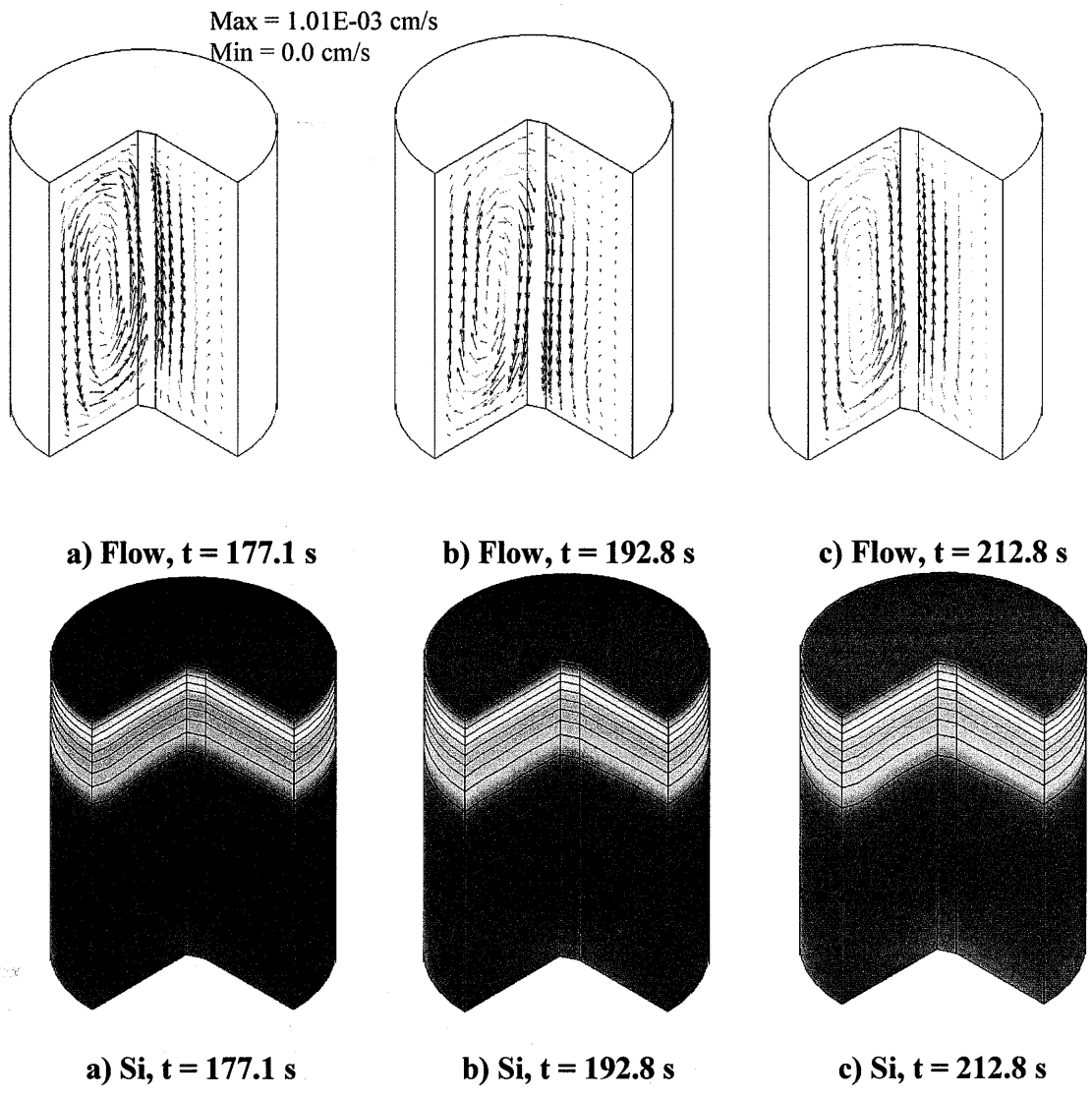

Figure 4- 22: 3D View of the Transient Pattern of Crystal solution under synthetic g-jitter with Frequency of 2.8E-02 Hz in terms of Flow behavior and Silicon Propagation

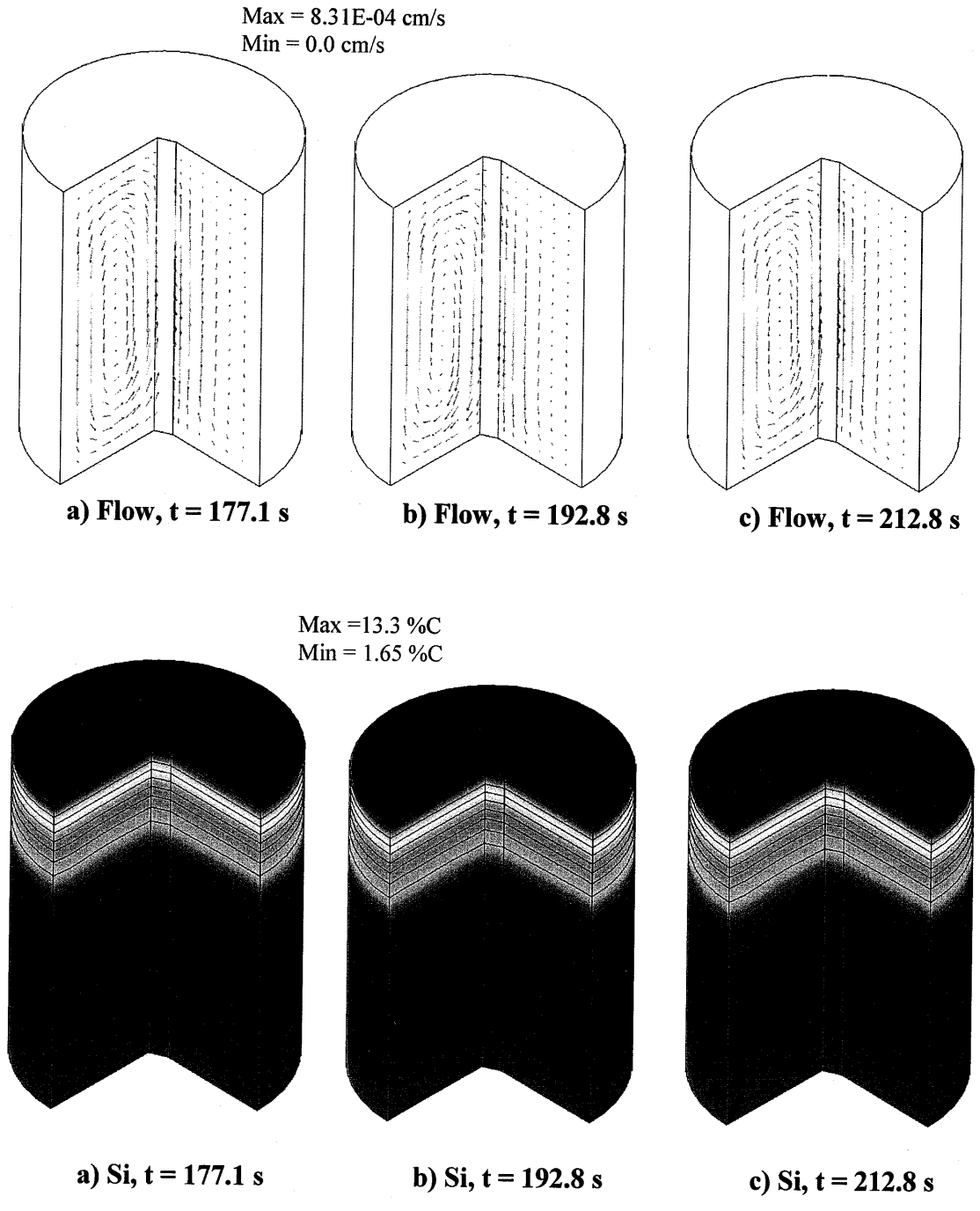

Figure 4- 23: 3D View of the Transient Pattern of Crystal solution under synthetic g-jitter with Frequency of 5.6E-02 Hz in terms of Flow behavior and Silicon Propagation

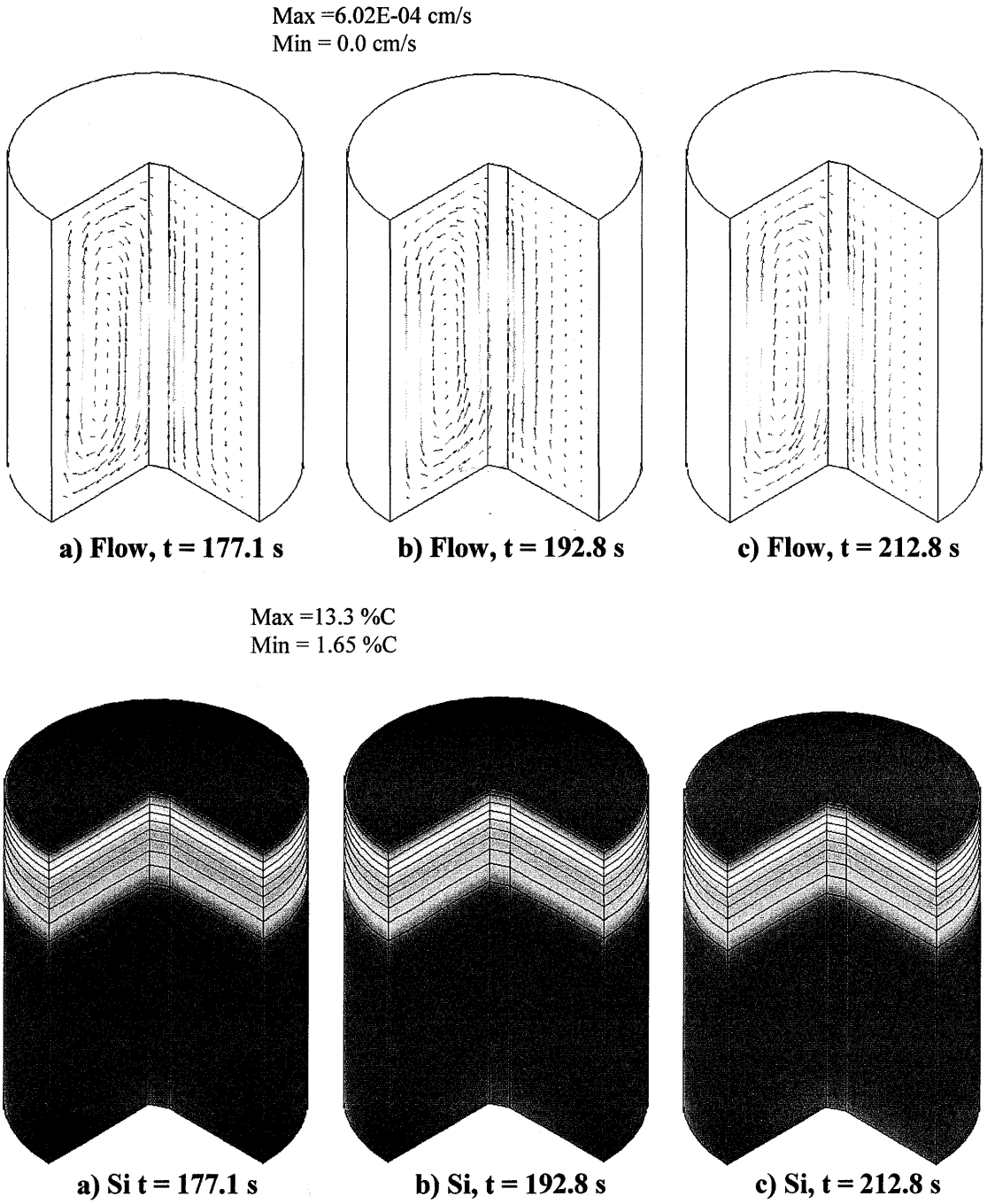

Figure 4- 24: 3D View of the Transient Pattern of Crystal solution under synthetic g-jitter with Frequency of 0.1 Hz in terms of Flow behavior and Silicon Propagation

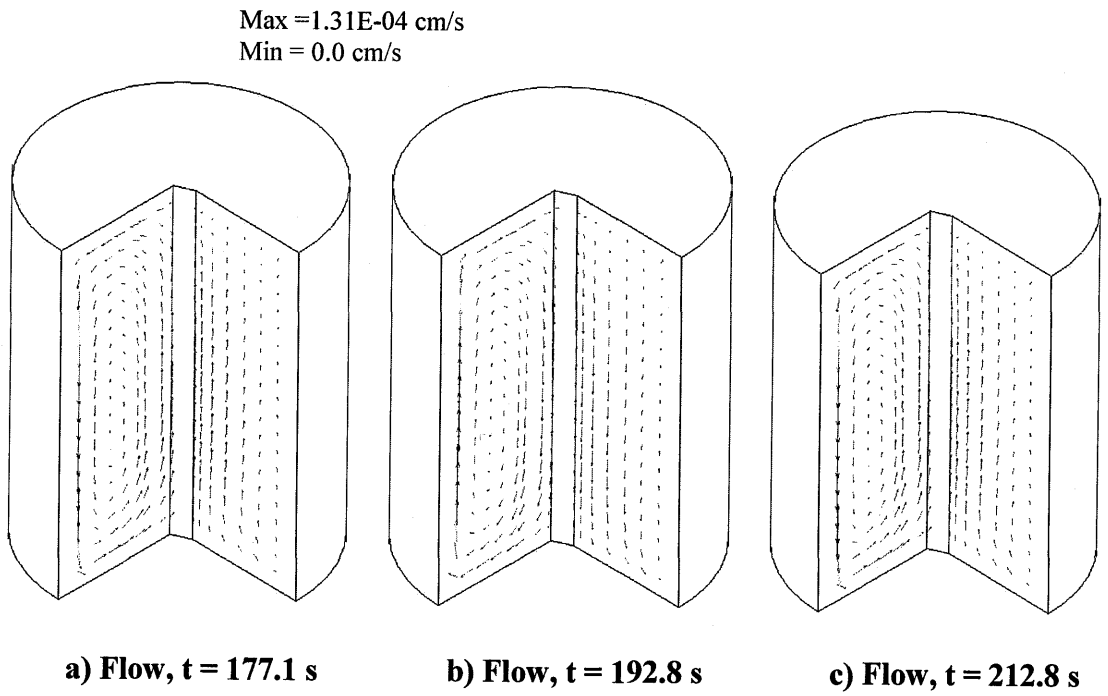

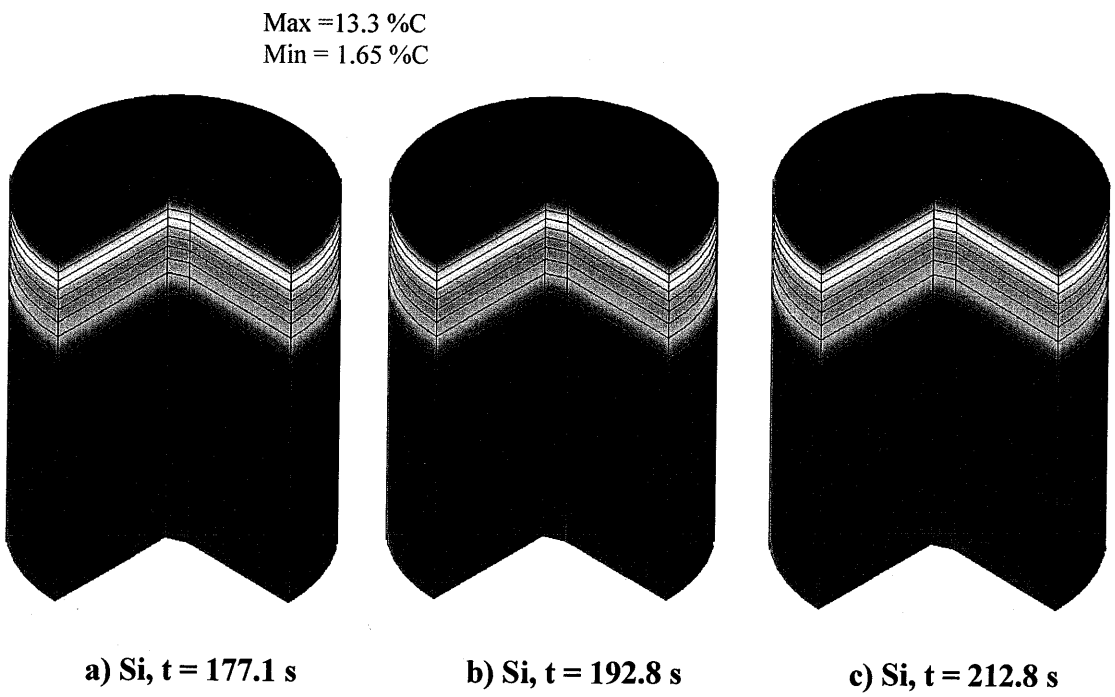

Figure 4- 25: 3D View of the Transient Pattern of Crystal solution under synthetic g-jitter with Frequency of 1 Hz in terms of Flow behavior and Silicon Propagation

Furthermore, the obtained results indicate that under higher frequency the amplitude of the flow is decreased. This behavior is further captured in figure 4-26, which highlight the maximum flow intensity at each node under different frequency effect. Note: the maximum flow intensity obtained is within the range of 10^{-4} cm/s, which was proven previously to have insignificant effect on the silicon migration. Based on this figure, the proportionality of the frequency increase to the flow intensity decease might not be linear, yet it is clear that the flow intensity is negatively proportional to the frequency applied. This phenomenon is due to the fact that once the frequency is increased the period of the flow fluctuation decrease applying restriction on the flow development. This is equivalent to suppressing the flow fluctuation leading to lower flow intensity.

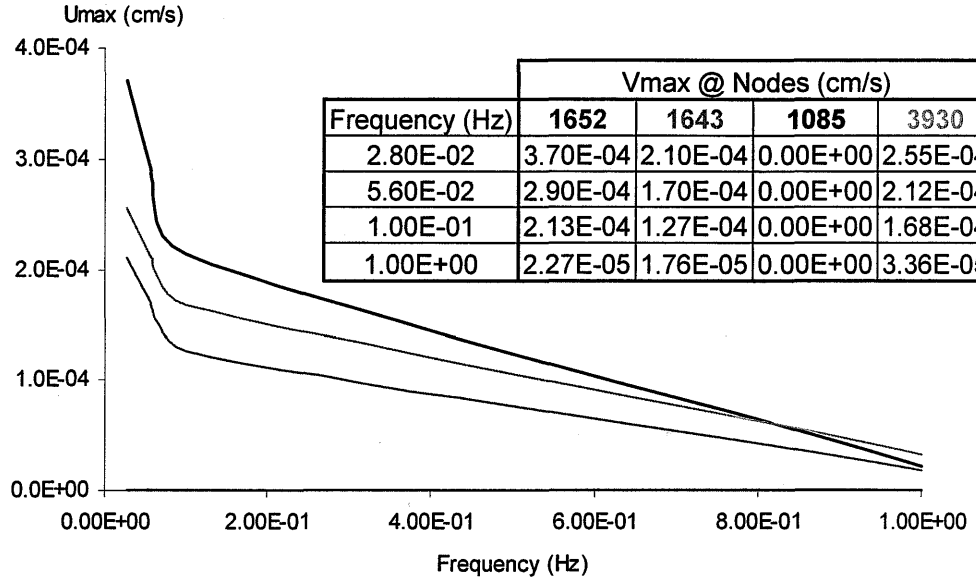

	Vmax @ Nodes (cm/s)			
Frequency (Hz)	**1652**	1643	**1085**	3930
2.80E-02	3.70E-04	2.10E-04	0.00E+00	2.55E-04
5.60E-02	2.90E-04	1.70E-04	0.00E+00	2.12E-04
1.00E-01	2.13E-04	1.27E-04	0.00E+00	1.68E-04
1.00E+00	2.27E-05	1.76E-05	0.00E+00	3.36E-05

Figure 4- 26: Maximum Flow Intensity Behavior Under Sinusoidal gravity with different Frequencies at Various locations within the solvent regime

Comparing the evolution of the flow and silicon concentration at nodes 1652 and 1643, it is noted that even though these two nodes are located on the same radial plan near the growth interface the maximum flow intensity at node 1643 is almost half of that at node 1652. In return, the rate of the silicon migration is influenced. Figure 4-27 is a snapshot, at 340 seconds, of the silicon

concentration at these two nodes under the different frequencies. If we examine this figure we can see that the silicon concentration at the two nodes under the lowest frequency of 2.8 $x10^{-2}$ Hz is different by 0.02 %C only, while under higher frequency the silicon concentration is identical at the two locations. Therefore, even thought at the lowest frequency the silicon distribution shows a hint of 3D complexity, this complexity vanishes as the frequency is increased. It is also worth noting through this figure that the silicon concentration decreases within the range of 0.01 %C as the frequency is increased. This is a confirmation that silicon transportation is dominated by diffusion. Therefore, by further suppressing the flow fluctuation through the application of higher frequency, the migration of silicon particles to the growth interface becomes linear leading to better silicon distribution at the growth interface as seen in Figure 4- *28*. The disadvantage of such behavior is slower crystal growth rate.

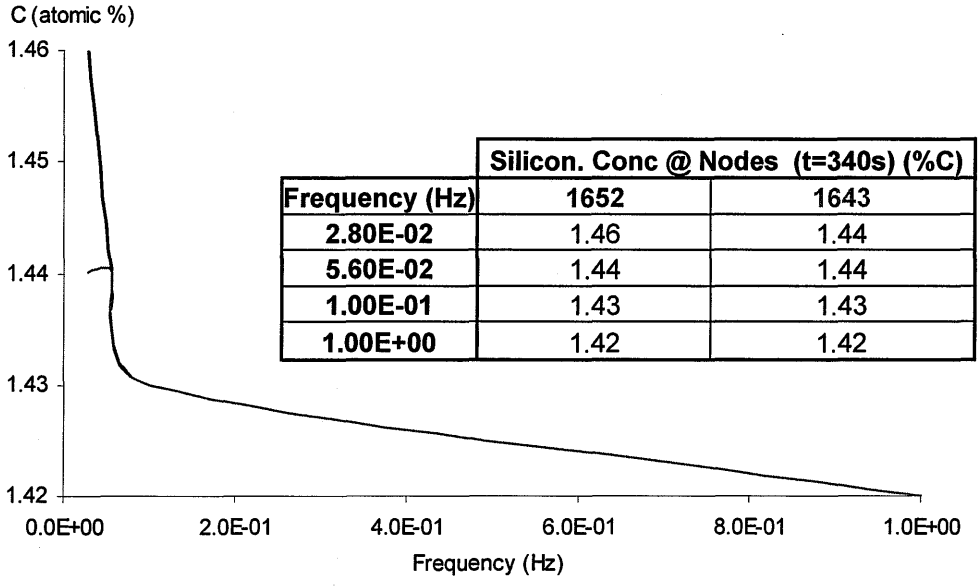

	Silicon. Conc @ Nodes (t=340s) (%C)	
Frequency (Hz)	**1652**	**1643**
2.80E-02	1.46	1.44
5.60E-02	1.44	1.44
1.00E-01	1.43	1.43
1.00E+00	1.42	1.42

Figure 4- 27: Silicon Concentration at Nodes 1652 and 1643 under Various Frequencies at snapshot t=340 seconds

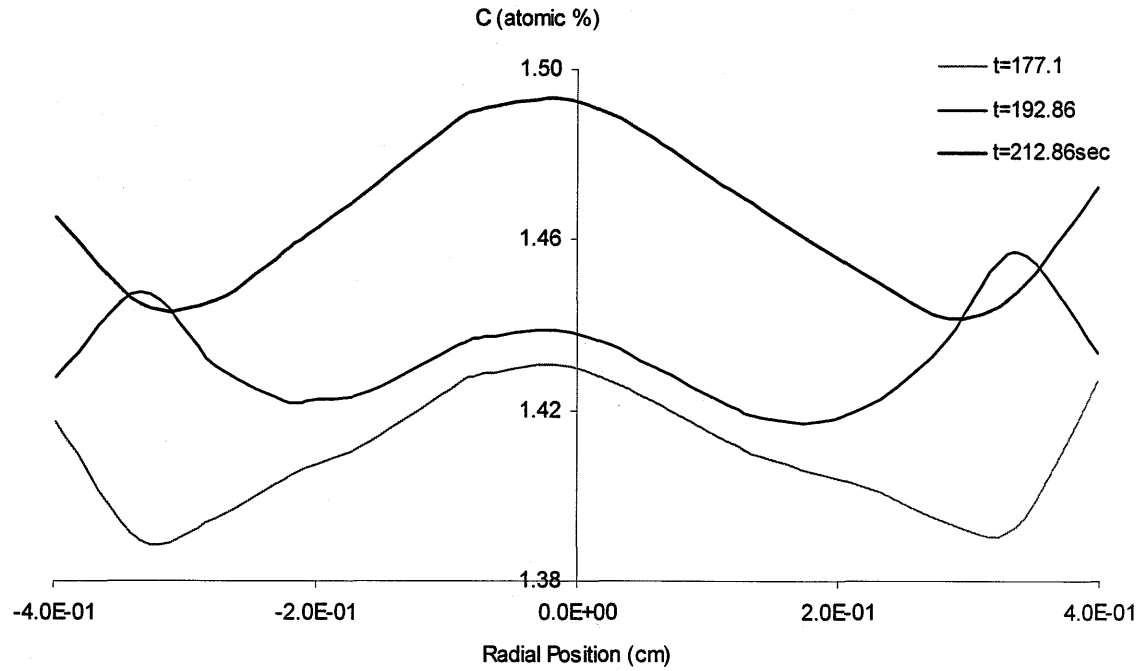

a)) F = 2.8x10^{-2} Hz

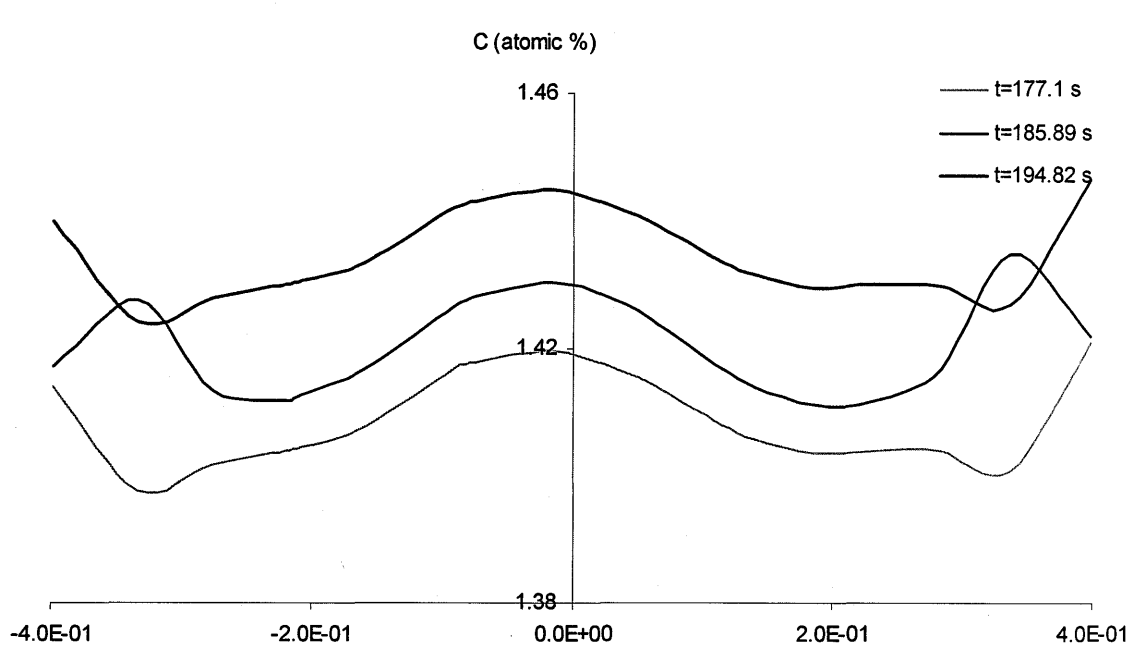

b) F = 5.6x10^{-2} Hz

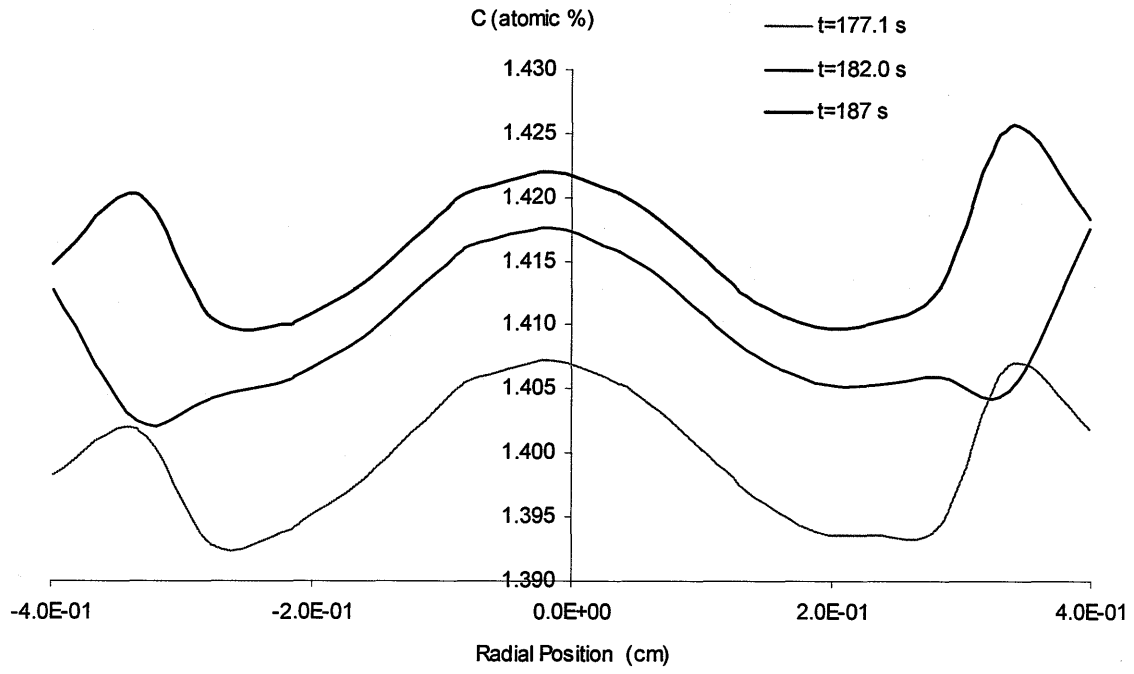

c)) F = 0.1 Hz

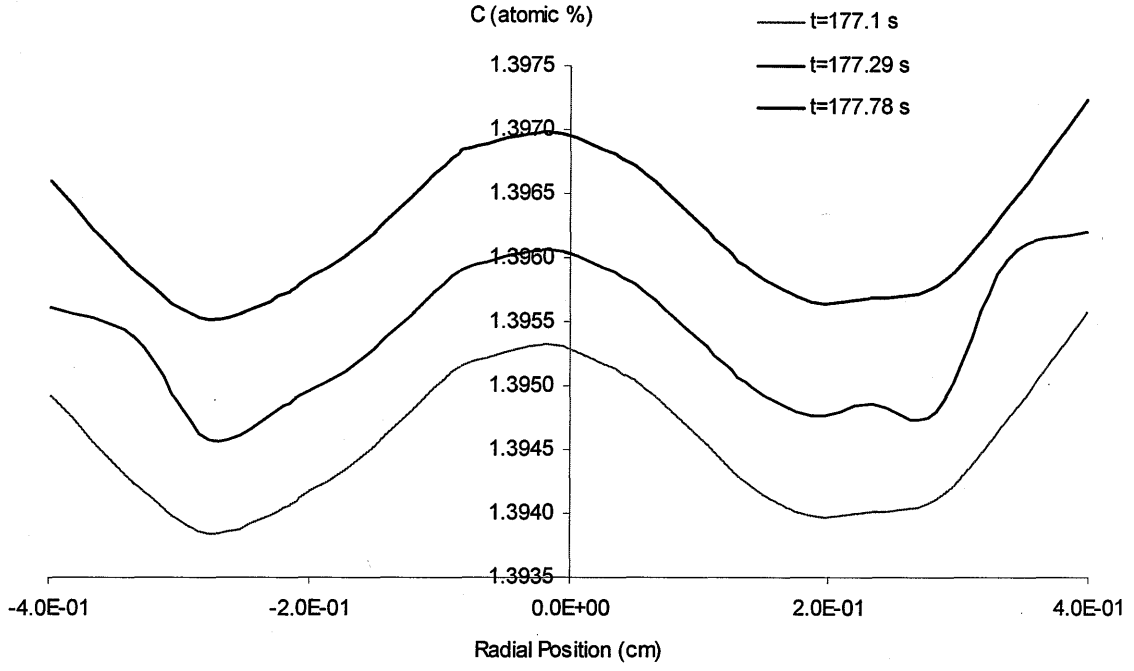

d)) F = 1 Hz

Figure 4- 28: Silicon Concentration Profile near the growth interface along the radial direction $\varphi = 0^{\circ}$ under sinusoidal gravitational effect with various Frequencies

Based on these findings, it is possible to conclude that sinusoidal gravity, with a range of frequency of 1 Hz to 2.8×10^{-2} Hz, have negligible effect on the silicon migration since the silicon transportation is driven by diffusion under the current flow intensity.

4.5 Real G-Jitter Effect

Based on previous studies conducted on crystal growth under real g-jitter forces [6, 9, 13, 15, 18, 20] one would expect the g-jitter force to impose some flow disturbance within the melt, which would cause noticeable disturbance to the silicon concentration distribution. Yet, these expectations were not met in our present analysis.

Based on the variation of the residual static gravity while keeping a constant sinusoidal jitter analysis, it was concluded that the nature of the flow is determined by the magnitude of the combined effect of static gravity and the amplitude of the sinusoidal gravity. As the magnitude of the static gravity drops to below 10^{-4} g_o, the flow is dominated by diffusion. Therefore, in real g-jitter cases, where the static gravity is in the range of 10^{-6} g_o, the flow is expected to be in diffusion mode. The analysis of the amplitude and frequency of the sinusoidal g-jitter are also useful in determining the expected behavior of the crystal growth under real g-jitter.

The amplitude of the sinusoidal jitter determines the intensity of the fluctuations experienced in the melt zone, while the frequency determines the period of these fluctuations. Furthermore, the amplitude of the fluctuation can be suppressed by increasing the frequency level. Combining the amplitude and the frequency effect on the flow behavior, it is concluded that sinusoidal gravity disturbance can have a visible disturbance only if the amplitude and frequency are within the range of 10^{-3} g_o and 10^{-3} Hz, simultaneously. In our case, the sinusoidal ingredient of the real g-jitter consists of amplitude within a range between 10^{-5} g_o to 10^{-6} g_o and a frequency within the

range of 10^{-3} Hz. Since the amplitude is very low, we would not expect much noticeable disturbance even under such low frequency.

To further mimic possible space environment under which crystal would be grown, two simulations will be considered as possible environment for crystal growth. A relatively severe disturbance that was captured using an accelerometer on board the FOTON space shuttle will be used for our simulations. This worst-case scenario, known as the Tramp case, consists of disturbance of the range of 10^{-5} g_o. Such environment occurs when many other variables contribute to perturbations such as active crew motions, mechanical vibrations, and space shuttle maneuvers. An ideal condition with minimal disturbance will also be considered in a second real g-jitter simulation known as QSAMP case, which has smaller disturbances of the range of 10^{-6} g_o. Such low intensity fluctuation is obtained when crew members are asleep with not as much mechanical vibration and stationary shuttle gliding. In both growth conditions the frequency will be within the range of 10^{-3} Hz.

Note, under real space environment residual gravity is imposed on the three directions x, y and z. Therefore, to represent the collected data of these disturbances gravity will be calculated as, $g = \sqrt{g_r^2 + g_\varphi^2 + g_z^2}$, as shown in Figure 4- *29*. The results obtained from these simulations will provide us with the basic understanding of the possible outcome of an experimental crystal growth in space.

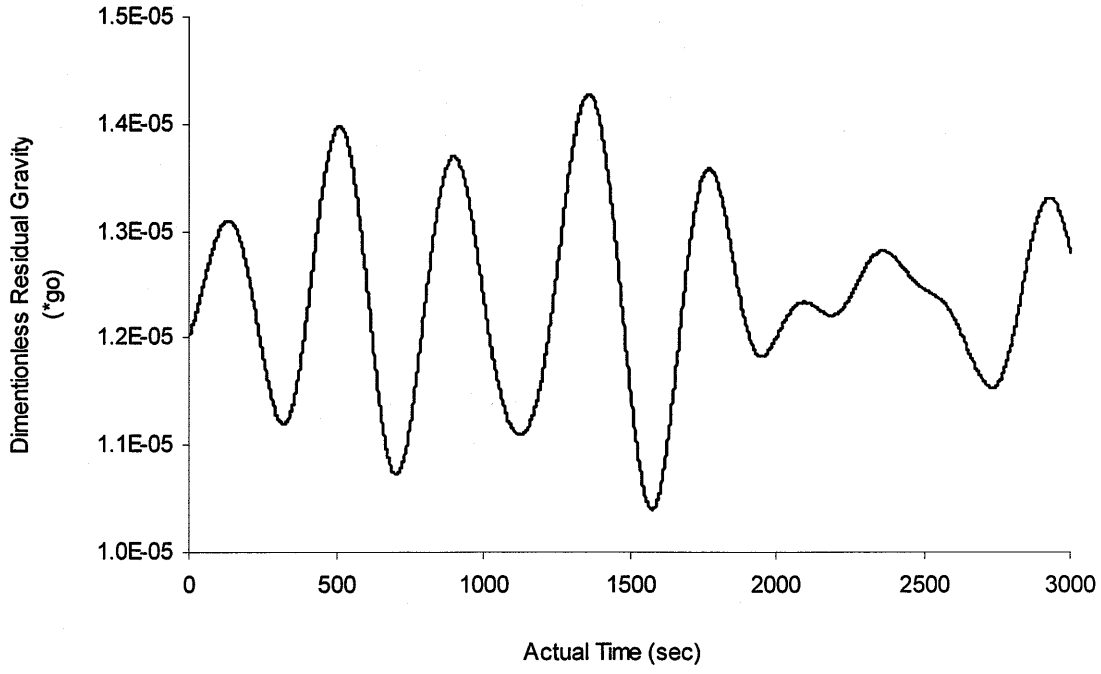

a) TRAMP

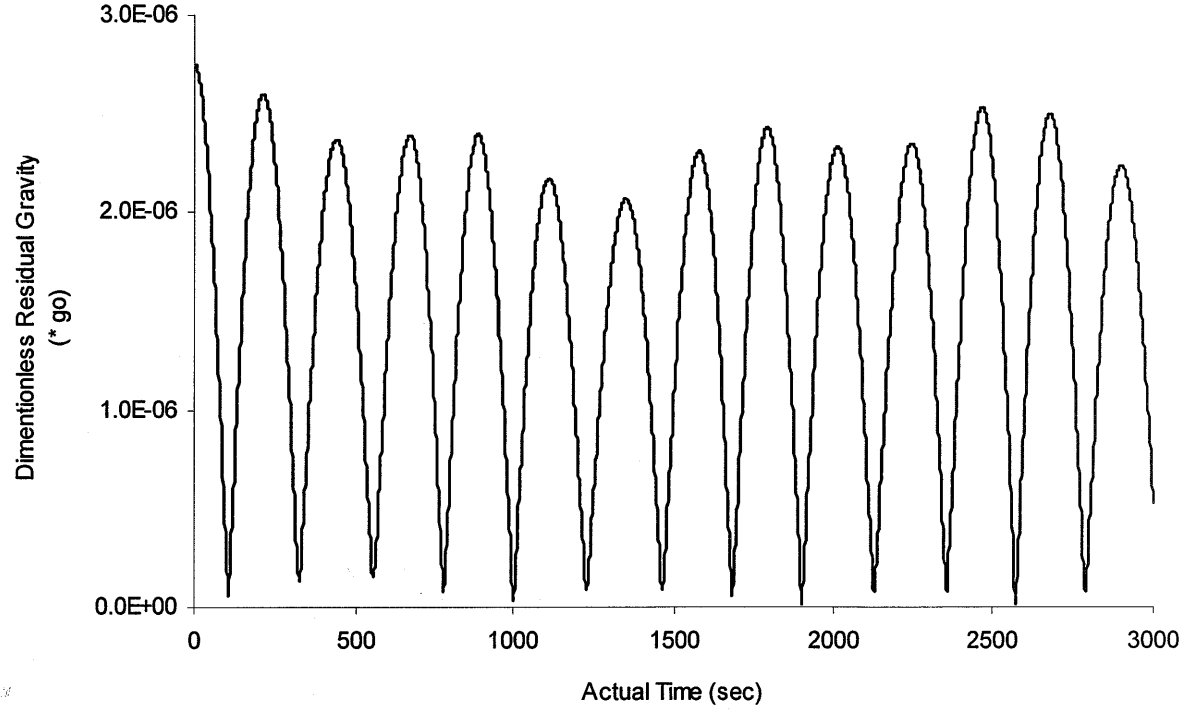

b) QSAMP

Figure 4- 29: g-jitter Model- Dimensionless Acceleration on board Foton 12 under two cases

4.5.1 TRAMP Case

Considering the worst-case scenario, the Tramp case was studied extensively. The intensity of the residual gravity is small enough to suggest the flow would be diffusive in nature. Yet, the frequency is rather too small to eliminate the possibility of flow fluctuation development.

Based on the results obtained as highlighted in Figure 4-30, flow fluctuation was noted to develop perpendicular to the growth interface, which is unlike the previously studied cases.

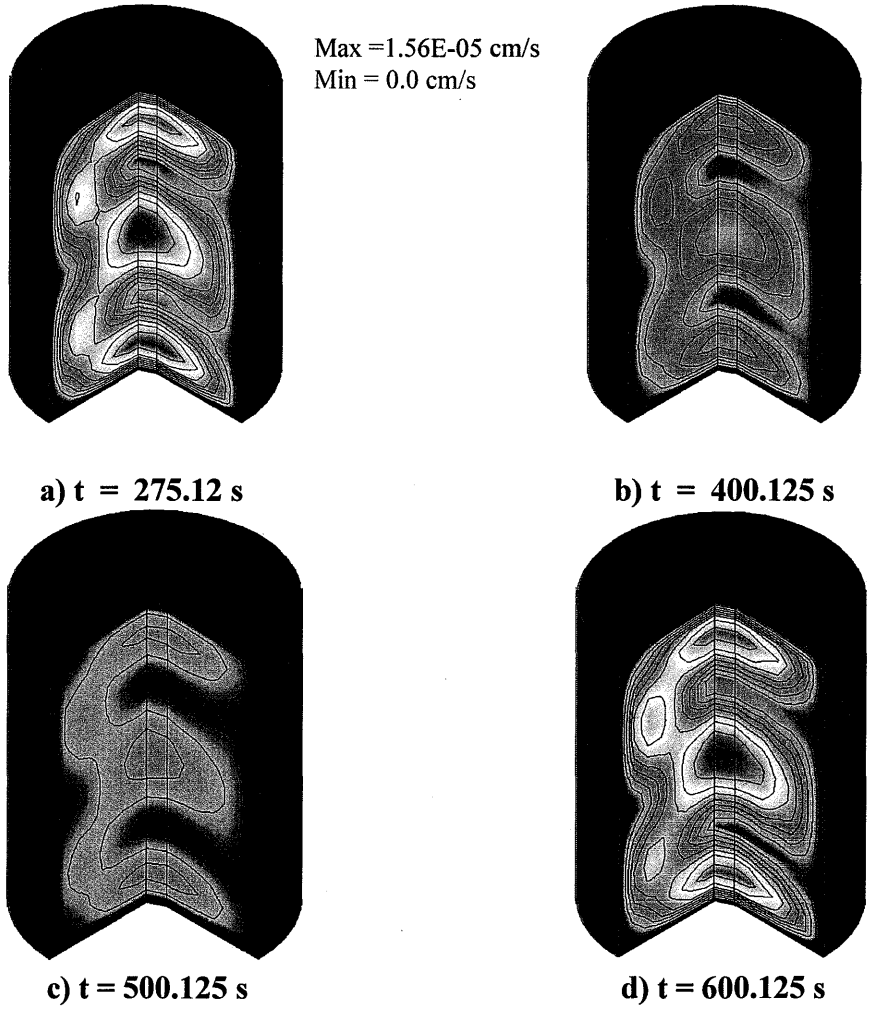

Figure 4- 30: 3D View of the Transient Flow behavior of the Crystal solution under the TRAMP Case

This phenomenon is due to the fact that on FOTTON 12 space mission; the residual gravity, both its static and sinusoidal components, was noted to be more concentrated along the y-direction, i.e. parallel to the growth interface plan. Consequently, the flow intensity and its fluctuations act along the y-direction. This phenomenon was seen and discussed in previous papers [8, 21].

In a realistic setting, three forces acting on the melt in three different directions would lead to the formation of flow along the three directions summing up to act along the direction with the highest gravitational forces. In return these flow cancellation leads to the formation of low intensity flow of the range of 10^{-5} cm/sec as seen in Figure 4-31.

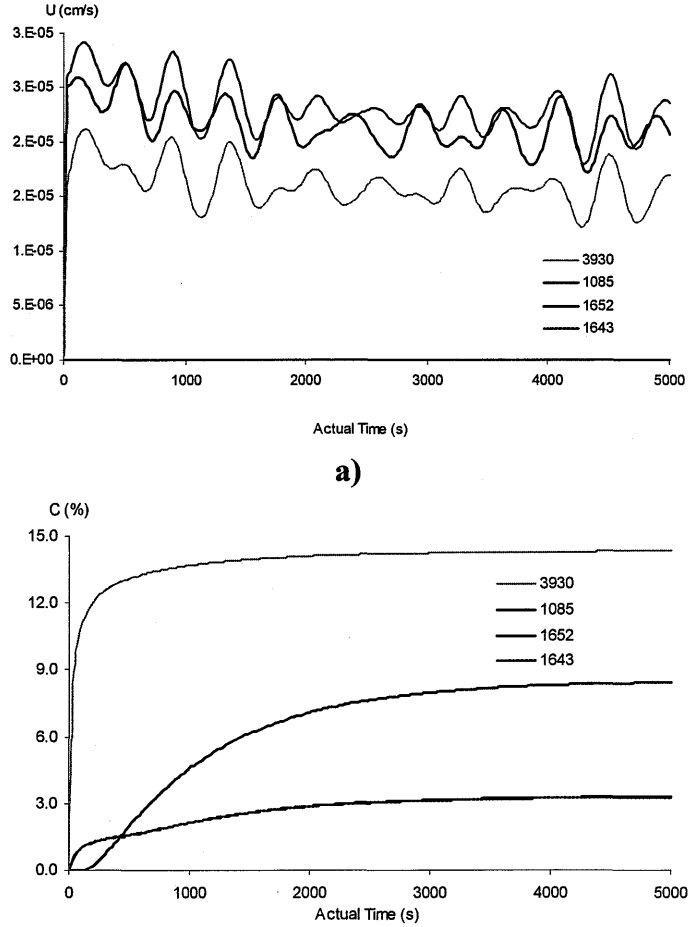

Figure 4- 31: Transient behavior at Various Nodes under Real g-jitter effect, Tramp Case, for:

a) The Flow plot

b) The Silicon distribution

Note, this flow intensity is proportional to the overall gravitational intensity applied during the TRAMP case of 10^{-5} g_o. Previously, it was proven that flow with intensity of 10^{-4} cm/sec can be considered in diffusive mode. Therefore, such flow would not be expected to have an effect on the silicon distribution as it propagates down toward the growth interface. This is clearly seen in Figure 4-32.

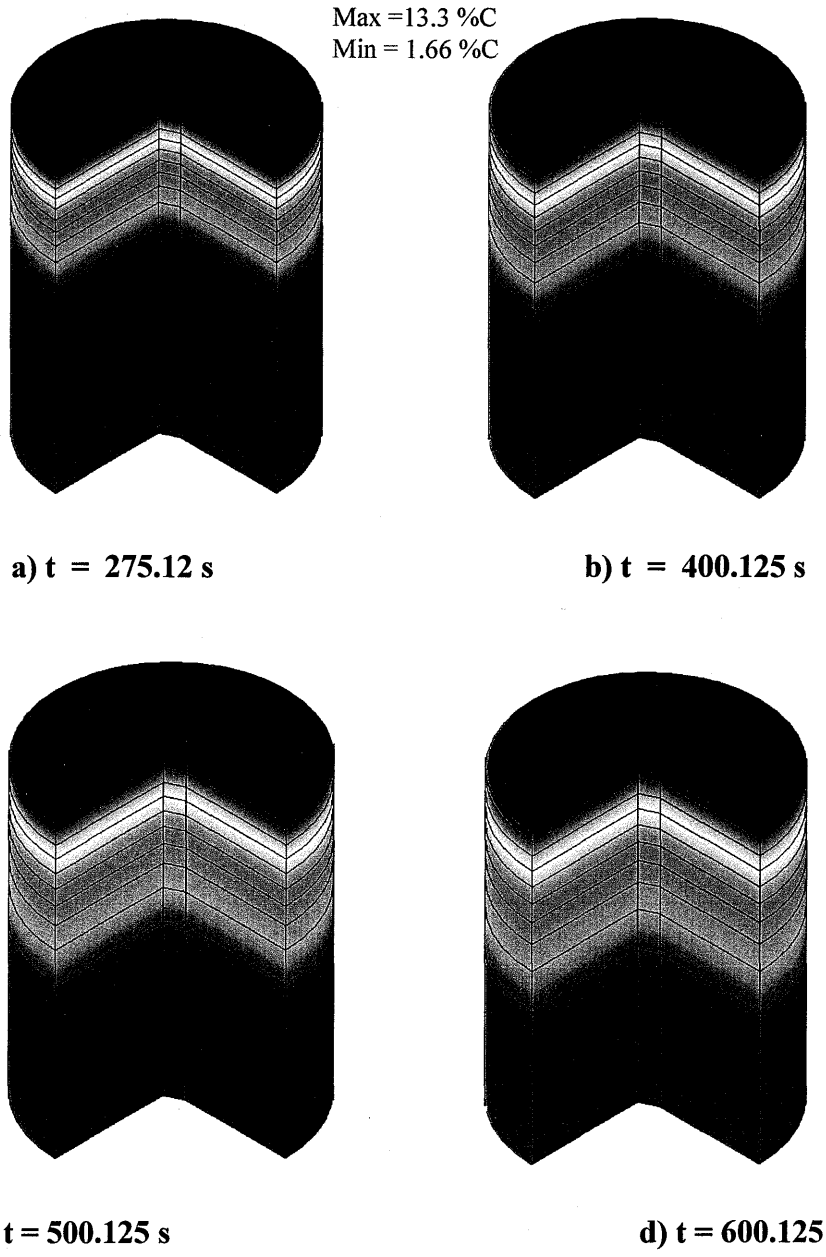

Figure 4- 32: 3D View of the Transient Silicon Concentration Propagation of the Crystal solution under the TRAMP case

As a matter of fact, even the complexity of the flow and the silicon concentration near the growth interface was noted to disappear leading to pure uniform silicon distribution along both the φ=0° and φ=90° directions. This is clearly seen by comparing Figure 4-33 to Figure 4- *34*, which capture both the flow and silicon concentration along the growth interface at different snapshots in time.

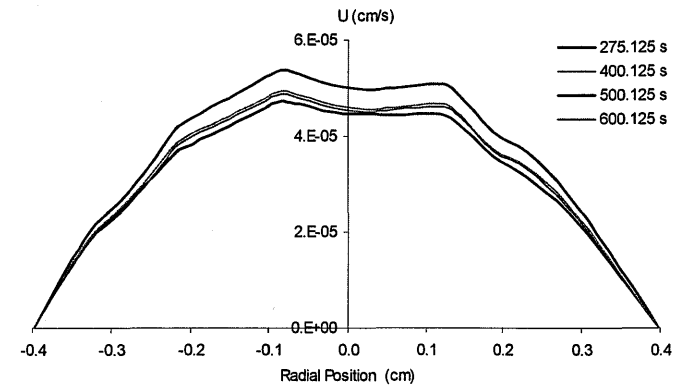

a)

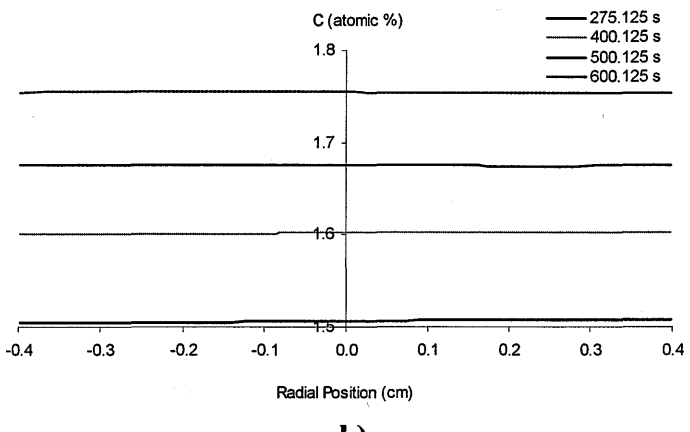

b)

Figure 4- 33: Transient Behavior near the growth interface, along φ=0°, under the Tramp g-jitter growth condition in terms of:

a) Flow Behavior

b) Silicon Distribution

At 77.03 seconds the average silicon concentration near the growth interface was found to be 1.5063 %C and 1.5077 %C along φ=0° and φ=90° directions respectively. This difference of 0.0014 %C, which is almost at our margin of validation, is very low to consider the disturbance of

the flow to have an effect on the silicon concentration behavior. Therefore, under such low flow intensity and such obtained silicon distribution, it is safe to conclude that the silicon migration is governed by pure diffusion.

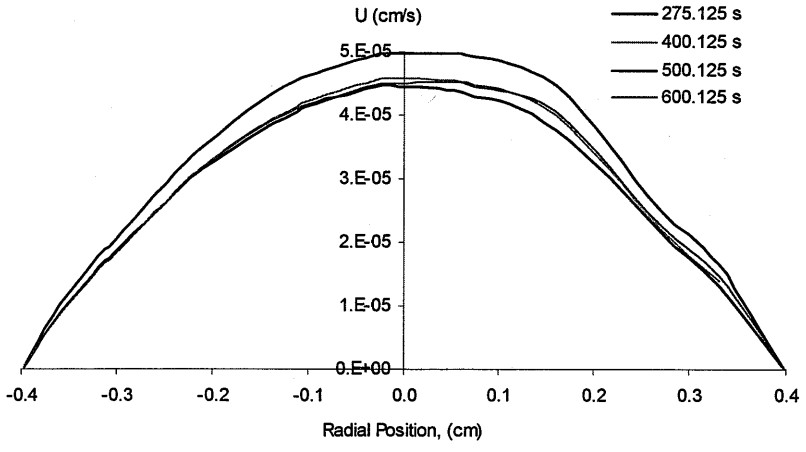

a)

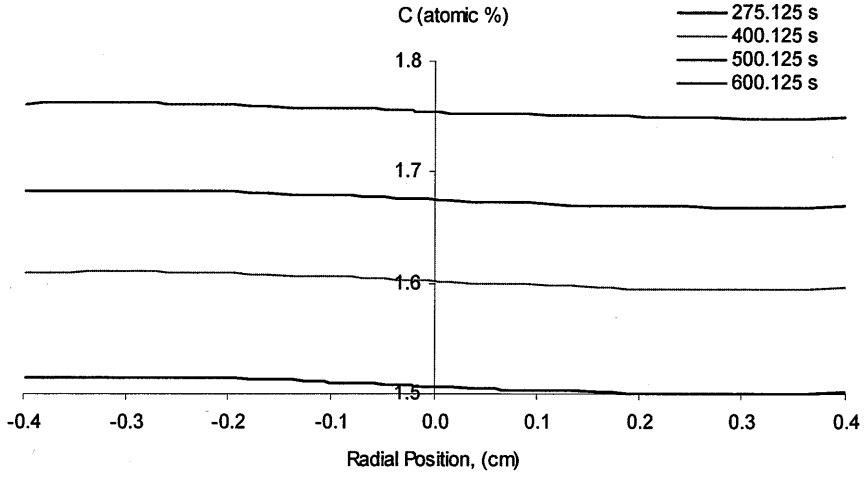

b)

Figure 4- 34: Transient Behavior near the growth interface, along φ=90°o, under the Tramp g-jitter growth condition in terms of:

a) Flow Behavior
b) Silicon Distribution

Previous studies [11] have used vibration effect as a mean of "stirring" the melt to obtain uniform specie distribution. Yet, the cost was always the non-desirable convective flow that was created by the gravitational terms. Yet, in this current situation, g-jitter with low gravitational intensities and low frequency has proven to be successful in acting as a 'stirring' agent while eliminating the undesirable convective flow.

Based on this analysis we can summarize our findings in two points

- The over all gravitational intensity effect lead to a low flow intensity within the range of 10^{-5} cm/s, which was proven to have insignificant effect on the silicon migration
- The combined effect of low frequency and low flow intensity within the solvent regime provided us with a mean to stir the solution in order to obtain better silicon distribution.

Accordingly, it is valid to conclude that the crystal growth environment in space served us well by providing an ideal growth environment to grow the perfect crystal structure.

4.5.2 QSAMP Case

Equivalent behavior has been noted in the solvent regime under lower gravitational effect of the range of 10^{-6} g_o and a frequency effect within the range of 10^{-3} Hz.

Again, as noted in Figure 4-35, in the QSAMP case the gravitational fluctuation acting along the y-direction was the highest and more uniform in nature compare to that of the TRAMP case.

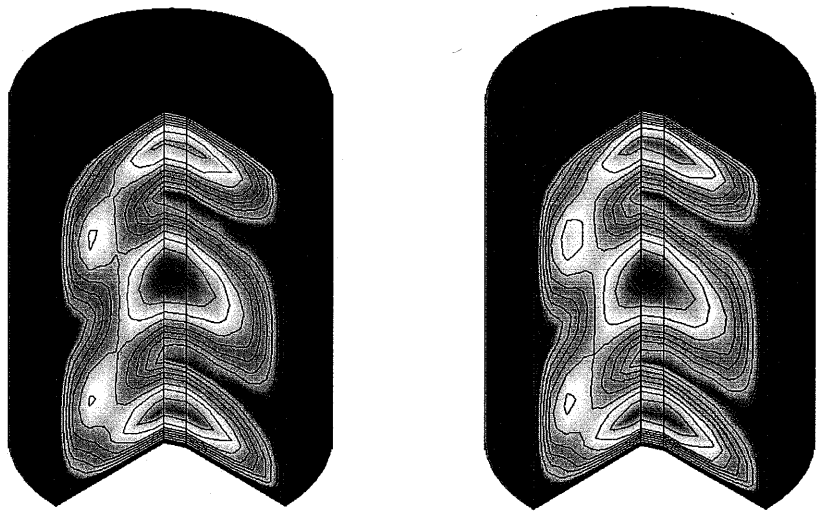

a) t = 275.12 s **b) t = 400.125 s**

Max =7.31E-06 cm/s
Min = 0.0 cm/s

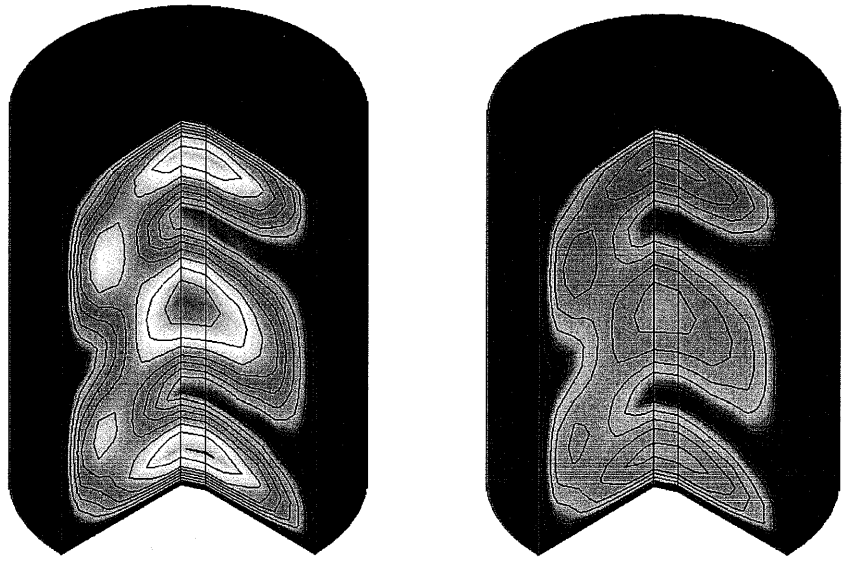

c) t = 500.125 s **d) t = 600.125 s**

Figure 4- 35: 3D View of the Transient Flow Behavior of the Crystal solution under the QSAMP Case

As a result of lowering the gravitational intensity, lower flow intensity of the range of 10^{-6} cm/sec was attained throughout the evolution of flow as seen in Figure 4-36.

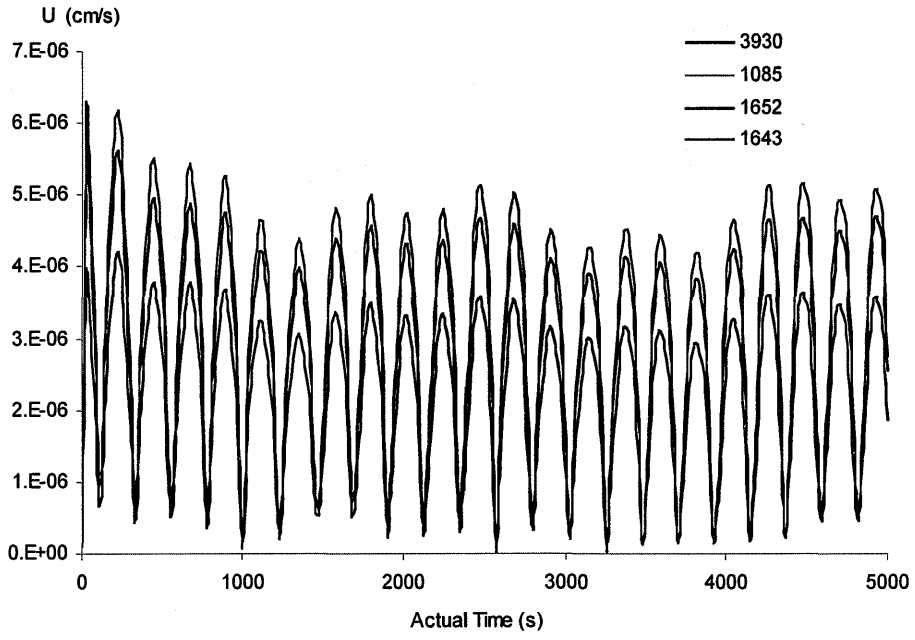

a)

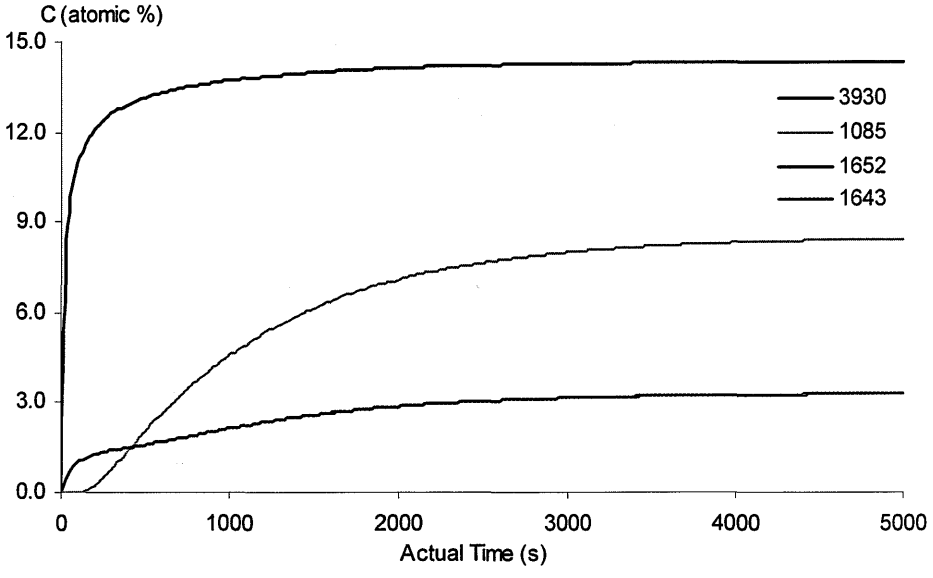

b)

Figure 4- 36: Transient behavior at Various Nodes under Real g-jitter effect, QSAMP Case, for:

a) The Flow plot

b) The Silicon Distribution

Because the flow is in diffusive mode, within that flow intensity range, the same non-complex and uniform silicon distribution along the solvent regime was obtained. This is clearly illustrated

in Figure 4-37. As a matter of fact, the decrease in flow intensity did not even contribute to the evolution of the silicon concentration as it propagates down toward the growth interface. As a result the same crystal growth rate is obtained.

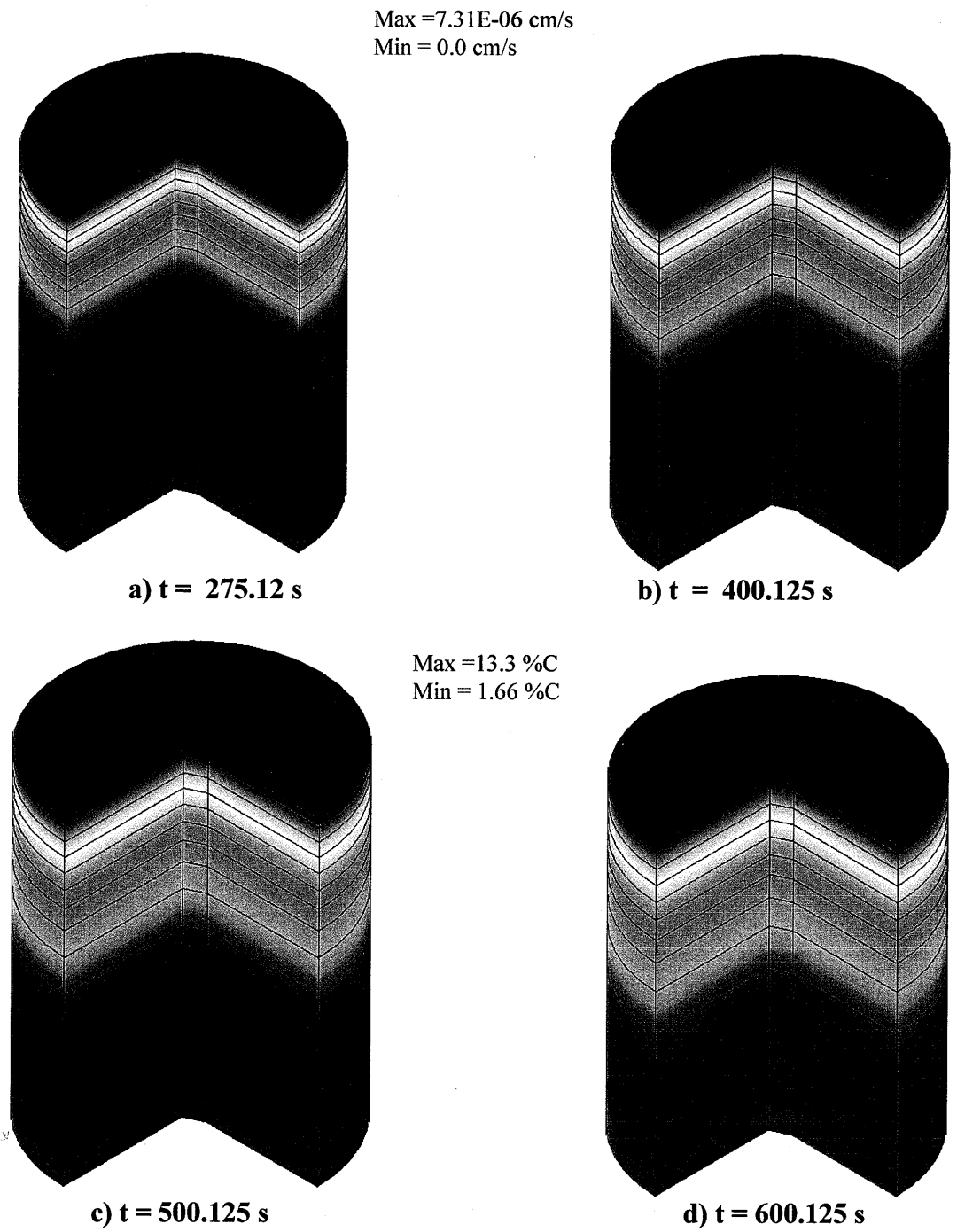

Figure 4- 37: 3D View of the Transient Silicon Concentration Propagation of the Crystal solution under the QSAMP case at:

Comparing the flow and the silicon distribution along φ=0° and φ=90° direction as seen in Figure 4- *38* and Figure 4- *39* simultaneously, it is noted that the hint of flow complexity seen during the TRAMP case completely disappears.

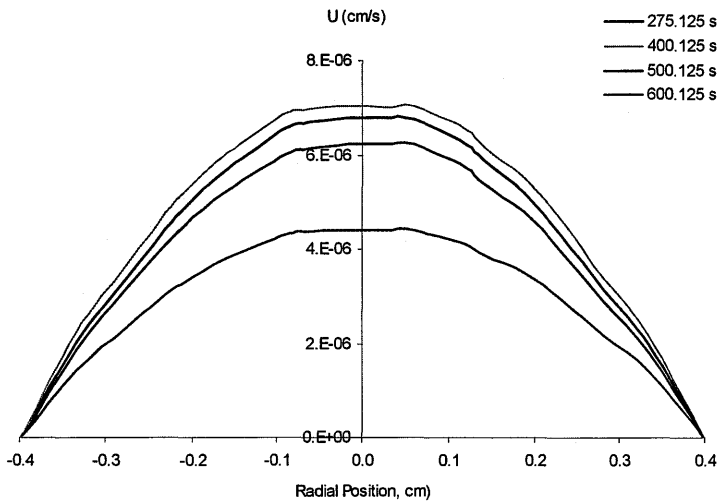

a)

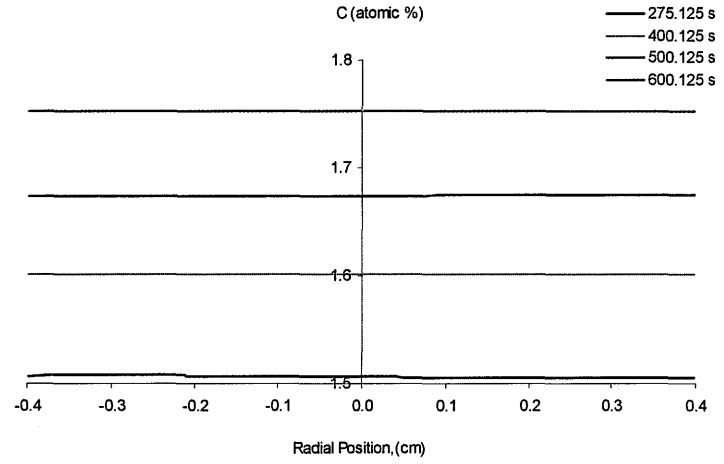

b)

Figure 4- 38: Transient Behavior near the growth interface, along φ=0°, under the QSAMP g-jitter growth condition in terms of:

a) Flow Behavior

b) Silicon Distribution

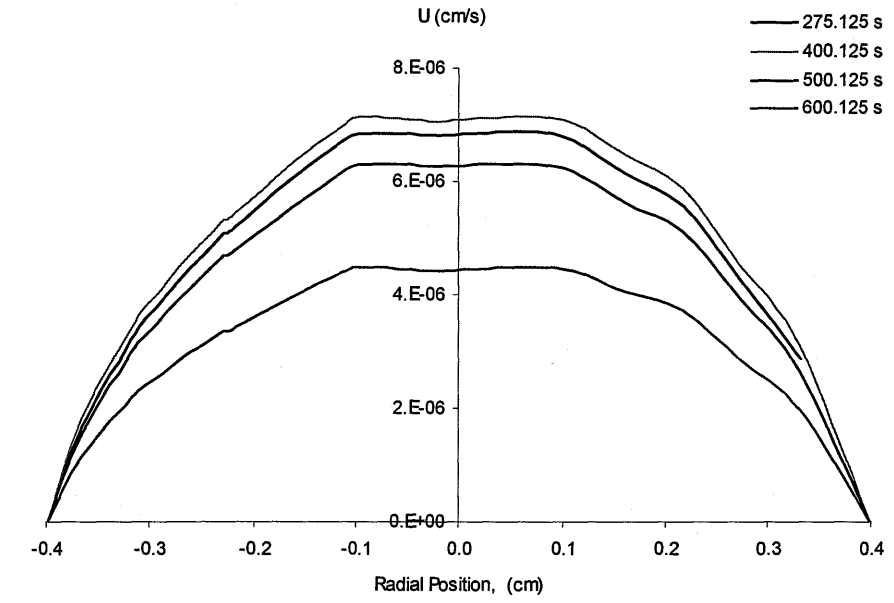

a)

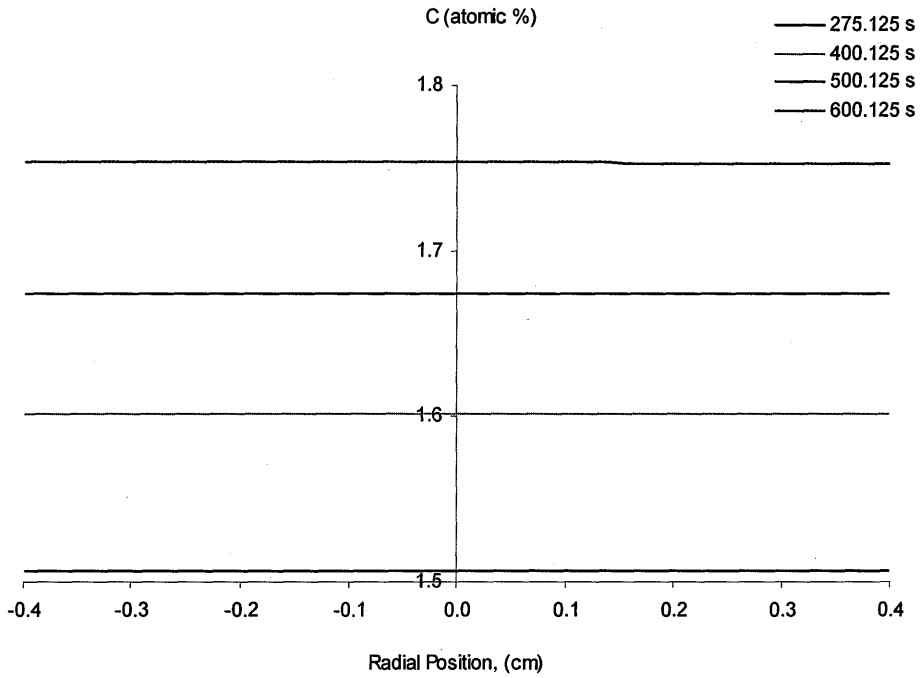

b)

Figure 4- 39: Transient Behavior near the growth interface, along φ=90°, under the QSAMP g-jitter growth condition in terms of:

a) Flow Behavior

b) Silicon Distribution

The average silicon concentration along the growth interface is also noted to be more uniform at every time step along both directions. At time step 77.03 seconds the average silicon concentration along both $\varphi=0^{\circ}$ and $\varphi=90^{\circ}$ direction was found to be 1.5063 %C, which is the same as that obtained during the TRAMP case along $\varphi=0^{\circ}$ direction at the same time step. Therefore, the silicon evolution in this case is exactly the same as the silicon evolution in the TRAMP case as can be seen in Figure 4-40.

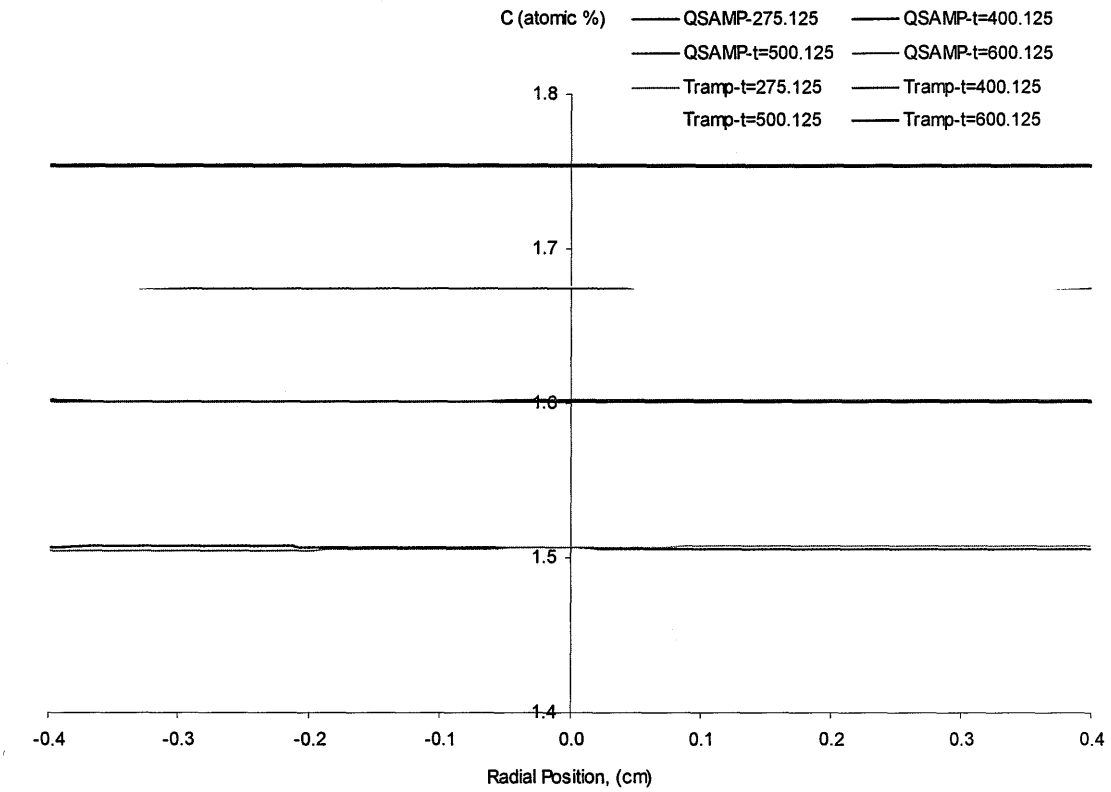

Figure 4- 40: Transient Behavior near the growth interface, along $\varphi=0^{\circ}$, under both the QSAMP and the TRAMP g-jitter growth conditions.

Chapter 5

Conclusion

Based on the performed analysis, a better understanding of crystal growth using the traveling heater method in a space environment has been achieved.

The initial studies suggest that, under terrestrial conditions, convective flow, along with uniform heating, contributes to the complexity of the flow evolutions which leads to non-uniform species distribution along the growth interface. Based on the analysis carried out through this report, it was found that, under a micro-gravity environment, the flow intensity is positively proportional to the micro-gravity intensity with no noticeable effect on the complex 3D flow pattern. Consequently, as the static gravity is decreased, more uniform silicon distribution and slower crystal growth is obtained. The cutoff flow intensity under which convective flow is noticed to have an effect on silicon transportation is 10^{-3} cm/s, which is equivalent to $10^{-3}g_o$ gravitational growth conditions. Furthermore, the complexity of the flow pattern at a higher gravitational growth environment is concluded to have proportional effect on the silicon distribution along the growth interface.

Based on the sinusoidal g-jitter analysis, it was found that the flow intensity within the solvent regime is governed by the overall gravitational intensity, which includes both static gravity and the amplitude of the Fourier component. Therefore, it is valid to conclude that the flow intensity is positively proportional to the overall gravitational intensity. The cutoff gravitational growth conditions effecting silicon transportation was confirmed to be in the range of $10^{-3}g_o$. Therefore, at a microgravity environment lower than $10^{-3}g_o$ silicon transportation is concluded to be purely diffusive.

Furthermore, the frequency was found to be negatively proportional to the flow intensity. As the frequency of the Fourier component is increased, the flow intensity was suppressed. However, at low gravity environment, similar to that encountered in space, flow was determined to be diffusive in nature more than it is convictive. Therefore, further suppression of flow will not have a noticeable effect on the silicon distribution along the growth interface. The frequency effect on the worst case scenario of gravitational growth environment, i.e., $10^{-3}g_o$, can be in the range of 0.2 %C of silicon distribution along the growth interface, which is still considered negligible. Still, usage of high frequency as a stirring agent to suppress the flow and obtain better quality crystal is worth studying further, especially under terrestrial growth conditions where the buoyancy effect due to terrestrial gravity is considered to have a negative effect on homogenous crystal growth.

Further analysis of the real g-jitter effect on crystal growth has proven that flow intensity within the solvent regime is low enough, i.e., within 10^{-5} cm/s, to consider the flow to be purely diffusive. Therefore, the silicon transportation is not effected much. As a result, homogenous silicon distribution along the growth interface is achieved. The obtained data also suggest that the gravitational effect acting parallel to the growth interface has a noticeable effect on the flow pattern. Since the silicon distribution is unaffected by this irregular flow pattern fluctuation, it is valid to conclude that the flow pattern does not affect the silicon transportation at low flow intensity. Furthermore, the combined effect of low flow intensity with the low frequency is also concluded to provide a mean of stirring the solution in order to obtain better silicon distribution. Accordingly, it is valid to conclude that the crystal growth environment in space served us well by providing an ideal growth environment to grow the perfect crystal structure.

So far, based on all of these analyses, it is concluded that FOTTON 12 mission provides very good space environments under which crystal can be grown using the traveling heater method to obtain high quality crystal structures, as desired. Still, the gravitational disturbances experience

on the FOTTON 12 mission is considered to be very low compared to other space environments/missions such as that on board the International Space Station (ISS). Therefore, it is strongly recommended to further study the effect of higher space gravitational effects, acting parallel to the growth interface, on the crystal growth structure.

A continuation of this research is also recommended to further study the possibility of using high frequency on crystal growth under terrestrial conditions since it is more feasible and practical to produce high quality crystal in the earth environment.

Reference

[1] http://www.lenntech.com/periodic-chart-elements/si-en.htm

[2] http://www.lenntech.com/periodic-chart-elements/Ge-en.htm

[3] http://science.uniserve.edu.au/school/quests/semiwq.html

[4] http://en.wikipedia.org/wiki/Semiconductor

[5] http://en.wikipedia.org/wiki/N-type_semiconductor

[6] J. Baumgartl and G. Muller, "Calculation of the effects of magnetic field damping on fluid flow" Eighth European Symp. on Materials and Fluid Sciences in Microgravity, Brussels, Belgium, pp.161-164 (1992).

[7] D.T.J. Hurle, R.W. Series "Handbook of Crystal Growth: 2 Bulk Crystal Growth B: Growth mechanics and dynamic", North-Holland, Amsterdam (1994).

[8] K.Li, B.Q. Li, H.C. de Groh, Effect of Magnetic field on g-jitter induced convection and solute striation during solidification in space, International Journal of Heat and Mass Transfer 46 pp. 4799-4811(2003).

[9] J. P. Garandet, J.I.D. Alexander, S. Corre, J.J. Favier, Composition Variations Induced by g-jitter in Bridgman growth of Sn-Bi alloys in Microgravity, Journal of Crystal Growth 226 pp. 543-554 (2001).

[10] St. Boschert*, A.N. Danilewsky, K.W. Benz, Numerical Simulation of the Influence of the orbiters attitude on the Ug growth of InP: S Crystals from an In Solution during the EURECA-a Flight, Journal of Crystal Growth 205 pp.92-96 (1999).

[11] N.G. Ivanova, A.B. Korsakova, E.M. Smirnova, K.V. Khodosevitchb, V.V. Kalaevb,Yu. N. Makarovc, E. Dornbergerd, J. Virbulisd, W. von Ammond "Analysis of magnetic field effect on 3D melt flow in CZ Si growth" Journal Of Crystal Growth 250 pp.183–188 (2003).

[12] http://en.wikipedia.org/wiki/Czochralski_process

[13] D. Schwabe " Bouyant-thermocapillary and pure thermocapillary convective instabilities in Czochralski systems", Journal of Crystal Growth 237-239 pp. 1849-1853 (2002).

[14] L. J. Liu, K. KaKimoto "3D global analysis of CZ-Si growth in a transverse magnetic field with various crystal growth rates" Journal of Crystal Growth 275 pp.1521-1526 (2005).

[15] B. Pan, D-Y Shang, B.Q. Li, H.C. de Groh. Magnetic field effects on g-jitter induced flow and solute transport, International Journal of Heat and Mass Transfer 45 pp. 125-144 (2002).

[16] Fabrication of bulk semiconductor crystals http://www.ee.byu.edu/cleanroom/everything_wafers.phtml.

[17] B. Pan, D-Y Shang, B.Q. Li, H.C. de Groh. Magnetic field effects on g-jitter induced flow and solute transport, International Journal of Heat and Mass Transfer 45 pp. 125-144 (2002).

[18] M.Z. Saghir, M. Chacha, M.R. Islam, Transient Convection of Te doped GaSb induced by g-jitter, Journal of Crystal Growth 234 pp. 285-295 (2002).

[19] B. Q. Li, g-Jitter induced free convection in a transverse magnetic field, Int. J. Heat Mass Transfer. Vol. 39, No. 14, pp. 2853-2860 (1996).

[20] K.Li, B.Q. Li, H.C. de Groh, Effect of Magnetic field on g-jitter induced convection and solute striation during solidification in space, International Journal of Heat and Mass Transfer 46 pp. 4799-4811 (2003).

[21] K. Li, B.Q. Li and J. Handa, Three-Dimensional Numerical simulation of g-jitter induced convection and solute transport in magnetic fields, School of Mechanical and Materials Engineering, Washington State University, H.C. de Groh NASA Glenn Research Center, International Journal of Numerical Methods for Heat & Fluid Flow Vol. 15 No. 8 pp. 872-893 (2005).

[22] K.Li, B.Q. Li, H.C. de Groh, Effect of Magnetic field on g-jitter induced convection and solute striation during solidification in space, International Journal of Heat and Mass Transfer 46 pp. 4799-4811 (2003).

[23] J. P. Garandet, J.I.D. Alexander, S. Corre, J.J. Favier, Composition Variations Induced by g-jitter in Bridgman growth of Sn-Bi alloys in Microgravity, Journal of Crystal Growth 226 pp. 543-554 (2001).

[24] Float Zone Crystal Growth. http://www.tf.uni-kiel.de/matwis/amat/elmat_en/kap_6/advanced/t6_1_3.html.

[25] "Crystal Growth Descriptions and Definitions" Internet. http://www.geocites.com/shajan89/melt.html.

[26] M Z. Saghir, M. R. Islam, N. Maffei, D. H. Quon. "Three- Dimensional Modeling of Bi12GeO20 using the Float zone technique" Journal of Crystal Growth 193 pp. 623-635 (1998).

[27] C.W. Lan, Effect of Axial Vibration on Vertical Zone-Melting Processing,International Journal of Heat and Mass Transfer 43 pp. 1987-1997 (2000).

[28] X. Ye, B. Tabarrok, D. Walsh. "The Influence of Thermosolutal Convection on CdTe growth by the Traveling Heater Method", Journal of Crystal Growth, 169 pp. 525-530 (1996).

[29] St. Boschert*, A.N. Danilewsky, K.W. Benz, Numerical Simulation of the Influence of the orbiters attitude on the Ug growth of InP: S Crystals from an In Solution during the EURECA-a Flight, Journal of Crystal Growth 205 pp. 92-96 (1999).

[30] T. Jaber, M. Z. Saghir, Usage of Axial and Rotating Magnetic Fields to Process Si0.98Ge0.02 Crystal by the Travelling Heating Method, 5th Joint ASME_JSME, SanDiego, CA. July 30-August 2, 2007.

[31] C.W. Lan, Effect of Axial Vibration on Vertical Zone-Melting Processing,International Journal of Heat and Mass Transfer 43 pp. 1987-1997 (2000).

[32] http://en.wikipedia.org/wiki/Boussinesq_approximation_%28buoyancy%29

[33] R. W. Olesinski, G. J. Abbaschian, "Bulletin of. Alloy Phase Diagrams" 5 edition, p 180 (1984)

[34] FIDAP User Manual, Vol. 8.7.2, 1999.

[35] T. Jaber, M. Z. Saghir, Usage of Axial and Rotating Magnetic Fields to Process Si0.98Ge0.02 Crystal by the Travelling Heating Method, 5th Joint ASME_JSME, SanDiego, CA. July 30-August 2, 2007.

APPENDIX A

Physical Properties

Physical Properties of $Ge_{0.85}Si_{0.15}$		Physical Properties of $Ge_{0.98}Si_{0.02}$		Physical Properties of Ge	
Symbol	**Values**	**Symbol**	**Values**	**Symbol**	**Values**
c_p	$0.04008\,J/g\cdot K$	c_p	$0.04008\,J/g\cdot K$	c_p	$0.0390\,J/g\cdot K$
T_m	1100^oC	T_m	971^oC	T_m	935^oC
α_c	$2.6\times10^{-4}\ cm^2/s$	α_c	$0.52\times10^{-4}\ cm^2/s$	α_c	$1.0\times10^{-4}\ cm^2/s$
α_T	$1.2\times10^{-1}\ cm^2/s$	σ	$2.5\times10^4\ S/cm$	α_T	$1.2\times10^{-1}\ cm^2/s$
β_C	$0.005\quad 1/at\%Si$	β_c	$0.005\quad 1/at\%Si$	β_c	$0.005\quad 1/at\%Si$
β_T	$1.2\times10^{-4}\ 1/^oC$	β_T	$1.01\times10^{-4}\ \ 1/^oC$	β_T	$1.0\times10^{-4}\ \ 1/^oC$
κ	$0.2905W/cm.K$	κ	$0.2559W/cm/K$	κ	$0.25W/cm/K$
μ	$7.4\times10^{-3}\ g/cm\cdot s$	μ	$8.3496\times10^{-3}\ g/cm\cdot s$	μ	$8.5\times10^{-3}\ g/cm\cdot s$
ν	$1.46\times10^{-3}\ cm^2/s$	ν	$1.53192\times10^{-3}\ cm^2/s$	ν	$1.5424\times10^{-3}\ cm^2/s$
ρ	$5.067\ g/cm^3$	ρ	$5.4504\,g/cm^3$	ρ	$5.51\,g/cm^3$
L_f	$39\ cal/g$				

Table A- 1: Physical properties of the Silicon Germanium

APPENDIX B

B.1 Sinusoidal Gravity Model:

In a typical microgravity environment, the residual acceleration experienced by the spacecraft is composed of a steady component and time-dependent components acting in 3D. This realistic g-jitter model can be expressed as:

$$g = g_i(t) = g_{io} + \sum_{j=1}^{n} (b_i^j \cos 2\pi f_i^j t + c_i^j \sin 2\pi f_i^j t) \tag{B.1}$$

Where, i is the direction of the applied gravity, i.e., x, y and z directions, and j is the number of components per direction.

However, to study the effect of each variable in this large equation, a more simplified sinusoidal gravity of the form is used:

$$g = g(t) = g_1 + A\sin(2\pi ft) \tag{B.2}$$

Where, g1 is the static micro-gravitational force, A is the amplitude of the damping gravity force, f is the damping frequency.

The following non-dimentionalized variables are used:

$$g = g^* g_o, \quad t = \tau D / u_o, \quad f = F u_o / D \tag{B.3}$$

Where go is the terrestrial gravitational acceleration, and τ is the non-dimensional time and F is the non dimensional frequency.

The non-dimensional sinusoidal gravity to be studied can be expressed as:

$$g^* = g(t) = \frac{g_1}{g_o} + \frac{A}{g_o}\sin\left(2\pi\left(\frac{Fu_o}{D}\right)\left(\frac{\tau D}{u_o}\right)\right) \tag{B.4}$$

This can be further simplified to:

$$g^* = g^*(t) = g_1^* + A^*\sin(2\pi F\tau) \tag{B.5}$$

The main influence of this variable can be captured through the Grashof number:

$$Gr = \frac{\beta_t \Delta T g^* D^3 \rho^2}{\mu^2} \tag{B.6}$$

Note; the convective terms represented by the gravitational force couples the energy and the transport equations. Since the g-jitter forces have a very weak effect on the Navier-Stokes equations, the energy equation and the solute transport equations are decoupled. Therefore, one would not expect the Silicon concentration distribution to be a function of the thermal distribution. To avoid decoupling these equations in order to take the gravitational fluctuation into consideration, the g-jitter force will be imposed on the z-momentum equation as a separate additional force in the case of synthetic gravity and along the three axes in the case of real g-jitter. This is possible to implement through FIDAP software. A body force FORTRAN sub program is included in Appendix D representing this body force.

B.1 Realistic Gravity Model – G-Jitter

The realistic g-jitter model is extracted from collected data. In this thesis, two sets of extracted data will be utilized, the QSAMP and TRAMP case. For both sets, the general description of the data can be expressed in the following manner:

$$g = g_i(t) = g_{io} + \sum_{j=1}^{n} (b_i^j \cos 2\pi f_i^j t + c_i^j \sin 2\pi f_i^j t) \quad \text{(B.1)}$$

Where the Coefficients for each case is recorded as follows:

B.1.1 Case 1: TRAMP

i = 1 (x-direction)

j	g_{xo} (10^{-6}m/s^2)	b_x^j (10^{-6}m/s^2)	c_x^j (10^{-6}m/s^2)	f_x^j (10^{-3}Hz)
1	-3.6615	-24.896	30.786	1.645209

i = 2 (y-direction)

j	g_{yo} (10^{-6}m/s^2)	b_y^j (10^{-6}m/s^2)	c_y^j (10^{-6}m/s^2)	f_y^j (10^{-3}Hz)
1	-116.65	1.5392	0.42332	1.157556
2	---	3.3976	-7.5033	2.51535
3	---	4.1744	1.4193	1.872925
4	---	-4.7073	-2.6550	2.237846
5	---	-0.96563	-1.4247	3.281500

i = 3 (z-direction)

j	g_{zo} (10^{-6}m/s^2)	b_z^j (10^{-6}m/s^2)	c_z^j (10^{-6}m/s^2)	f_z^j (10^{-3}Hz)
1	16.508	5.5583	2.8422	1.643534
2	---	-0.45562	-0.70390	1.870828
3	---	-1.5791	-0.094072	2.073682
4	---	-2.8356	1.0229	3.290399
5	---	-0.91597	-0.27967	4.149568

Table B- 1: TRAMP gravitational Coefficients

B.1.2 Case 2: QSAMP

i = 1 (x-direction)

j	g_{xo} (10^{-6}m/s^2)	b_x^j (10^{-6}m/s^2)	c_x^j (10^{-6}m/s^2)	f_x^j (10^{-3}Hz)
1	0.0	23.009	0.0	2.234
2	---	0.746	0.0	2.436
3	---	1.707	0.0	2.656
4	---	1.265	0.0	3.397

i = 2 (y-direction)

j	g_{yo} (10^{-6}m/s^2)	b_y^j (10^{-6}m/s^2)	c_y^j (10^{-6}m/s^2)	f_y^j (10^{-3}Hz)
1	0.0	1.381	0.0	2.232
2	---	0.153	0.0	2.450
3	---	0.478	0.0	2.638
4	---	0.661	0.0	2.816
5	---	0.440	0.0	2.998
6	---	0.131	0.0	3.182

i = 3 (z-direction)

j	g_{zo} (10^{-6}m/s^2)	b_z^j (10^{-6}m/s^2)	c_z^j (10^{-6}m/s^2)	f_z^j (10^{-3}Hz)
1	0.0	1.249	0.0	2.234
2	---	0.091	0.0	2.664

Table B- 2: QSAMP gravitational Coefficients

APPENDIX C

Non-Dimensionalization

C.1 Navier-Stokes Equations

r - component

The dimensional form of r-direction momentum equation is:

$$\rho\left[\frac{\partial u}{\partial t}+u\frac{\partial u}{\partial r}+\frac{v}{r}\frac{\partial u}{\partial \varphi}+w\frac{\partial u}{\partial z}-\frac{v^2}{r}\right]=-\frac{\partial p}{\partial r}+\mu\left[\frac{1}{r}\frac{\partial}{\partial r}\left(\frac{\partial u}{\partial r}\right)+\frac{1}{r^2}\frac{\partial^2 u}{\partial \varphi^2}+\frac{\partial^2 u}{\partial z^2}\right]$$

$$\rho\left[\frac{\partial u}{\partial t}+u\frac{\partial u}{\partial r}+\frac{v}{r}\frac{\partial u}{\partial \varphi}+w\frac{\partial u}{\partial z}-\frac{v^2}{r}\right]=-\frac{\partial p}{\partial r}+\mu\left[\frac{1}{r}\frac{\partial}{\partial r}\left(\frac{\partial u}{\partial r}\right)+\frac{1}{r^2}\frac{\partial^2 u}{\partial \varphi^2}+\frac{\partial^2 u}{\partial z^2}\right] \tag{C.1}$$

The following non-dimensionalized variables are placed into the equation.

$$r=RD,\ z=ZD,\ u=Uu_o,\ v=Vu_o,\ w=Wu_o,\ T-T_o=\Delta T\theta,\ c-c_o=\Delta cC\ \ p=\frac{P\mu u_o}{D},\ \text{and}\ \ \omega=\frac{\omega^* u_o}{D},$$

$$t=\frac{\tau D}{u_o}$$

Substituting the variables inside the equation above:

$$\rho\left[\frac{\partial(Uu_o)}{\partial\left(\frac{\tau D}{u_o}\right)}+Uu_o\frac{\partial(Uu_o)}{\partial(RD)}+\frac{Vu_o}{RD}\frac{\partial(Uu_o)}{\partial\varphi}+Wu_o\frac{\partial(Uu_o)}{\partial(ZD)}-\frac{(Vu_o)^2}{(RD)}\right]=-\frac{\partial\left(\frac{P\mu u_o}{D}\right)}{\partial(RD)}+$$

$$\mu\left[\frac{1}{RD}\frac{\partial}{\partial(RD)}\left(\frac{\partial(Uu_o)}{\partial(RD)}\right)+\frac{1}{(RD)^2}\frac{\partial^2(Uu_o)}{\partial\varphi^2}+\frac{\partial^2(Uu_o)}{\partial(ZD)^2}\right] \tag{C.2}$$

Dividing the equation by $\frac{\mu u_o}{D^2}$, a factor chosen to further simplify the equation gives:

$$\frac{\rho u_o^2}{D}\left[\frac{\partial U}{\partial \tau}+U\frac{\partial U}{\partial R}+\frac{V}{R}\frac{\partial U}{\partial \varphi}+W\frac{\partial U}{\partial Z}-\frac{V^2}{R}\right]\cdot\frac{D^2}{\mu u_o}=$$

$$-\frac{\mu u_o}{D^2}\frac{\partial P}{\partial R}\cdot\frac{D^2}{\mu u_o}+\frac{\mu u_o}{D^2}\left[\frac{1}{R}\frac{\partial}{\partial R}\left(\frac{\partial U}{\partial R}\right)+\frac{1}{R^2}\frac{\partial^2 U}{\partial \varphi^2}+\frac{\partial^2 U}{\partial Z^2}\right]\cdot\frac{D^2}{\mu u_o} \tag{C.3}$$

This Further simplifies to:

$$\frac{\rho u_o D}{\mu}\left[\frac{\partial U}{\partial \tau}+U\frac{\partial U}{\partial R}+\frac{V}{R}\frac{\partial U}{\partial \varphi}+W\frac{\partial U}{\partial Z}-\frac{V^2}{R}\right]=-\frac{\partial P}{\partial R}+\left[\frac{1}{R}\frac{\partial}{\partial R}\left(\frac{\partial U}{\partial R}\right)+\frac{1}{R^2}\frac{\partial^2 U}{\partial \varphi^2}+\frac{\partial^2 U}{\partial Z^2}\right] \tag{C.4}$$

The non-dimensionalized form of the *r*-component of the Navier-Stokes equation

$$\mathrm{Re}\left[\frac{\partial U}{\partial \tau}+U\frac{\partial U}{\partial R}+\frac{V}{R}\frac{\partial U}{\partial \varphi}+W\frac{\partial U}{\partial Z}-\frac{V^2}{R}\right]=-\frac{\partial P}{\partial R}+\left[\frac{1}{R}\frac{\partial}{\partial R}\left(\frac{\partial U}{\partial R}\right)+\frac{1}{R^2}\frac{\partial^2 U}{\partial \varphi^2}+\frac{\partial^2 U}{\partial Z^2}\right] \tag{C.5}$$

φ - component

The dimensional form of φ-direction momentum equation is:

$$\rho\left[\frac{\partial v}{\partial t}+u\frac{\partial v}{\partial r}+\frac{v}{r}\frac{\partial v}{\partial \varphi}+w\frac{\partial v}{\partial z}+\frac{uv}{r}\right]=-\frac{1}{r}\frac{\partial p}{\partial \varphi}+\mu\left[\frac{1}{r}\frac{\partial}{\partial r}\left(\frac{\partial v}{\partial r}\right)+\frac{1}{r^2}\frac{\partial^2 v}{\partial \varphi^2}+\frac{\partial^2 v}{\partial z^2}\right] \tag{C.6}$$

Substituting the dimensionless variables inside the equation C.6:

$$\rho\left[\frac{\partial(Vu_o)}{\partial\left(\frac{\tau D}{u_o}\right)}+(Uu_o)\frac{\partial(Vu_o)}{\partial(RD)}+\frac{(Vu_o)}{(RD)}\frac{\partial(Vu_o)}{\partial\varphi}+(Wu_o)\frac{\partial(Vu_o)}{\partial(ZD)}+\frac{(Uu_oVu_o)}{(RD)}\right]=$$

$$-\frac{1}{(RD)}\frac{\partial\left(\frac{P\mu u_o}{D}\right)}{\partial\varphi}+\mu\left[\frac{1}{(RD)}\frac{\partial}{\partial(RD)}\left(\frac{\partial(Vu_o)}{\partial(RD)}\right)+\frac{1}{(RD)^2}\frac{\partial^2(Vu_o)}{\partial\varphi^2}+\frac{\partial^2(Vu_o)}{\partial(ZD)^2}\right] \tag{C.7}$$

and then dividing by $\frac{\mu u_o}{D^2}$:

$$\frac{\rho u_o^2}{D}\left[\frac{\partial V}{\partial\tau}+U\frac{\partial V}{\partial R}+\frac{V}{R}\frac{\partial V}{\partial\varphi}+W\frac{\partial V}{\partial Z}+\frac{UV}{R}\right]\cdot\frac{D^2}{\mu u_o}=-\frac{\mu u_o}{D^2}\frac{\partial P}{\partial\varphi}\cdot\frac{D^2}{\mu u_0}+$$

$$\frac{\mu u_o}{D^2}\left[\frac{1}{R}\frac{\partial}{\partial R}\left(\frac{\partial V}{\partial R}\right)+\frac{1}{R^2}\frac{\partial^2 V}{\partial\varphi^2}+\frac{\partial^2 V}{\partial Z^2}\right] \tag{C.8}$$

Now by organizing all common factors we get

$$\frac{\rho u_o D}{\mu}\left[\frac{\partial V}{\partial\tau}+U\frac{\partial V}{\partial R}+\frac{V}{R}\frac{\partial V}{\partial\varphi}+W\frac{\partial V}{\partial Z}+\frac{UV}{R}\right]=-\frac{1}{R}\frac{\partial P}{\partial\varphi}+\left[\frac{1}{R}\frac{\partial}{\partial R}\left(\frac{\partial V}{\partial R}\right)+\frac{1}{R^2}\frac{\partial^2 V}{\partial\varphi^2}+\frac{\partial^2 V}{\partial Z^2}\right] \tag{C.9}$$

The non-dimensionalized form of the φ-component of the Navier-Stokes equation

$$\mathrm{Re}\left[\frac{\partial V}{\partial\tau}+U\frac{\partial V}{\partial R}+\frac{V}{R}\frac{\partial V}{\partial\varphi}+W\frac{\partial V}{\partial Z}+\frac{UV}{R}\right]=-\frac{1}{R}\frac{\partial P}{\partial\varphi}+\left[\frac{1}{R}\frac{\partial}{\partial R}\left(\frac{\partial V}{\partial R}\right)+\frac{1}{R^2}\frac{\partial^2 V}{\partial\varphi^2}+\frac{\partial^2 V}{\partial Z^2}\right] \tag{C.9}$$

z - component

The dimensional form of z-direction momentum equation is:

(C.11)

$$\rho\left[\frac{\partial w}{\partial t}+u\frac{\partial w}{\partial r}+\frac{v}{r}\frac{\partial w}{\partial \varphi}+w\frac{\partial w}{\partial z}\right]=-\frac{\partial p}{\partial z}+\mu\left[\frac{1}{r}\frac{\partial}{\partial r}\left(\frac{\partial w}{\partial r}\right)+\frac{1}{r^2}\frac{\partial^2 w}{\partial \varphi^2}+\frac{\partial^2 w}{\partial z^2}\right]+$$

$$\rho(g)\left[\beta_t(T-T_0)-\beta_C(c-c_0)\right] \tag{C.12}$$

$$\frac{\rho u_o^2}{D}\left[\frac{\partial W}{\partial \tau}+U\frac{\partial W}{\partial R}+\frac{V}{R}\frac{\partial W}{\partial \varphi}+W\frac{\partial W}{\partial Z}\right]\cdot\frac{D^2}{\mu u_o}=-\frac{\mu u_o}{D^2}\frac{\partial P}{\partial Z}\cdot\frac{D^2}{\mu u_o}+$$

$$\frac{\mu u_o}{D^2}\left[\frac{1}{R}\frac{\partial}{\partial R}\left(\frac{\partial W}{\partial R}\right)+\frac{1}{R^2}\frac{\partial^2 W}{\partial \varphi^2}+\frac{\partial^2 W}{\partial Z^2}\right]\cdot\frac{D^2}{\mu u_o}+\frac{\rho g\left[\beta_t\Delta T\theta-\beta_C\Delta cC\right]}{\frac{\mu u_o}{D^2}} \tag{C.13}$$

Now by organizing all the common factors we get

$$\frac{\rho u_o D}{\mu}\left[\frac{\partial W}{\partial \tau}+U\frac{\partial W}{\partial R}+\frac{V}{R}\frac{\partial W}{\partial \varphi}+W\frac{\partial W}{\partial Z}\right]=-\frac{\partial P}{\partial Z}+$$

$$\left[\frac{1}{R}\frac{\partial}{\partial R}\left(\frac{\partial W}{\partial R}\right)+\frac{1}{R^2}\frac{\partial^2 W}{\partial \varphi^2}+\frac{\partial^2 W}{\partial Z^2}\right]+\frac{\rho g D^2}{\mu u_o}\left[\beta_t\Delta T\theta-\beta_C\Delta cC\right] \tag{C.14}$$

The non-dimensionalized form of the *z*-component of the Navier-Stokes equation.

$$\mathrm{Re}\left[\frac{\partial W}{\partial \tau}+U\frac{\partial W}{\partial R}+\frac{V}{R}\frac{\partial W}{\partial \varphi}+W\frac{\partial W}{\partial Z}\right]=-\frac{\partial P}{\partial Z}+\left[\frac{1}{R}\frac{\partial}{\partial R}\left(\frac{\partial W}{\partial R}\right)+\frac{1}{R^2}\frac{\partial^2 W}{\partial \varphi^2}+\frac{\partial^2 W}{\partial Z^2}\right]$$

$$+\frac{Gr_T}{\mathrm{Re}}\theta-\frac{Gr_c}{\mathrm{Re}}C \tag{C.15}$$

C.2 Energy Equation

$$\frac{\partial T}{\partial t}+u\frac{\partial T}{\partial r}+\frac{v}{r}\frac{\partial T}{\partial \varphi}+w\frac{\partial T}{\partial z}=\frac{\kappa}{\rho c_p}\left(\frac{1}{r}\frac{\partial T}{\partial r}+\frac{\partial^2 T}{\partial r^2}+\frac{1}{r^2}\frac{\partial^2 T}{\partial \varphi^2}+\frac{\partial^2 T}{\partial z^2}\right) \tag{C.16}$$

Substituting the dimensionless variables inside the equation above:

$$\rho c_p \left[\frac{\partial(\Delta T\theta + T_o)}{\partial\left(\frac{\tau D}{u_o}\right)} + Uu_o \frac{\partial(\Delta T\theta + T_o)}{\partial(RD)} + \frac{Vu_o}{(RD)} \frac{\partial(\Delta T\theta + T_o)}{\partial\varphi} + Wu_o \frac{\partial(\Delta T\theta + T_o)}{\partial(ZD)} \right] =$$

$$\kappa \left[\frac{1}{RD} \frac{\partial(\Delta T\theta + T_o)}{\partial(RD)} + \frac{\partial^2(\Delta T\theta + T_o)}{\partial(RD)^2} + \frac{1}{(RD)^2} \frac{\partial^2(\Delta T\theta + T_o)}{\partial\varphi^2} + \frac{\partial^2(\Delta T\theta + T_o)}{\partial(ZD)^2} \right] \tag{C.17}$$

Simplifying gives:

$$\mathrm{Re}\,\mathrm{Pr}\left[\frac{\partial\theta}{\partial\tau} + U\frac{\partial\theta}{\partial R} + \frac{V}{R}\frac{\partial\theta}{\partial\varphi} + W\frac{\partial\theta}{\partial Z} \right] = \left[\frac{1}{R}\frac{\partial\theta}{\partial R} + \frac{\partial^2\theta}{\partial R^2} + \frac{1}{R^2}\frac{\partial^2\theta}{\partial\varphi^2} + \frac{\partial^2\theta}{\partial Z^2} \right] \tag{C.18}$$

C.3 Continuity Equation

$$\frac{\partial\rho}{\partial t} + \frac{1}{r}\frac{\partial}{\partial r}(\rho r u) + \frac{1}{r}\frac{\partial(\rho v)}{\partial\varphi} + \frac{\partial(\rho w)}{\partial z} = 0 \tag{C.19}$$

Substituting the dimensionless variables inside the equation above:

$$\frac{\partial\rho}{\partial\left(\frac{\tau D}{u_o}\right)} + \frac{1}{(RD)}\frac{\partial}{\partial(RD)}(RDUu_o\rho) + \frac{1}{(RD)}\frac{\partial(Vu_o\rho)}{\partial\varphi} + \frac{\partial(Wu_o\rho)}{\partial(ZD)} = 0 \tag{C.20}$$

Simplifying gives:

$$\frac{\partial\rho}{\partial\tau} + \frac{1}{R}\frac{\partial}{\partial R}(RU\rho) + \frac{1}{R}\frac{\partial(V\rho)}{\partial\varphi} + \frac{\partial(W\rho)}{\partial Z} = 0 \tag{C.21}$$

C.4 Solute Equation

$$\frac{\partial c}{\partial t} + u\frac{\partial c}{\partial r} + \frac{v}{r}\frac{\partial c}{\partial\varphi} + w\frac{\partial c}{\partial z} = \alpha_C\left(\frac{1}{r}\frac{\partial}{\partial r}\left(r\frac{\partial c}{\partial r} \right) + \frac{1}{r^2}\frac{\partial^2 c}{\partial\varphi^2} + \frac{\partial^2 c}{\partial z^2} \right) \tag{C.23}$$

Substituting the dimensionless variables inside the equation above:

$$\rho\left[\frac{\partial(C\Delta c+c_o)}{\partial\left(\frac{\tau D}{u_o}\right)}+Uu_o\frac{\partial(C\Delta c+c_o)}{\partial(RD)}+\frac{Vu_0}{(RD)}\frac{\partial(C\Delta c+c_o)}{\partial\varphi}+Wu_o\frac{\partial(C\Delta c+c_o)}{\partial(ZD)}\right]=$$

$$\rho\alpha_c\left[\frac{1}{(RD)}\frac{\partial}{\partial(RD)}\left((RD)\frac{\partial(C\Delta c+c_o)}{\partial(RD)}\right)+\frac{1}{(RD)^2}\frac{\partial^2(C\Delta c+c_o)}{\partial\varphi}+\frac{\partial^2(C\Delta c+c_o)}{\partial(ZD)^2}\right] \qquad \text{(C.24)}$$

Simplifying gives:

$$\mathrm{Re}\left[\frac{\partial C}{\partial\tau}+U\frac{\partial C}{\partial R}+\frac{V}{R}\frac{\partial C}{\partial\varphi}+W\frac{\partial C}{\partial Z}\right]=\frac{1}{Sc}\left[\frac{1}{R}\frac{\partial}{\partial R}(R\frac{\partial C}{\partial R})+\frac{1}{R^2}\frac{\partial^2 C}{\partial\varphi^2}+\frac{\partial^2 C}{\partial Z^2}\right] \qquad \text{(C.25)}$$

Note, during the static gravity analysis all the time dependent variable are set to zero, allowing steady state analysis to be performed.

Appendix D

D.1 Input File for the Terrestrial and Static Microgravity

The input file is revised regarding to each case, as follows:

1. Terrestrial under non-uniform heating case. In this case the gravity is equal to go
2. Microgravity under non-uniform heating case. In this case the gravity is varied from go to 10-3go, 10-4go, 10-5go, and 10-6go

FDREAD Input File

```
/ ****************************************************************
/ Disclaimer: This file was written by GAMBIT and contains
/ all the continuum and boundary entities and coordinate systems
/ defined in GAMBIT. Additionally, some frequently used FIPREP
/ commands are added. Modify/Add/Uncommment any necessary commands.
/ Refer to FIPREP documentation for complete listing of commands.
/ ****************************************************************
/
/          CONVERSION OF NEUTRAL FILE TO FIDAP Database
/
FICONV( NEUTRAL )
INPUT( FILE="60x240.FDNEUT" )
OUTPUT( DELETE )
END
/
TITLE
60x240-Microggravity-NONU
/
FIPREP
/
/          PROBLEM SETUP
/
PROBLEM (3-D, NONLINEAR, BUOYANCY, FREE, BUOYANCY =1, BUOYANCY = 2)
EXECUTION( NEWJOB )
PRINTOUT( NONE )
DATAPRINT( CONTROL )
/
/          CONTINUUM ENTITIES
/
RENUMBER( PROFILE )
ENTITY ( NAME = "source", SOLID, PROPERTY = "source" )
ENTITY ( NAME = "solvent", FLUID, PROPERTY = "solvent", SPECIES = 1,
MDIFF = 3, MEXP = 3 )
ENTITY ( NAME = "substrate", FLUID, PROPERTY = "substrate", SPECIES = 1,
MDIFF = 3 )
/
```

```
/          BOUNDARY ENTITIES
/
ENTITY ( NAME = "top", PLOT, ATTACH = "source" )
ENTITY ( NAME = "outflow", PLOT, ATTACH = "solvent" )
ENTITY ( NAME = "inflow", MELT, ATTACH = "solvent", NATTACH =
"substrate", MSPHT = "solvent", DEPTH = -1, SPECIES = 1, M1LIQU =
"solvent" )
ENTITY ( NAME = "bottom", SURFACE, SPINE, STRAIGHT, DEPTH = 0, CONTINUE,
ATTACH = "substrate" )
ENTITY ( NAME = "profile1", PLOT )
ENTITY ( NAME = "profile2", PLOT )
ENTITY ( NAME = "profile3", PLOT )
ENTITY (NAME = "interface", PLOT, ATTACH = "solvent" )
ENTITY( NAME = "inferfacedge", PLOT, ATTACH = "solvent" )
/
LIQUIDUS( SET = "solvent", CONSTANT = 12.56, TEMPERATURE )
/          LOCAL COORDINATE SYSTEMS DEFINED
/
/
/          SOLUTION PARAMETERS
/
SOLUTION( SEGREGATED = 450 )
PRESSURE( MIXED = 1.E-8, DISCONTINUOUS )
/RELAX( HYBRID )
OPTIONS( UPWINDING )
UPWIND( 1STO )
/
/          MATERIAL PROPERTIES
/
/ Partial list of Material Properties data
/
DENSITY( SET = "source", CONSTANT = 233, TYP2, TEMPERATURE, SPECIES =
1 )
VISCOSITY( SET = "source", CONSTANT = 1 )
CONDUCTIVITY( SET = "source", CONSTANT = 1 )
SPECIFICHEAT( SET = "source", CONSTANT = 2.25E-2 )
VOLUMEXPANSION( SET = "source", CONSTANT = 1, TEMPERATURE )
/
DENSITY( SET = "solvent", CONSTANT = 450, TYP2, TEMPERATURE, SPECIES =
1 )
VISCOSITY( SET = "solvent", CONSTANT = 1 )
CONDUCTIVITY( SET = "solvent", CONSTANT = 1 )
SPECIFICHEAT( SET = "solvent", CONSTANT = 7E-3,LATENT = 2.23, TMELT =
36 )
VOLUMEXPANSION( SET = "solvent", CONSTANT = 1, TEMPERATURE )
GRAVITY( MAGNITUDE = 1.0 )
/
VOLUMEXPANSION( SET =3, CONSTANT = 42, SPECIES = 1 )
DIFFUSIVITY( SET = 3, CONSTANT = 1.587E-4, SPECIES = 1 )
/
/DENSITY( SET = "substrate", CONSTANT = 409, TYP2, TEMPERATURE, SPECIES
= 1 )
VISCOSITY( SET = "substrate", CONSTANT = 1 )
CONDUCTIVITY( SET = "substrate", CONSTANT = 1 )
SPECIFICHEAT( SET = "substrate", CONSTANT = 7E-3 )
VOLUMEXPANSION( SET = "substrate", CONSTANT = 1, TEMPERATURE )
/
```

```
/          INITIAL AND BOUNDARY CONDITIONS
/
/ICNODE( , CONSTANT = 0, ALL )
/
/BODYFORCE( ENTITY = "solvent", LORENTZ = 2, VXB = 1, FZC =
1.749635531 )
/BCNODE( SPECIES = 2, CONSTANT = 0, ENTITY = "solvent" )
/BCNODE( SPECIES = 2, CONSTANT = 0, ENTITY = "source" )
/BCNODE( SPECIES = 2, CONSTANT = 0, ENTITY = "substrate" )
/
/
/
BCNODE( SURFACE,ZERO, ENTITY = "inferfacedge" )
BCNODE( SURFACE, ZERO, ENTITY = "bottom" )
/
BCNODE( SPECIES = 1, CONSTANT = 0.15, ENTITY = "source" )
BCNODE( SPECIES = 1, CONSTANT = 0.02, ENTITY = "inflow" )
BCNODE( SPECIES = 1, CONSTANT = 0.15, ENTITY = "outflow")
/
BCNODE( VELOCITY, CONSTANT = 0, ENTITY = "source" )
BCNODE( VELOCITY, CONSTANT = 0, ENTITY = "substrate" )
/
BCNODE( COORDINATE, ENTITY = "inferfacedge" )
BCSYSTEM( SET = 1, EDGE )
/
BCNODE( VELOCITY, CONSTANT = 0, ENTITY = "top" )
BCNODE( VELOCITY, CONSTANT = 0, ENTITY = "bottom" )
BCNODE( VELOCITY, CONSTANT = 0, ENTITY = "profile1" )
BCNODE( VELOCITY, CONSTANT = 0, ENTITY = "profile2" )
BCNODE( VELOCITY, CONSTANT = 0, ENTITY = "profile3" )
/
BCNODE( TEMPERATURE, POLYNOMIAL = 10, ENTITY = "profile1" )
-171.491674619836000  3.75234521575985 1 0 0 -0.000000000000028217 0 1
0 -23.468172284192400 0 0 1 14.0800946182358 2 0 0 -42.240284 0 2 0
784.323802803643000 0 0 2 -825.939526461064000 0 0 3
338.295844875043000 0 0 4  -62.326428754429800 0 0 5 4.325223592473780
0 0 6
BCNODE( TEMPERATURE, POLYNOMIAL = 10, ENTITY = "profile2" )
-171.491674619836000  3.75234521575985 1 0 0 -0.000000000000028217 0 1
0 -23.468172284192400 0 0 1 14.0800946182358 2 0 0 -42.240284 0 2 0
784.323802803643000 0 0 2 -825.939526461064000 0 0 3
338.295844875043000 0 0 4  -62.326428754429800 0 0 5 4.325223592473780
0 0 6
BCNODE( TEMPERATURE, POLYNOMIAL = 10, ENTITY = "profile3" )
-171.491674619836000  3.75234521575985 1 0 0 -0.000000000000028217 0 1
0 -23.468172284192400 0 0 1 14.0800946182358 2 0 0 -42.240284 0 2 0
784.323802803643000 0 0 2 -825.939526461064000 0 0 3
338.295844875043000 0 0 4  -62.326428754429800 0 0 5 4.325223592473780
0 0 6
/
END
/
CREATE( FIPREP,DELETE )
PARAMETER( LIST )
CREATE( FISOLV )
/RUN( FISOLV, FOREGROUND )
```

D.2 Input File for the Transient g-jitter Cases (Sinusoidal and Real g-jitters)

This input file was not revised as it always points to a SUBROUTINE, which included the varying g-jitter variable. The FIDAP input file was set as:

```
/ ****************************************************************
/ Disclaimer: This file was written by GAMBIT and contains
/ all the continuum and boundary entities and coordinate systems
/ defined in GAMBIT. Additionally, some frequently used FIPREP
/ commands are added. Modify/Add/Uncommment any necessary commands.
/ Refer to FIPREP documentation for complete listing of commands.
/ ****************************************************************
/
/          CONVERSION OF NEUTRAL FILE TO FIDAP Database
/
FICONV( NEUTRAL )
INPUT( FILE="20(5)X40.FDNEUT" )
OUTPUT( DELETE )
END
/
TITLE
60x240-Microggravity-NONU
/
FIPREP
/
/          PROBLEM SETUP
/
PROBLEM (3-D, NONLINEAR, ENERGY, FREE, SPECIES = 1, SPECIES = 2,
TRANSIENT )
TIMEINTEGRATION (BACKWARD, DT=0.028, FIXED, NSTEPS=4000, TEND=112 )
EXECUTION( NEWJOB )
PRINTOUT( NONE )
DATAPRINT( CONTROL )
/
/          CONTINUUM ENTITIES
/
RENUMBER( PROFILE )
ENTITY ( NAME = "source", SOLID, PROPERTY = "source" )
ENTITY ( NAME = "solvent", FLUID, PROPERTY = "solvent", SPECIES = 1,
MDIFF = 3, MEXP = 3 )
ENTITY ( NAME = "substrate", FLUID, PROPERTY = "substrate", SPECIES = 1,
MDIFF = 3 )
/
/          BOUNDARY ENTITIES
/
ENTITY ( NAME = "top", PLOT, ATTACH = "source" )
ENTITY ( NAME = "outflow", PLOT, ATTACH = "solvent" )
ENTITY ( NAME = "inflow", MELT, ATTACH = "solvent", NATTACH =
"substrate", MSPHT = "solvent", DEPTH = -1, SPECIES = 1, M1LIQU =
"solvent" )
```

```
ENTITY ( NAME = "bottom", SURFACE, SPINE, STRAIGHT, DEPTH = 0, CONTINUE,
ATTACH = "substrate" )
ENTITY ( NAME = "profile1", PLOT )
ENTITY ( NAME = "profile2", PLOT )
ENTITY ( NAME = "profile3", PLOT )
ENTITY (NAME = "interface", PLOT, ATTACH = "solvent" )
ENTITY( NAME = "inferfacedge", PLOT, ATTACH = "solvent" )
/
LIQUIDUS( SET = "solvent", CONSTANT = 12.56, TEMPERATURE )
/          LOCAL COORDINATE SYSTEMS DEFINED
/
/
/          SOLUTION PARAMETERS
/
SOLUTION( SEGREGATED = 200 )
PRESSURE( MIXED = 1.E-8, DISCONTINUOUS )
/RELAX( HYBRID )
OPTIONS( UPWINDING )
UPWIND( 1STO )
/
/          MATERIAL PROPERTIES
/
/ Partial list of Material Properties data
/
DENSITY( SET = "source", CONSTANT = 233, TYP2, TEMPERATURE, SPECIES =
1 )
VISCOSITY( SET = "source", CONSTANT = 1 )
CONDUCTIVITY( SET = "source", CONSTANT = 1 )
SPECIFICHEAT( SET = "source", CONSTANT = 2.25E-2 )
VOLUMEXPANSION( SET = "source", CONSTANT = 1, TEMPERATURE )
/
DENSITY( SET = "solvent", CONSTANT = 450, TYP2, TEMPERATURE, SPECIES =
1 )
VISCOSITY( SET = "solvent", CONSTANT = 1 )
CONDUCTIVITY( SET = "solvent", CONSTANT = 1 )
SPECIFICHEAT( SET = "solvent", CONSTANT = 7E-3,LATENT = 2.23, TMELT =
36 )
VOLUMEXPANSION( SET = "solvent", CONSTANT = 1, TEMPERATURE )
/GRAVITY( MAGNITUDE = 0.0001 )
/
VOLUMEXPANSION( SET =3, CONSTANT = 42, SPECIES = 1 )
DIFFUSIVITY( SET = 3, CONSTANT = 1.587E-4, SPECIES = 1 )
/
/DENSITY( SET = "substrate", CONSTANT = 409, TYP2, TEMPERATURE, SPECIES
= 1 )
VISCOSITY( SET = "substrate", CONSTANT = 1 )
CONDUCTIVITY( SET = "substrate", CONSTANT = 1 )
SPECIFICHEAT( SET = "substrate", CONSTANT = 7E-3 )
VOLUMEXPANSION( SET = "substrate", CONSTANT = 1, TEMPERATURE )
/
/          INITIAL AND BOUNDARY CONDITIONS
/
/ICNODE( , CONSTANT = 0, ALL )
/
BODYFORCE( ENTITY = "solvent", SUBROUTINE )
BCNODE( SPECIES = 2, CONSTANT = 0, ENTITY = "solvent" )
BCNODE( SPECIES = 2, CONSTANT = 0, ENTITY = "source" )
```

```
BCNODE( SPECIES = 2, CONSTANT = 0, ENTITY = "substrate" )
/
/
/
BCNODE( SURFACE,ZERO, ENTITY = "inferfacedge" )
BCNODE( SURFACE, ZERO, ENTITY = "bottom" )
/
BCNODE( SPECIES = 1, CONSTANT = 0.15, ENTITY = "source" )
BCNODE( SPECIES = 1, CONSTANT = 0.02, ENTITY = "inflow" )
BCNODE( SPECIES = 1, CONSTANT = 0.15, ENTITY = "outflow")
/
BCNODE( VELOCITY, CONSTANT = 0, ENTITY = "source" )
BCNODE( VELOCITY, CONSTANT = 0, ENTITY = "substrate" )
/
BCNODE( COORDINATE, ENTITY = "inferfacedge" )
BCSYSTEM( SET = 1, EDGE )
/
BCNODE( VELOCITY, CONSTANT = 0, ENTITY = "top" )
BCNODE( VELOCITY, CONSTANT = 0, ENTITY = "bottom" )
BCNODE( VELOCITY, CONSTANT = 0, ENTITY = "profile1" )
BCNODE( VELOCITY, CONSTANT = 0, ENTITY = "profile2" )
BCNODE( VELOCITY, CONSTANT = 0, ENTITY = "profile3" )
/
BCNODE( TEMPERATURE, POLYNOMIAL = 10, ENTITY = "profile1" )
-171.491674619836000  3.75234521575985 1 0 0 -0.000000000000028217 0 1
0 -23.468172284192400 0 0 1 14.0800946182358 2 0 0 -42.240284 0 2 0
784.323802803643000 0 0 2 -825.939526461064000 0 0 3
338.295844875043000 0 0 4  -62.326428754429800 0 0 5 4.325223592473780
0 0 6
BCNODE( TEMPERATURE, POLYNOMIAL = 10, ENTITY = "profile2" )
-171.491674619836000  3.75234521575985 1 0 0 -0.000000000000028217 0 1
0 -23.468172284192400 0 0 1 14.0800946182358 2 0 0 -42.240284 0 2 0
784.323802803643000 0 0 2 -825.939526461064000 0 0 3
338.295844875043000 0 0 4  -62.326428754429800 0 0 5 4.325223592473780
0 0 6
BCNODE( TEMPERATURE, POLYNOMIAL = 10, ENTITY = "profile3" )
-171.491674619836000  3.75234521575985 1 0 0 -0.000000000000028217 0 1
0 -23.468172284192400 0 0 1 14.0800946182358 2 0 0 -42.240284 0 2 0
784.323802803643000 0 0 2 -825.939526461064000 0 0 3
338.295844875043000 0 0 4  -62.326428754429800 0 0 5 4.325223592473780
0 0 6
/
END
/
CREATE( FIPREP,DELETE )
PARAMETER( LIST )
CREATE( FISOLV )
/RUN( FISOLV, FOREGROUND )
```

D.3 SUBROUTINE Input File

Alternatively, the SUBROUTINE was revised to accommodate for all the following cases:

Simulations	Case #	Static-g (g*)	Amplitude (A*)	Frequency (F)
4.1: Realistic Sinusoidal Gravity Analysis (Base Case)	1	1.00E-02	2.00E-03	2.80E-02
4.2: Static Residual Gravity Effect	2	0.00E+00	2.00E-06	2.80E-02
4.3: Amplitude Effect Analysis	3	1.00E-02	2.00E-04	2.80E-02
	4	1.00E-02	2.00E-05	2.80E-02
	5	1.00E-02	2.00E-06	2.80E-02
4.4: Frequency Effect Analysis	6	1.00E-02	2.00E-03	5.60E-02
	7	1.00E-02	2.00E-03	1.00E-01
	8	1.00E-02	2.00E-03	1.00E+00
4.5: Real G-jitter Analysis	9	FOTTON 1 - TRAMP (Collected data)		
	10	FOTTON 2 - QSAMP (Collected Data)		

Table D- 1: Subroutine Input Variables for all Cases

Where the subroutine used for the analysis carried out through sections 4.1 to 4.4 is specified as:

```
      SUBROUTINE USRBDY (NELT,NE,NG,BDYF,VARI,DVARI,NDFCD,LDOFU,SHP,
     1                   DSDX,XYZL,PROP,TIME,NPTS,ndp,MNDP,IERR,IOPT)
C
C     USER DEFINED BODY FORCES
C
C     NELT  = GLOBAL ELEMENT NUMBER
C     NE    = LOCAL ELEMENT NUMBER
C     NG    = GROUP NUMBER
C     BDYF  = BODY FORCES
C     VARI  = ARRAY OF SOLUTION VARIBLES AT INTEGRATION POINTS
C     DVARI = GRADIENTS OF SOLUTION VARIABLES AT INTEGRATION POINTS
C     NDFCD = 2(3) COORDINATES DIMENSION, ACCORDING TO THE DEFINITION
IN
C     LDOFU = pointer array for accessing vari and dvari information
C     XYZL  = X,Y,Z COORDINATES
C     SHP   = ELEMENT SHAPE FUNCTIONS
C     DSDX  = SHAPE FUNCTION DERIVATIVES IN THE X,Y,Z DIRECTION
C     PROP  = USER DEFINED PARAMETERS
C     MNDP  = FIRST DIMENSION OF SHAPE FUNCTION MATRICES
C     TIME  = TIME
C     NPTS  = NUMBER OF POINTS
C     IOPT  = 0 - BODY FORCE
C     IOPT  = 1 - LORENTZ FORCE
C
```

```
#include "IMPLCT.COM"
#include "PARUSR.COM"
      DIMENSION BDYF(3,NPTS)
      DIMENSION SHP(NPTS,MNDP),DSDX(NPTS,NDFCD,MNDP),XYZL(NPTS,NDFCD)
      DIMENSION PROP(*),VARI(NPTS,*),DVARI(NPTS,NDFCD,*),LDOFU(*)
      ZRO = 0.D0
C
        TREF=0.0
        CREF = 0.0
        BETAT=1.0
        BETAC = 42.0
        GS=g*
        GV=A*
        F=F* *1.5/0.42
        PI=4.0*ATAN(1.0)
        G=GS+GV*DSIN(2*PI*F*TIME)
C
      DO I=1,NPTS
      TEMP=VARI(I,LDOFU(KDT))
        SPEC = VARI(I,LDOFU(KDS+1))
C
      BDYF(1,I)=0.0
      BDYF(2,I)=0.0
      BDYF(3,I)=G*(BETAT*(TEMP-TREF)-BETAC*(SPEC-CREF))
      ENDDO
      RETURN
      END
```

While the subroutine used for the analysis carried out through section 4.5. i.e. TRAMP and QSAMP cases are specified as follows:

TRAMP Case:

```
      SUBROUTINE USRBDY (NELT,NE,NG,BDYF,VARI,DVARI,NDFCD,LDOFU,SHP,
     1                   DSDX,XYZL,PROP,TIME,NPTS,ndp,MNDP,IERR,IOPT)
C
C     USER DEFINED BODY FORCES
C
C     NELT  = GLOBAL ELEMENT NUMBER
C     NE    = LOCAL ELEMENT NUMBER
C     NG    = GROUP NUMBER
C     BDYF  = BODY FORCES
C     VARI  = ARRAY OF SOLUTION VARIBLES AT INTEGRATION POINTS
C     DVARI = GRADIENTS OF SOLUTION VARIABLES AT INTEGRATION POINTS
C     NDFCD = 2(3) COORDINATES DIMENSION, ACCORDING TO THE DEFINITION
IN
C     LDOFU = pointer array for accessing vari and dvari information
C     XYZL  = X,Y,Z COORDINATES
C     SHP   = ELEMENT SHAPE FUNCTIONS
C     DSDX  = SHAPE FUNCTION DERIVATIVES IN THE X,Y,Z DIRECTION
C     PROP  = USER DEFINED PARAMETERS
C     MNDP  = FIRST DIMENSION OF SHAPE FUNCTION MATRICES
C     TIME  = TIME
C     NPTS  = NUMBER OF POINTS
C     IOPT  = 0 - BODY FORCE
C     IOPT  = 1 - LORENTZ FORCE
```

```
C
#include "IMPLCT.COM"
#include "PARUSR.COM"
      DIMENSION BDYF(3,NPTS)
      DIMENSION SHP(NPTS,MNDP),DSDX(NPTS,NDFCD,MNDP),XYZL(NPTS,NDFCD)
      DIMENSION PROP(*),VARI(NPTS,*),DVARI(NPTS,NDFCD,*),LDOFU(*)
      ZRO = 0.D0
C
        TREF=0.0
        CREF = 0.0
      BETAT=1.0
        BETAC = 42.0
        PI=4.0*ATAN(1.0)
        F11=1.645209D-3*1.5/0.42
        g11=-39.593D-6*DCOS(2*PI*F11*TIME)
      G1=(g11)/9.800
        F21=1.157556D-3*1.5/0.42
        F22=1.872925D-3*1.5/0.42
        F23=2.237846D-3*1.5/0.42
        F24=2.515350D-3*1.5/0.42
        F25=3.281500D-3*1.5/0.42
        g21=-1.596D-6*DCOS(2*PI*F21*TIME)
        g22=-4.409D-6*DCOS(2*PI*F22*TIME)
        g23=-5.404D-6*DCOS(2*PI*F23*TIME)
        g24=-8.237D-6*DCOS(2*PI*F24*TIME)
        g25=-1.721D-6*DCOS(2*PI*F25*TIME)
        G2=(g21+g22+g23+g24+g25)/9.800
        F31=1.643534D-3*1.5/0.42
        F32=1.870828D-3*1.5/0.42
        F33=2.073682-3*1.5/0.42
        F34=3.290399D-3*1.5/0.42
        F35=4.149568D-3*1.5/0.42
        g31=-6.243D-6*DCOS(2*PI*F31*TIME)
        g32=-0.838D-6*DCOS(2*PI*F32*TIME)
        g33=-1.582D-6*DCOS(2*PI*F33*TIME)
        g34=-3.014D-6*DCOS(2*PI*F34*TIME)
        g35=-0.958D-6*DCOS(2*PI*F35*TIME)
      G3=(g31+g32+g33+g34+g35)/9.800
C
      DO I=1,NPTS
      TEMP=VARI(I,LDOFU(KDT))
        SPEC = VARI(I,LDOFU(KDS+1))
C
      BDYF(1,I)=G1*(BETAT*(TEMP-TREF)-BETAC*(SPEC-CREF))
      BDYF(2,I)=G2*(BETAT*(TEMP-TREF)-BETAC*(SPEC-CREF))
      BDYF(3,I)=G3*(BETAT*(TEMP-TREF)-BETAC*(SPEC-CREF))
      ENDDO
      RETURN
      END
C
```

QSAMP Case:

```
      SUBROUTINE USRBDY (NELT,NE,NG,BDYF,VARI,DVARI,NDFCD,LDOFU,SHP,
     1                   DSDX,XYZL,PROP,TIME,NPTS,ndp,MNDP,IERR,IOPT)
C
C     USER DEFINED BODY FORCES
```

```
C
C     NELT  = GLOBAL ELEMENT NUMBER
C     NE    = LOCAL ELEMENT NUMBER
C     NG    = GROUP NUMBER
C     BDYF  = BODY FORCES
C     VARI  = ARRAY OF SOLUTION VARIBLES AT INTEGRATION POINTS
C     DVARI = GRADIENTS OF SOLUTION VARIABLES AT INTEGRATION POINTS
C     NDFCD = 2(3) COORDINATES DIMENSION, ACCORDING TO THE DEFINITION
IN
C     LDOFU = pointer array for accessing vari and dvari information
C     XYZL  = X,Y,Z COORDINATES
C     SHP   = ELEMENT SHAPE FUNCTIONS
C     DSDX  = SHAPE FUNCTION DERIVATIVES IN THE X,Y,Z DIRECTION
C     PROP  = USER DEFINED PARAMETERS
C     MNDP  = FIRST DIMENSION OF SHAPE FUNCTION MATRICES
C     TIME  = TIME
C     NPTS  = NUMBER OF POINTS
C     IOPT  = 0 - BODY FORCE
C     IOPT  = 1 - LORENTZ FORCE
C
#include "IMPLCT.COM"
#include "PARUSR.COM"
      DIMENSION BDYF(3,NPTS)
      DIMENSION SHP(NPTS,MNDP),DSDX(NPTS,NDFCD,MNDP),XYZL(NPTS,NDFCD)
      DIMENSION PROP(*),VARI(NPTS,*),DVARI(NPTS,NDFCD,*),LDOFU(*)
      ZRO = 0.D0
C
        TREF=0.0
        CREF = 0.0
      BETAT=1.0
        BETAC = 42.0
        PI=4.0*ATAN(1.0)
        F11=2.234D-3*1.5/0.42
        F12=2.436D-3*1.5/0.42
        F13=2.656D-3*1.5/0.42
        F14=3.397D-3*1.5/0.42
        g11=-23.009D-6*DCOS(2*PI*F11*TIME)
        g12=-0.746D-6*DCOS(2*PI*F12*TIME)
        g13=-1.707D-6*DCOS(2*PI*F13*TIME)
        g14=-1.265D-6*DCOS(2*PI*F14*TIME)
      G1=(g11+g12+g13+g14)/9.800
        F21=2.232D-3*1.5/0.42
        F22=2.450D-3*1.5/0.42
        F23=2.638D-3*1.5/0.42
        F24=2.816D-3*1.5/0.42
        F25=2.998D-3*1.5/0.42
        F26=3.182D-3*1.5/0.42
        g21=-1.381D-6*DCOS(2*PI*F21*TIME)
        g22=-0.153D-6*DCOS(2*PI*F22*TIME)
        g23=-0.478D-6*DCOS(2*PI*F23*TIME)
        g24=-0.661D-6*DCOS(2*PI*F24*TIME)
        g25=-0.440D-6*DCOS(2*PI*F25*TIME)
        g26=-0.131D-6*DCOS(2*PI*F26*TIME)
        G2=(g21+g22+g23+g24+g25+g26)/9.800
        F31=2.234D-3*1.5/0.42
        F32=2.664D-3*1.5/0.42
        g31=-1.249D-6*DCOS(2*PI*F31*TIME)
```

```
        g32=-0.091D-6*DCOS(2*PI*F32*TIME)
        G3=(g31+g32)/9.800
C
      DO I=1,NPTS
      TEMP=VARI(I,LDOFU(KDT))
        SPEC = VARI(I,LDOFU(KDS+1))
C
      BDYF(1,I)=G1*(BETAT*(TEMP-TREF)-BETAC*(SPEC-CREF))
      BDYF(2,I)=G2*(BETAT*(TEMP-TREF)-BETAC*(SPEC-CREF))
      BDYF(3,I)=G3*(BETAT*(TEMP-TREF)-BETAC*(SPEC-CREF))
      ENDDO
      RETURN
      END
C
```